

The Butler Matrix as a Multiple Beam Beamforming Network

by

Pieter Böning



*Thesis presented in partial fulfilment of the requirements
for the degree of Master of Engineering (Electronic) in the
Faculty of Engineering at Stellenbosch University*

Supervisor: Dr. C. Van Niekerk

March 2020

The financial assistance of the National Research Foundation (NRF) and Cobham Aerospace Communications towards this research is hereby acknowledged. Opinions expressed and conclusions arrived at, are solely those of the author.

Declaration

By submitting this thesis electronically, I declare that the entirety of the work contained therein is my own, original work, that I am the sole author thereof (save to the extent explicitly otherwise stated), that reproduction and publication thereof by Stellenbosch University will not infringe any third party rights and that I have not previously in its entirety or in part submitted it for obtaining any qualification.

Date: .March 2020

Copyright © 2020 Stellenbosch University
All rights reserved.

Abstract

The Butler Matrix as a Multiple Beam Beamforming Network

P. Böning

*Department of Electric and Electronic Engineering,
University of Stellenbosch,
Private Bag X1, Matieland 7602, South Africa.*

Thesis: MEng (Elec)

March 2020

High bandwidth communication has become an essential part of modern society. The increasing demand for data requires engineers to implement innovative solutions to utilise the finite electromagnetic spectrum. Methods such as time, frequency, and spatial division have been adopted to increase the effective use of the spectrum. Time and frequency-division reduces the amount of bandwidth, the property that needs to be maximised, available to a single user.

To implement spatial division efficiently and cost-effectively is a complex problem which has received a lot of attention lately as communication devices are now more than ever, accessible to the average person.

To address the spatial division problem, multiple beam beamforming networks (MBBFN) is the suggested solution, but are expensive and technically difficult to implement. There is a direct correlation between the proposed Butler Matrix and the Fast Fourier Transform, in that both are an optimal solution to the underlying calculation, requiring the least amount of operations. In the case of the Butler Matrix, these operations refer to power dividers and combiners, and phase shifters. This poses a viable solution in terms of efficiency and cost-effectiveness.

There are many implementations of the Butler Matrix, two of which are analysed, constructed, and measured. One implementation was done at a higher frequency to effectively increase the operational bandwidth. The higher frequency posed significant challenges resulting in unacceptable performance degradation, but still proved a working concept. The lower frequency implementation was easier to design and implement with very low cost, and successfully demonstrated the ability of the Butler Matrix as a MBBFN.

ABSTRACT

iii

The theoretical analysis of the Butler Matrix concept provides a better understanding of MBBFN's, which is supported by simulated and measured results.

Uittreksel

Die Butler Matriks as Meervoudige Straalvormingsnetwerk

(“The Butler Matrix as a Multiple Beam Beamforming Network”)

P. Böning

*Departement Elektriese en Elektroniese Ingenieurswese,
Universiteit van Stellenbosch,
Privaatsak X1, Matieland 7602, Suid Afrika.*

Tesis: MIng (Elek)

Maart 2020

Kommunikasie met 'n hoë bandwydte is 'n wesenlike deel van die moderne samelewing. Die toenemende vraag na data, vereis dat ingenieurs innoverende oplossings moet implementeer om die eindige elektromagnetiese spektrum te gebruik. Metodes soos tyd, frekwensie en ruimtelike verdeling word toegepas om die effektiewe gebruik van die spektrum te verhoog. Tyd en frekwensieverdeling verminder die hoeveelheid bandwydte, die eienskap wat gemaksimeer moet word, wat beskikbaar is vir 'n enkele gebruiker. Om ruimtelike verdeling doeltreffend en koste-effektief te implementeer, is 'n ingewikkelde probleem wat die afgelope tyd baie aandag geniet, aangesien kommunikasietoestelle nou meer as ooit tevore vir die gemiddelde persoon toeganklik is.

Om die ruimtelike verdeling probleem aan te spreek, is meervoudige stralingsvormende netwerke (MSVN) die verkose oplossing, maar is duur en tegnies moeilik om te implementeer. Daar is 'n direkte verband tussen die voorge-stelde Butler Matriks en die Vinnige Fourier-transformasie, deurdat beide 'n optimale oplossing vir die onderliggende berekening is, wat die minste hoeveelheid bewerkings benodig. In die geval van die Butler Matriks, verwys hierdie bewerkings na kragverdelers, kragkombineerders en faseverskuiwings. Dit bied 'n haalbare oplossing ten opsigte van doeltreffendheid en koste-effektiwiteit.

Daar is baie implementerings van die Butler Matriks, waarvan twee ontleed, gekonstrueer en gemeet word. Een implementering is met 'n hoër frekwensie gedoen om die operasionele bandwydte effektief te verhoog. Die hoër frekwensie het uitdagings opgelewer wat tot onaanvaarbare agteruitgang van verrigting gelei het, maar kon steeds 'n werkende konsep illustreer. Die implementering

van die laer frekwensie was makliker om te ontwerp en met baie lae koste te implementeer en het die vermoë van die Butler Matriks as 'n MSVN suksesvol getoon.

Die teoretiese analise van die Butler Matriks-konsep bied 'n beter begrip van MSVN's, wat ondersteun word deur gesimuleerde en gemete resultate.

Contents

Declaration	i
Abstract	ii
Uittreksel	iv
Contents	vi
List of Figures	viii
List of Tables	xi
Nomenclature	xiii
1 Introduction	1
1.1 Overview	1
1.2 Problem Statement	1
1.3 Objectives	2
1.4 Thesis Outline	2
2 Literature Study	3
2.1 Antennas	3
2.2 Beamforming	19
3 The Butler Matrix	28
3.1 Concept	28
3.2 Derivation	28
3.3 Fourier Transform Equivalence	33
4 Implementation of the Butler Matrix	39
4.1 Ideal Implementation	39
4.2 Practical considerations	39
4.3 Microstrip Implementation at 1.5 GHz	40
4.4 Microstrip Implementation at 15 GHz	47

<i>CONTENTS</i>	vii
5 Results	52
5.1 Ideal Implementation	52
5.2 Microstrip Implementation at 1.5 GHz	54
5.3 Microstrip Implementation at 15 GHz	59
6 Conclusion	65
Appendices	67
A $M \times N$ Planar Array Factor Derivation	68
B Results - Graphs	71
B.1 Butler Matrix results - Ideal	71
B.2 Butler Matrix results - Microstrip, CST and AWR simulation	75
B.3 Butler Matrix results - Measured PCB	81
B.4 Butler Matrix results - Ideal, 15 GHz	86
B.5 Butler Matrix results - CST Simulation, 15 GHz	90
B.6 Butler Matrix results - Measured PCB, 15 GHz	94
List of References	99

List of Figures

2.1	Hertzian dipole	5
2.2	Hertzian dipole radiation pattern(Cartesian in dB, Normalised)	10
2.3	Finite length dipoles directivity(Cartesian in dB)	14
2.4	Finite length dipoles directivity(Cartesian in dB, normalised)	14
2.5	Geometrical description of the helical antenna	15
2.6	Geometrical description of a probe-fed, rectangular microstrip patch antenna	16
2.7	Geometrical description of a line-fed, rectangular microstrip patch antenna	17
2.8	Linear array (far-field approximation)	17
2.9	$ AF $ for varying d , $n = 4$	19
2.10	$ AF $ for varying n , $d = 0.5\lambda$	20
2.11	4-element BFN	20
2.12	$ AF $ for varying θ_0 , $n = 4$, $d = \frac{\lambda}{2}$	21
2.13	Limits of scan angle θ_0 for varying i	23
2.14	Change in scan angle θ_0 over frequency, $i = 0.5$, $B_{\%} = 0.2$	24
2.15	Example of a 4-element Multiple beam beamformer	25
2.16	Digital beamformer - receive array	26
3.1	Example of a 4-element Butler Matrix	29
3.2	Valid region for orthogonality condition	33
3.3	Excitation amplitudes as $f(x)$	35
3.4	Magnitude and phase of $\mathcal{F}[f(x)]$	36
3.5	$ AF $ - Single beams	36
3.6	$ AF $ - Single port excitations	37
3.7	$ AF $ - Different beam pairs	38
3.8	$ AF $ - Increasing excitation on 1 beam	38
4.1	AWR circuit of ideal circuit	40
4.2	Butler Matrix - Indicating non-zero and crossing lines	41
4.3	42
4.4	3D Model of Butler Matrix in CST	42
4.5	Microstrip implementation - measurement setup	44
4.6	Microstrip antenna array dimensions	46

4.7	46
4.8 Interconnection between microstrip patch and Butler Matrix . . .	47
4.9 Microstrip patch array, mounted in anechoic chamber	48
4.10 Crossover, utilising 2 quadrature hybrids	48
4.11 Ideal AWR model, with hybrid crossover	49
4.12 CST model, with hybrid crossover, feed lines	50
4.13 Manufactured PCB, with TRL calibration	51
5.1 Butler Matrix, patch antenna integration - Directivity, normalised	60
A.1 2D Planar Array	69
B.1 AWR Ideal simulation - Reflection	71
B.2 AWR Ideal simulation - Isolation	72
B.3 AWR Ideal simulation - Transmission magnitude, beam port 1 . .	72
B.4 AWR Ideal simulation - Transmission phase, beam port 1	73
B.5 AWR Ideal simulation - Transmission phase, beam port 2	73
B.6 AWR Ideal simulation - Transmission phase, beam port 3	74
B.7 AWR Ideal simulation - Transmission phase, beam port 4	74
B.8 Microstrip CST and AWR simulation - Reflection	75
B.9 Microstrip CST and AWR simulation - Beam port isolation . . .	76
B.10 Microstrip CST and AWR simulation - Element port isolation . .	76
B.11 Microstrip CST and AWR simulation - Transmission magnitude, beam port 1	77
B.12 Microstrip CST and AWR simulation - Transmission phase, beam port 1	78
B.13 Microstrip CST and AWR simulation - Transmission phase, beam port 2	78
B.14 Microstrip CST and AWR simulation - Transmission phase, beam port 3	79
B.15 Microstrip CST and AWR simulation - Transmission phase, beam port 4	80
B.16 Measured microstrip PCB - Reflection	81
B.17 Measured microstrip PCB - Beam port isolation	82
B.18 Measured microstrip PCB - Element port isolation	82
B.19 Measured microstrip PCB - Transmission magnitude, beam port 1	83
B.20 Measured microstrip PCB - Transmission phase, beam port 1 . .	84
B.21 Measured microstrip PCB - Transmission phase, beam port 2 . .	84
B.22 Measured microstrip PCB - Transmission phase, beam port 3 . .	85
B.23 Measured microstrip PCB - Transmission phase, beam port 4 . .	85
B.24 AWR Ideal simulation - Reflection, 15 GHz	86
B.25 AWR Ideal simulation - Isolation, 15GHz	87
B.26 AWR Ideal simulation - Transmission magnitude, beam port 1, 15 GHz	87

*LIST OF FIGURES***x**

B.27 AWR Ideal simulation - Transmission phase, beam port 1, 15 GHz	88
B.28 AWR Ideal simulation - Transmission phase, beam port 2, 15 GHz	89
B.29 AWR Ideal simulation - Transmission phase, beam port 3, 15 GHz	89
B.30 AWR Ideal simulation - Transmission phase, beam port 4, 15 GHz	90
B.31 CST simulation - Reflection, 15 GHz	91
B.32 CST simulation - Isolation, 15 GHz	91
B.33 CST simulation - Transmission magnitude, beam port 1, 15 GHz	92
B.34 CST simulation - Transmission phase, beam port 1, 15 GHz . . .	92
B.35 CST simulation - Transmission phase, beam port 2, 15 GHz . . .	93
B.36 CST simulation - Transmission phase, beam port 3, 15 GHz . . .	93
B.37 CST simulation - Transmission phase, beam port 4, 15 GHz . . .	94
B.38 Measured PCB - Reflection, 15 GHz	95
B.39 Measured PCB - Isolation, 15 GHz	95
B.40 Measured PCB - Transmission magnitude, beam port 1, 15 GHz	96
B.41 Measured PCB - Transmission phase, beam port 1, 15 GHz . . .	96
B.42 Measured PCB - Transmission phase, beam port 2, 15 GHz . . .	97
B.43 Measured PCB - Transmission phase, beam port 3, 15 GHz . . .	97
B.44 Measured PCB - Transmission phase, beam port 4, 15 GHz . . .	98

List of Tables

2.1	Finite length dipoles	13
3.1	Dot products for an N beam BFN	33
4.1	Microstrip Implementation at 1.5 GHz - Design parameters	41
4.2	Microstrip Implementation - Measurement setup	43
4.3	Microstrip antenna array dimensions	45
4.4	Microstrip Implementation at 15 GHz - Design parameters	49
5.1	AWR Ideal simulation - Reflection and Isolation	52
5.2	AWR Ideal simulation - Transmission phase, beam port 1	53
5.3	AWR Ideal simulation - Transmission phase, beam port 2	53
5.4	AWR Ideal simulation - Transmission phase, beam port 3	53
5.5	AWR Ideal simulation - Transmission phase, beam port 4	54
5.6	AWR Ideal simulation - Progressive phase shift	54
5.7	Microstrip CST and AWR simulation - Reflection	55
5.8	Microstrip CST and AWR simulation - Isolation	55
5.9	Microstrip AWR simulation - Beam port 1 bandwidth	56
5.10	Microstrip AWR simulation - Beam port 2 bandwidth	56
5.11	Microstrip AWR simulation - Beam port 3 bandwidth	56
5.12	Microstrip AWR simulation - Beam port 4 bandwidth	56
5.13	Microstrip AWR simulation - Progressive phase shift	57
5.14	Microstrip CST simulation - Progressive phase shift	57
5.15	Measured microstrip PCB - Reflection and Isolation	57
5.16	Measured microstrip PCB - Beam port 1 bandwidth	58
5.17	Measured microstrip PCB - Beam port 2 bandwidth	58
5.18	Measured microstrip PCB - Beam port 3 bandwidth	58
5.19	Measured microstrip PCB - Beam port 4 bandwidth	58
5.20	Measured microstrip PCB - Progressive phase shift	59
5.21	CST Simulation - Beam port 1 bandwidth, 15 GHz	60
5.22	CST Simulation - Beam port 2 bandwidth, 15 GHz	61
5.23	CST Simulation - Beam port 3 bandwidth, 15 GHz	61
5.24	CST Simulation - Beam port 4 bandwidth, 15 GHz	61
5.25	CST Simulation - Progressive phase shift, 15 GHz	62

*LIST OF TABLES***xii**

5.26	Measured PCB - Beam port 1 bandwidth, 15 GHz	62
5.27	Measured PCB - Beam port 2 bandwidth, 15 GHz	62
5.28	Measured PCB - Beam port 3 bandwidth, 15 GHz	63
5.29	Measured PCB - Beam port 4 bandwidth, 15 GHz	63
5.30	Measured PCB - Progressive phase shift, 15 GHz	64
5.31	Measured PCB - Progressive phase shift, 14.25 GHz	64

Nomenclature

Constants

c_0	Speed of light in a vacuum	[m/s]
ϵ_0	Vacuum permittivity	[F/m]
μ_0	Vacuum permeability	[H/m]
π	Ratio of circumference to diameter	[m/m]

Variables

θ	Polar angle	[degrees]
x	Coordinate	[m]
\ddot{x}	Acceleration	[m/s ²]

Vectors

\mathbf{E}	Electric field vector
$\hat{\mathbf{r}}$	Radial unit vector

Subscripts

A_r	Radial component of vector \mathbf{A}
-------	---

Other

AF	Array factor
----	--------------

Chapter 1

Introduction

1.1 Overview

Beamforming networks have established their importance in modern radio systems. There are ever increasing requirements for higher bandwidth communication, especially with the rise of Internet of Things (IoT) and Fifth Generation (5G) networks over the last few years.

1.2 Problem Statement

The number of users requiring high bandwidth communication systems are ever increasing, which poses a significant problem. There is a finite amount of frequency spectrum available, which can only be divided into a finite amount of usable channels when multiple users want to occupy a specific band of frequencies at the same time. Dividing the limited frequency spectrum into channels lowers the available bandwidth per user.

A method employed to divide access even more, is time division. The concept of time division is that a certain frequency channel is divided into timeslots, where the number of timeslots depend on the number of users trying to use the same frequency channel. This also lowers the data throughput each user can have.

The third method employed is space division. When multiple users are located in separate locations, in an angular space, a phased array can be used to point the main beam of the antenna towards the current active user. This will maximise the possible gain of the antenna, and separate the signal of interest from the interferers (other users). Many phased arrays can be incorporated in a single system to allow multiple users to simultaneously use the same frequency channel, given they're spatially separated. Using multiple phased array systems in this way is inefficient, instead, a multiple beam beamforming network (MBBFN) is proposed.

1.3 Objectives

The main aim of this thesis is to analyse the Butler Matrix concept as a MBBFN. The secondary aim of this thesis is to quantify the scalability of the Butler Matrix. The third aim is to implement the Butler Matrix in a practical way and demonstrate its ability as a MBBFN. In order to reach these aims, the following objectives will need to be achieved:

1. Introduce antennas and antenna arrays, as well as some methods for beamforming.
2. Analyse the Butler Matrix theoretically and establish its mathematical operation.
3. Compare different implementations of the Butler Matrix to discover its viability as a beamforming network.
4. Draw a conclusion that is supported by simulated and measured results.

1.4 Thesis Outline

The following chapter introduces some basic properties of antennas, and explains how the simplest antenna radiates electromagnetic energy into space. Some examples of widely adopted antenna elements are discussed. Antenna arrays are then introduced, followed by the concept of beamforming and leads into multiple beam beamforming. Digital beamforming is also briefly discussed.

Chapter 3 introduces the Butler Matrix, which is a MBBFN. An in depth derivation is done, and some limitations are highlighted. The Butler Matrix and its Fourier Transform relationship is analysed.

Chapter 4 introduces implementations of the Butler Matrix in microstrip technology. At first an ideal circuit is defined, which is followed up by a microstrip circuit that is simulated, manufactured, and measured. Two different use cases are analysed, one to operate at 1.5 GHz, the other at 15 GHz.

Chapter 5 analyses the results obtained from the implementations in Chapter 4.

This body of work concludes with Chapter 6, evaluating the results from Chapter 5 and how the objectives were achieved.

Chapter 2

Literature Study

2.1 Antennas

Antennas are an integral part of any radio system, it performs the transformation of electromagnetic waves in free space to voltages and currents on a transmission line, and vice versa (Huang and Boyle, 2008). This transformation needs to be as efficient as possible, as the power density of a propagating electromagnetic wave typically gets very small over large distances. A lot of effort goes into designing antennas and the circuits that feed them, also known as feed networks.

Electromagnetic waves propagate radially from its source. When observing the waves at a large distance r , the radiating source is considered as a point, and the fields are real. The Poynting vector is defined by the cross product of the electric and magnetic fields, and is used to quantify the flow of power density.

$$\mathbf{S} = \mathbf{E} \times \mathbf{H}^* \quad \left(\frac{W}{m^2} \right) \quad (2.1.1)$$

Consider an ideal radiating point source, radiating uniformly in all directions. The power flowing through a spherical surface, with the point source as origin, will be uniform over the sphere. The surface area of the sphere increases at a rate r^2 , as the radius r of the sphere increases. The power density decreases at a rate $\frac{1}{r^2}$ because the same total power (Poynting vector) is now integrated over a larger area. This $\frac{1}{r^2}$ relation is commonly known as the inverse-square law, and it is present in many natural laws like gravity, electrostatics and sound (Blake and Long, 2009).

According to Blake and Long (2009), an ideal antenna will radiate all incoming power (from a transmission line) in the desired directions and with the desired polarisation. In reality an antenna radiates some energy in all directions, similar to the point source discussed earlier, meaning that some energy propagates in an undesired direction and is lost. An antenna parameter

used to quantify the proportion of energy that is radiated in a specific direction, is called the beam or radiation pattern. *Radiation pattern* is a more general term, which could refer to field or power pattern. This body of work is only concerned with the power pattern, which is represented in decibel scale as a function of angular space (Balanis, 2012). When referring to the radiation patterns of antennas, they are classified within 3 major classes:

- Isotropic - Radiates equally in all directions
- Omnidirectional - Radiates equally in a plane
- Directional - Radiates in one direction

Isotropic radiation patterns are purely theoretical, but are widely used to analyse antenna arrays. The advantage of using an isotropic pattern when analysing arrays is that it leaves out the radiation characteristics of the antenna element (Sidelobes, HPBW, etc.), and considers only the characteristics of the array. Omnidirectional and Directional antennas will be discussed in section 2.1.2 and section 2.1.3.

It should be noted that here it is referred to as a radiation pattern, but antennas are reciprocal devices, they capture energy in the same way that they radiate energy. In the next couple of subsections, some well-understood antenna elements will be discussed, which will lead to a discussion about antenna arrays and beamforming.

2.1.1 Hertzian Dipole

The simplest radiating element is the Hertzian Dipole. It is also known as an infinitesimal, or elemental electric dipole. The Hertzian dipole is a dipole that is considerably shorter than a tenth of the wavelength. The current distribution on the wire is uniform but still varies with time, oscillating at some frequency. Blake and Long (2009) also mentions a short dipole, which is one of about a tenth of the wavelength and does not necessarily have uniform current distribution.

The Hertzian dipole is a radiating element which can be analysed relatively easily. Cheng (2014) proposes three steps to analyse the electromagnetic fields from a current distribution. The first step is to determine \mathbf{A} , the *vector magnetic potential* from \mathbf{J} , the *volume current density*, using equation 2.1.2. The second step is to find \mathbf{H} , the *magnetic field intensity*, from \mathbf{A} using equation 2.1.3. The final step is to calculate \mathbf{E} , the *electric field intensity*, from \mathbf{H} using equation 2.1.4. The equations used here follow lengthy derivations by Cheng (2014) which will not be discussed in this thesis.

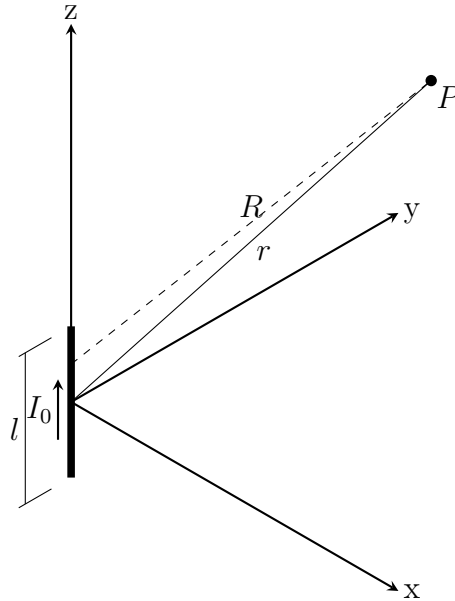


Figure 2.1: Hertzian dipole

$$\mathbf{A} = \frac{\mu}{4\pi} \int_{\mathbf{V}'} \frac{\mathbf{J} e^{-jkR}}{R} dv' \quad (2.1.2)$$

$$\mathbf{H} = \frac{1}{\mu} \nabla \times \mathbf{A} \quad (2.1.3)$$

$$\mathbf{E} = \frac{1}{-j\omega\epsilon} \nabla \times \mathbf{H} \quad (2.1.4)$$

Where:

$\mathbf{V}' =$ Source volume

$R =$ Distance from any point in \mathbf{V}' to the observation point

Equation equation 2.1.2 can be simplified by applying the infinitesimal dimensions of the source:

$$\mathbf{J} = \begin{cases} I_0 \delta(x') \delta(y') \hat{\mathbf{z}} & -\frac{l}{2} \leq z' \leq \frac{l}{2} \\ 0 & \text{elsewhere} \end{cases}$$

This integral is evaluated over z' , meaning R is dependent on dz' , making the integral more difficult to solve. Since l is very small, R can be approximated as r , which greatly simplifies the integral:

$$\begin{aligned}
\mathbf{A} &= \hat{\mathbf{z}} \frac{\mu I_0}{4\pi} \left(\frac{e^{-jkr}}{r} \right) \int_{-\frac{l}{2}}^{\frac{l}{2}} dz' \\
&= \hat{\mathbf{z}} \frac{\mu I_0 l}{4\pi} \left(\frac{e^{-jkr}}{r} \right)
\end{aligned} \tag{2.1.5}$$

From equation 2.1.5, step 2 can be followed to calculate \mathbf{H} . It is much easier to evaluate \mathbf{H} and \mathbf{E} in a spherical coordinate system (Balanis, 2012). The transformation matrix in equation 2.1.6 is used to transform $\mathbf{A} = A_x \hat{\mathbf{x}} + A_y \hat{\mathbf{y}} + A_z \hat{\mathbf{z}}$ to $\mathbf{A} = A_r \hat{\mathbf{r}} + A_\theta \hat{\boldsymbol{\theta}} + A_\phi \hat{\boldsymbol{\phi}}$.

$$\begin{bmatrix} A_r \\ A_\theta \\ A_\phi \end{bmatrix} = \begin{bmatrix} \sin \theta \cos \phi & \sin \theta \sin \phi & \cos \theta \\ \cos \theta \cos \phi & \cos \theta \sin \phi & -\sin \theta \\ -\sin \phi & \cos \phi & 0 \end{bmatrix} \begin{bmatrix} A_x \\ A_y \\ A_z \end{bmatrix} \tag{2.1.6}$$

In this case, A_x and A_y is 0, leading to an easier solution for \mathbf{A} , in spherical coordinates:

$$\begin{aligned}
A_r &= \cos \theta \frac{\mu I_0 l}{4\pi} \left(\frac{e^{-jkr}}{r} \right) \\
A_\theta &= -\sin \theta \frac{\mu I_0 l}{4\pi} \left(\frac{e^{-jkr}}{r} \right) \\
A_\phi &= 0
\end{aligned} \tag{2.1.7}$$

To evaluate the curl in spherical coordinates, equation 2.1.8 is used.

$$\boldsymbol{\nabla} \times \mathbf{A} = \frac{1}{r^2 \sin \theta} \begin{vmatrix} \hat{\mathbf{r}} & r\hat{\boldsymbol{\theta}} & r \sin \theta \hat{\boldsymbol{\phi}} \\ \frac{\partial}{\partial r} & \frac{\partial}{\partial \theta} & \frac{\partial}{\partial \phi} \\ A_r & rA_\theta & r \sin \theta A_\phi \end{vmatrix} \tag{2.1.8}$$

There is no ϕ -variation in both A_r and A_θ , and $A_\phi = 0$. This significantly simplifies the curl operation.

$$H_r = 0$$

$$H_\theta = 0$$

$$\begin{aligned}
H_\phi &= \frac{1}{\mu r} \left[\frac{\partial}{\partial r} \left(-\sin \theta \frac{\mu I_0 l e^{-jkr}}{4\pi} \right) - \frac{\partial}{\partial \theta} \left(\cos \theta \frac{\mu I_0 l e^{-jkr}}{4\pi r} \right) \right] \\
&= \frac{1}{\mu r} \left[\sin \theta \frac{jk\mu I_0 l e^{-jkr}}{4\pi} + \sin \theta \frac{\mu I_0 l e^{-jkr}}{4\pi r} \right] \\
&= \frac{I_0 l}{4\pi r} \sin \theta e^{-jkr} \left[jk + \frac{1}{r} \right] \tag{2.1.9}
\end{aligned}$$

$$= -\frac{I_0 l}{4\pi} k^2 \sin \theta \left[\frac{1}{jkr} + \frac{1}{(jkr)^2} \right] e^{-jkr} \tag{2.1.10}$$

Rewriting equation 2.1.9 as equation 2.1.10 is mostly for aesthetic reasons. This is an “easier to read” formula, separating the constants neatly from the oscillating and decaying parameters. Now that \mathbf{H} is determined, the final step can be approached using equation 2.1.4:

$$\nabla \times \mathbf{H} = \frac{1}{r^2 \sin \theta} \begin{vmatrix} \hat{\mathbf{r}} & r\hat{\boldsymbol{\theta}} & r \sin \theta \hat{\boldsymbol{\phi}} \\ \frac{\partial}{\partial r} & \frac{\partial}{\partial \theta} & \frac{\partial}{\partial \phi} \\ H_r & rH_\theta & r \sin \theta H_\phi \end{vmatrix}$$

H_ϕ is the only component of \mathbf{H} that is not 0.

$$E_\phi = 0$$

$$\begin{aligned}
\mathbf{E} &= \frac{1}{j\omega\epsilon} \frac{1}{r^2 \sin\theta} \left[\frac{\partial}{\partial\theta} (r \sin\theta H_\phi) \hat{\mathbf{r}} - r \frac{\partial}{\partial r} (r \sin\theta H_\phi) \hat{\boldsymbol{\theta}} \right] \\
E_r &= \frac{1}{j\omega\epsilon} \frac{1}{r^2 \sin\theta} \frac{\partial}{\partial\theta} \left(-\frac{r I_0 l}{4\pi} k^2 \sin^2\theta \left[\frac{1}{jkr} + \frac{1}{(jkr)^2} \right] e^{-jkr} \right) \\
&= -\frac{I_0 l}{4\pi \sin\theta} \frac{1}{\omega\epsilon} \frac{1}{jr} k^2 \frac{\partial}{\partial\theta} (\sin^2\theta) \left[\frac{1}{jkr} + \frac{1}{(jkr)^2} \right] e^{-jkr} \\
&= -\frac{I_0 l}{2\pi} k^2 \cos\theta \frac{\eta}{jkr} \left[\frac{1}{jkr} + \frac{1}{(jkr)^2} \right] e^{-jkr} \\
&= -\frac{I_0 l}{2\pi} \eta k^2 \cos\theta \left[\frac{1}{(jkr)^2} + \frac{1}{(jkr)^3} \right] e^{-jkr} \tag{2.1.11}
\end{aligned}$$

$$\begin{aligned}
E_\theta &= -\frac{1}{j\omega\epsilon} \frac{1}{r \sin\theta} \frac{\partial}{\partial r} \left(-\frac{r I_0 l}{4\pi} k^2 \sin^2\theta \left[\frac{1}{jkr} + \frac{1}{(jkr)^2} \right] e^{-jkr} \right) \\
&= \frac{I_0 l}{4\pi} k^2 \sin\theta \frac{1}{\omega\epsilon} \frac{1}{jr} \frac{\partial}{\partial r} \left(\left[\frac{1}{jk} + \frac{1}{(jk)^2 r} \right] e^{-jkr} \right) \\
&= -\frac{I_0 l}{4\pi} k^2 \sin\theta \frac{1}{\omega\epsilon} \frac{1}{jr} \left[1 + \frac{1}{jkr} + \frac{1}{(jkr)^2} \right] e^{-jkr} \\
&= -\frac{I_0 l}{4\pi} \eta k^2 \sin\theta \left[\frac{1}{jkr} + \frac{1}{(jkr)^2} + \frac{1}{(jkr)^3} \right] e^{-jkr} \tag{2.1.12}
\end{aligned}$$

Where:

$$\eta = \frac{\omega\mu}{k}$$

In the same way as H_ϕ was rewritten to be “easier to read”, equation 2.1.11 and equation 2.1.12 is also written in this way. It can be seen that the different terms that are inversely proportional to kr will decay at different rates. H_ϕ has the terms $\frac{1}{jkr}$ and $\frac{1}{(jkr)^2}$, of which $\frac{1}{(jkr)^2}$ decays faster as r increases. It can then be stated that for a significantly large r , $\frac{1}{(jkr)^2}$ becomes much smaller than $\frac{1}{jkr}$. This approximation is known as the *far field* approximation or the *Fraunhofer* region. This is also applied to E_r and E_θ , and since E_r has $\frac{1}{(jkr)^2}$ and $\frac{1}{(jkr)^3}$ terms only, it can be approximated that $E_r \approx 0$. These approximations simplify \mathbf{E} and \mathbf{H} to:

$$\mathbf{E} \simeq \frac{jI_0 l}{4\pi r} \eta k \sin\theta e^{-jkr} \hat{\boldsymbol{\theta}} \tag{2.1.13}$$

$$\mathbf{H} \simeq \frac{jI_0 l}{4\pi r} k \sin\theta e^{-jkr} \hat{\boldsymbol{\phi}} \tag{2.1.14}$$

An interesting observation to make is that:

$$\frac{E_\theta}{H_\phi} = \eta \tag{2.1.15}$$

There are various definitions for what are considered “significantly large r ”. According to Huang and Boyle (2008), there are two definitions for this that depend on the largest dimension of the antenna, D .

$$r > \begin{cases} 3\lambda & D < \lambda \\ \frac{2D^2}{\lambda} & D > \lambda \end{cases}$$

When r is not significantly large, the far field approximation cannot be made, and the field is known as *near field*. The near field is not as important for the purposes of this piece of work.

To view the power pattern, the power density function must be calculated. The time-averaged version (over one period, sinusoidal excitation) of equation 2.1.1 is used, along with equation 2.1.13 and equation 2.1.14.

$$\bar{\mathbf{S}} = \frac{1}{2} \text{Re} [\mathbf{E} \times \mathbf{H}^*] \quad (2.1.16)$$

$$\begin{aligned} &= \frac{1}{2} \text{Re} \left[\left(\frac{jI_0 l}{4\pi r} \eta k \sin \theta e^{-jkr} \hat{\boldsymbol{\theta}} \right) \times \left(\frac{jI_0 l}{4\pi r} k \sin \theta e^{-jkr} \hat{\boldsymbol{\phi}} \right)^* \right] \\ &= \frac{(I_0 l k)^2}{32 (\pi r)^2} \eta \sin^2 \theta \hat{\mathbf{r}} \end{aligned} \quad (2.1.17)$$

From equation 2.1.17 it can be seen that $\bar{\mathbf{S}}$ only has an $\hat{\mathbf{r}}$ -component, meaning power is propagating in the $\hat{\mathbf{r}}$ -direction. In the angular space the only dependency is on θ , resulting in a symmetry in the ϕ -plane. This equation follows an inverse square law with distance, as noted in section 2.1. The *radiation intensity* is a parameter similar to radiation density, but instead measures the power per unit solid angle, or steradian. The radiation intensity will assist in calculating directivity.

$$\begin{aligned} U &= r^2 \bar{S} \\ &= \frac{(I_0 l k)^2}{32 \pi^2} \eta \sin^2 \theta \end{aligned} \quad (2.1.18)$$

The total power radiated by the dipole can be determined by integrating $\bar{\mathbf{S}}$ over a closed spherical surface with radius r .

$$\begin{aligned}
P &= \oiint_S \bar{\mathbf{S}} \cdot d\mathbf{s} & (2.1.19) \\
&= \int_0^{2\pi} \int_0^\pi \bar{S}_r r^2 \sin \theta \, d\theta d\phi \\
&= \int_0^{2\pi} \int_0^\pi \frac{(I_0 l k)^2}{32\pi^2} \eta \sin^3 \theta \, d\theta d\phi \\
&= \frac{(I_0 l k)^2}{32\pi^2} \eta \int_0^{2\pi} \left[-\cos \theta + \frac{\cos^3 \theta}{3} \right]_0^\pi d\phi \\
&= \frac{(I_0 l k)^2}{32\pi^2} \eta \left[\frac{8\pi}{3} \right] \\
&= \frac{(I_0 l k)^2}{12\pi} \eta
\end{aligned}$$

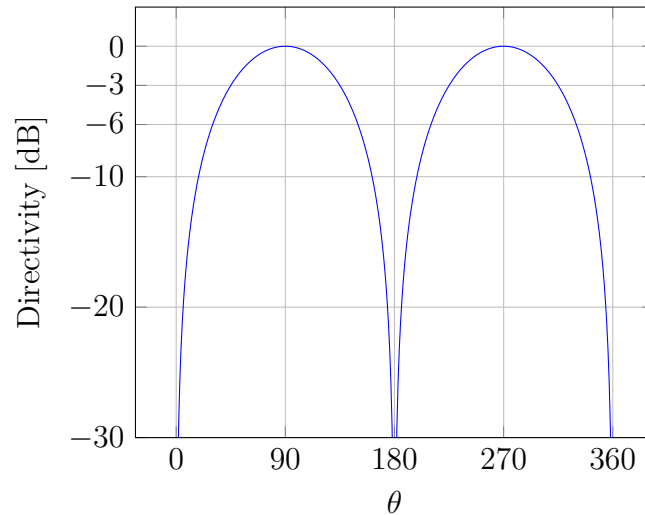


Figure 2.2: Hertzian dipole radiation pattern(Cartesian in dB, Normalised)

The *directivity* of an antenna is the radiation intensity in a certain direction divided by the average radiation intensity (Also given as $\frac{P}{4\pi}$). The direction implied is almost always the direction of maximum radiation intensity (Balanis, 2012).

$$\begin{aligned}
U_{max} &= U\left(\frac{\pi}{2}\right) = \frac{(I_0 l k)^2}{32\pi^2} \eta \\
D &= \frac{4\pi U_{max}}{P} \\
&= \frac{\frac{1}{8}}{\frac{1}{12}} \\
&= 1.5 \\
&= 1.7609 \text{ dB}
\end{aligned} \tag{2.1.20}$$

The Hertzian dipole is the simplest antenna to analyse in such a closed form solution. Most antenna elements are extremely difficult or impossible to be analysed in closed form and requires numerical solutions. The analysis of the Hertzian dipole in this section is merely to demonstrate some of the properties of antennas that will be referred to in this body of work. However, the Hertzian dipole has no practical value. The current distribution was assumed to be constant, which is practically impossible according to Balanis (2012). This is however helpful for analysing larger wire antennas that can be represented by many small Hertzian dipoles.

2.1.2 Omni-directional Antennas

Omnidirectional antennas, as mentioned before, radiates equally in a plane. The Hertzian dipole is an example of an omnidirectional antenna, even though it's purely theoretical. The *finite length dipole* is similar to the Hertzian dipole, although much harder to analyse mathematically and will not be derived here. According to Balanis (2012), the \mathbf{E} -field for a finite length dipole is given in the far-field region which simplifies to:

$$E_{\theta} \simeq j\eta \frac{I_0 e^{-jkr}}{2\pi r} \left[\frac{\cos\left(\frac{kl}{2} \cos \theta\right) - \cos \frac{kl}{2}}{\sin \theta} \right]$$

Then from equation 2.1.15:

$$H_{\phi} \simeq j \frac{I_0 e^{-jkr}}{2\pi r} \left[\frac{\cos\left(\frac{kl}{2} \cos \theta\right) - \cos \frac{kl}{2}}{\sin \theta} \right]$$

$\bar{\mathbf{S}}$ can then be calculated from equation 2.1.16:

$$\begin{aligned}
\bar{S} &= \frac{1}{2} \text{Re} \left[E_\theta \hat{\theta} \times H_\phi^* \hat{\phi} \right] \\
\bar{S}_r &= \frac{1}{2} \text{Re} \left[\left(j\eta \frac{I_0 e^{-jkr}}{2\pi r} \left[\frac{\cos\left(\frac{kl}{2} \cos \theta\right) - \cos \frac{kl}{2}}{\sin \theta} \right] \right) \left(-j \frac{I_0 e^{jkr}}{2\pi r} \left[\frac{\cos\left(\frac{kl}{2} \cos \theta\right) - \cos \frac{kl}{2}}{\sin \theta} \right] \right) \right] \\
&= \frac{1}{2} \text{Re} \left[\eta \frac{I_0^2}{(2\pi r)^2} \left[\frac{\cos\left(\frac{kl}{2} \cos \theta\right) - \cos \frac{kl}{2}}{\sin \theta} \right]^2 \right] \\
&= \eta \frac{I_0^2}{8(\pi r)^2} \left[\frac{\cos\left(\frac{kl}{2} \cos \theta\right) - \cos \frac{kl}{2}}{\sin \theta} \right]^2 \\
U &= r^2 \bar{S} \\
&= \eta \frac{I_0^2}{8\pi^2} \left[\frac{\cos\left(\frac{kl}{2} \cos \theta\right) - \cos \frac{kl}{2}}{\sin \theta} \right]^2
\end{aligned}$$

The next logical step would be to analyse the total radiated power using equation 2.1.19, however this yields a very complicated integral. Instead of solving this integral in closed form, numerical solutions will be obtained.

$$\begin{aligned}
P &= \int_0^{2\pi} \int_0^\pi \eta \frac{I_0^2}{8(\pi r)^2} \left[\frac{\cos\left(\frac{kl}{2} \cos \theta\right) - \cos \frac{kl}{2}}{\sin \theta} \right]^2 r^2 \sin \theta \, d\theta \, d\phi \\
&= \eta \frac{I_0^2}{8\pi^2} (2\pi) \int_0^\pi \frac{\left[\cos\left(\frac{kl}{2} \cos \theta\right) - \cos \frac{kl}{2} \right]^2}{\sin \theta} \, d\theta \\
&= \eta \frac{I_0^2}{4\pi} \int_0^\pi \frac{\left[\cos\left(\frac{kl}{2} \cos \theta\right) - \cos \frac{kl}{2} \right]^2}{\sin \theta} \, d\theta \tag{2.1.21}
\end{aligned}$$

Table 2.1 shows solutions of equation 2.1.21 for some values of l . These values can be used in equation 2.1.20 to calculate the directivity. For example, for $l = \frac{\lambda}{4}$:

Dipole Length	U_{max}	P	D	D [dB]
$l = \frac{\lambda}{4}$	$\eta \frac{I_0^2}{8\pi^2} (0.0858)$	$\eta \frac{I_0^2}{4\pi} (0.112)$	1.5321	1.8529
$l = \frac{\lambda}{2}$	$\eta \frac{I_0^2}{8\pi^2} (1)$	$\eta \frac{I_0^2}{4\pi} (1.21883)$	1.6409	2.1508
$l = \frac{3\lambda}{4}$	$\eta \frac{I_0^2}{8\pi^2} (2.9142)$	$\eta \frac{I_0^2}{4\pi} (3.09681)$	1.8821	2.7464
λ	$\eta \frac{I_0^2}{8\pi^2} (4)$	$\eta \frac{I_0^2}{4\pi} (3.31813)$	2.411	3.822
1.25λ	$\eta \frac{I_0^2}{8\pi^2} (2.9142)$	$\eta \frac{I_0^2}{4\pi} (1.77562)$	3.2825	5.162

Table 2.1: Finite length dipoles

$$\begin{aligned}
D(\theta, \phi) &= 4\pi \frac{U(\theta, \phi)}{P} \\
&= 4\pi \frac{\eta \frac{I_0^2}{8\pi^2} \left[\frac{\cos(\frac{\pi}{4} \cos \theta) - \cos \frac{\pi}{4}}{\sin \theta} \right]^2}{\eta \frac{I_0^2}{4\pi} (0.112)} \\
&= \frac{\frac{1}{2\pi} \left[\frac{\cos(\frac{\pi}{4} \cos \theta) - \cos \frac{\pi}{4}}{\sin \theta} \right]^2}{\frac{1}{4\pi} (0.112)} \\
&= 17.8571 \left[\frac{\cos(\frac{\pi}{4} \cos \theta) - \cos \frac{\pi}{4}}{\sin \theta} \right]^2
\end{aligned}$$

2.1.3 Directional Antennas

When looking at figure 2.3 and figure 2.4, it would seem that the dipole exhibits some directionality. It should be noted that the directivity has no ϕ -dependency, meaning it is completely symmetrical in the ϕ -plane.

A directional antenna typically has only one axis-symmetry.

One of the most well-understood and widely used directional antennas is the helical antenna. This antenna was first proven to work and subsequently popularised by Kraus (1950). The geometry of the helical antenna is fairly simple, consisting of a wire wound in a helical shape as shown in figure 2.5. At the base of the helix, there is a circular ground plane. The wire is fed through the ground plane by some coaxial method, where the ground is attached to the ground plane.

The helical structure has a spacing S between N turns. The diameter of the turns is D . Figure 2.5 also shows the relationship between S , D and L ,

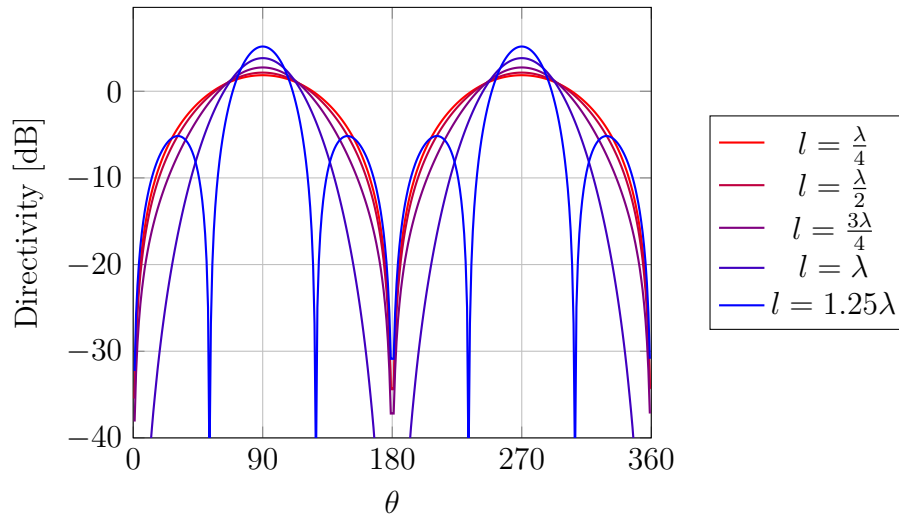


Figure 2.3: Finite length dipoles directivity(Cartesian in dB)

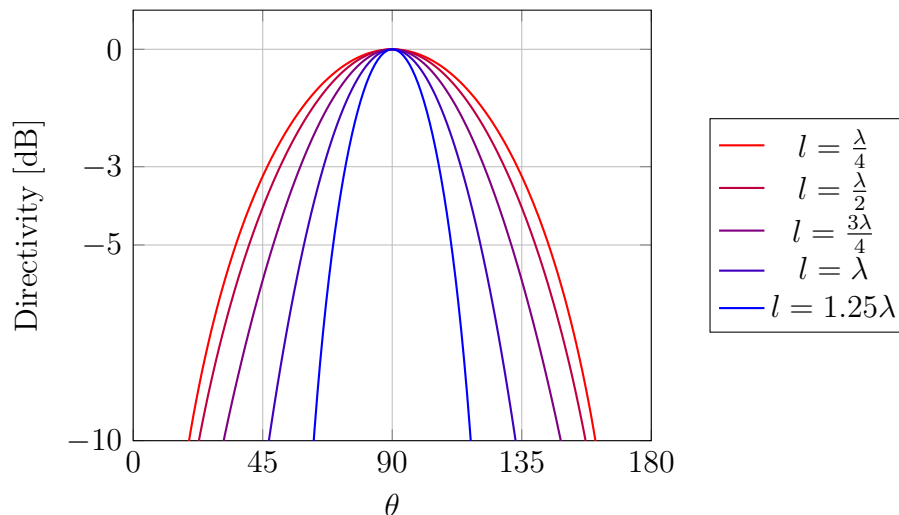


Figure 2.4: Finite length dipoles directivity(Cartesian in dB, normalised)

the length of wire in one turn, and α , the pitch of the wire. By changing D , S , and N , the radiation characteristics can be controlled.

The helical antenna can operate in normal and axial mode. When operating in normal mode, the radiation pattern is similar to a dipole and is more omnidirectional. This is accomplished when $NL \ll \lambda$. Axial mode is of more interest for this section as it exhibits directional radiation patterns. In order to operate in axial mode, the following parameters are suggested by Kraus (1950) and similarly by Balanis (2012):

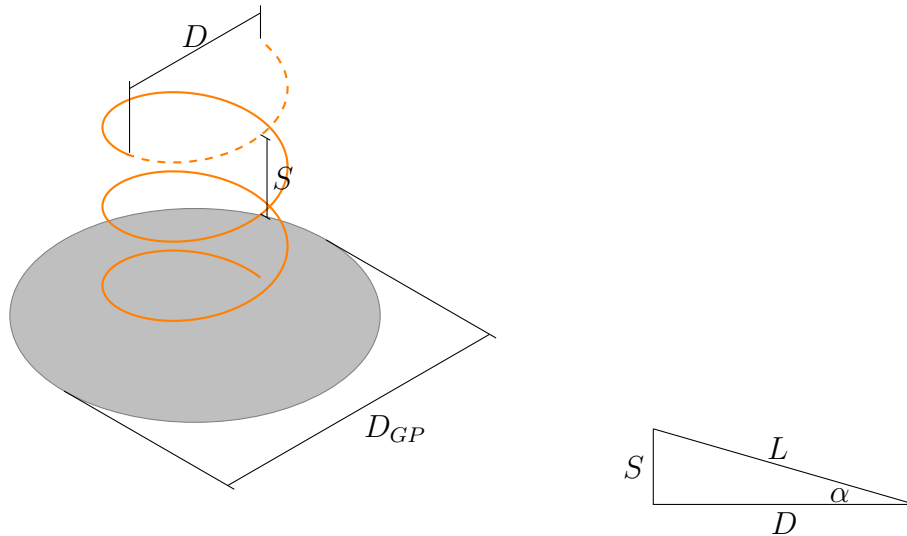


Figure 2.5: Geometrical description of the helical antenna

$$\begin{aligned}
 C &= \pi D \\
 \frac{3}{4} &< \frac{C}{\lambda} < \frac{4}{3} \\
 12^\circ &< \alpha < 14^\circ \\
 n &\geq 4 \\
 D_{GP} &> \frac{\lambda}{2}
 \end{aligned}$$

Closed form solutions for this type of antenna are almost impossible to obtain. Kraus (1950) also suggests some design equations that approximate some performance parameters and are very useful as a starting point. Design equations need to be supported by simulations, and especially full wave 3D simulations. 3D electromagnetic simulation software is much more available nowadays, making the use of complicated closed form solutions mostly redundant.

$$\begin{aligned}
 \text{HPBW} &\simeq \frac{52}{\frac{c}{\lambda} \sqrt{\frac{nS}{\lambda}}} \\
 \text{Directivity} &\simeq 15 \frac{CnS}{\lambda^3} \\
 R &= 140 \frac{C}{\lambda}
 \end{aligned}$$

The real part of the input impedance dominates and is typically between 100Ω and 200Ω . By paying close attention to the feed structure, this can be lowered, even to 50Ω (Balanis, 2012).

Another very widely used directional antenna is the microstrip antenna, also known as the patch antenna. It consists of a planar conductor in some geometric shape placed parallel above a ground plane. The distance between the shape and the ground plane is typically between 0.003 and 0.05 free-space wavelengths (Balanis, 2012), and is usually filled with a substrate with $2.2 \leq \epsilon_r \leq 12$.

There are a variety of shapes that have good radiation characteristics but the most common shape is a rectangular patch. The four most widely used feed methods, according to Balanis (2012), are the microstrip line, coaxial probe, aperture coupling and proximity coupling. Figures 2.6 and 2.7 show rectangular patches with two different feed structures that are easy to optimise and are widely used due to their low cost and ease of implementation. The important parameter to optimise in these feed structures is the inset position, indicated with i , which directly influences the input impedance.

In the case of the probe-fed patch, a hole is required at the inset position to attach the centre conductor of a coaxial cable. The ground of the coaxial cable must be attached to the ground plane. In the case of a line-fed patch, a microstrip transmission line attaches to the inset position.

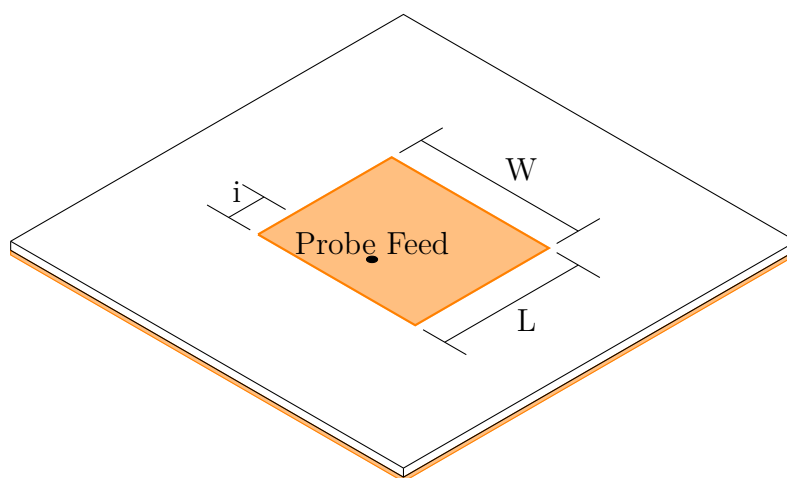


Figure 2.6: Geometrical description of a probe-fed, rectangular microstrip patch antenna

Design equations exist and are used with very good results for the design of a patch antenna. These equations, along with the design, simulation and prototyping of a probe-fed rectangular patch are covered in section 4.3.3.

2.1.4 Antenna Arrays

Many different antenna elements were discussed in sections 2.1.1, 2.1.2 and 2.1.3. The elements listed are some of the most widely used and well understood elements. Using each element on its own may not necessarily provide

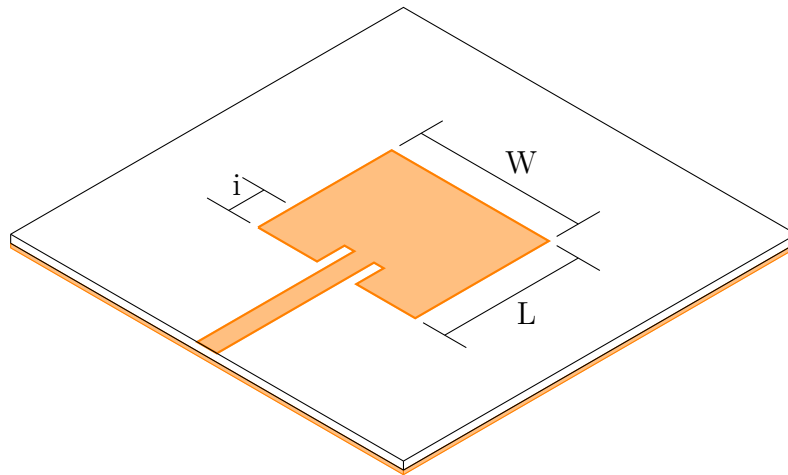


Figure 2.7: Geometrical description of a line-fed, rectangular microstrip patch antenna

the performance that is required in a system. This leads to the concept of antenna arrays, where multiple antenna elements (typically of the same type), are arranged in certain ways to sum up to one larger antenna element. There are many different ways to arrange the individual elements, some of which will be discussed.

The simplest array is the linear array, which consists of multiple antenna elements spaced along an axis, separated by a distance d .

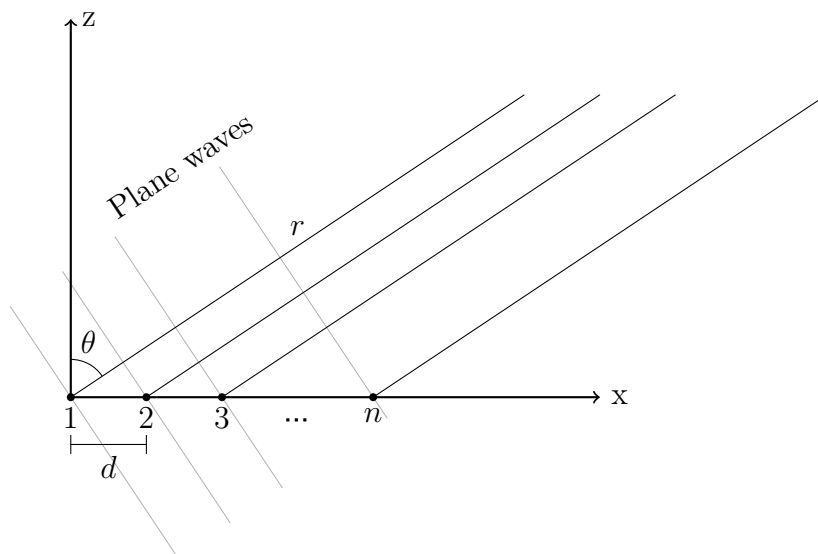


Figure 2.8: Linear array (far-field approximation)

Each element is excited with the same amplitude E_m , but the phase in element 2 leads that of 1 by ξ_2 (Cheng, 2014). Similarly, the phase in element

n leads that of 1 by ξ_n . $F(\theta)$ is the element pattern, that describes the radiation pattern of a single element. In the case of the Hertzian dipole, it is equation 2.1.13. An array can be analysed irrespective of its element patterns, by separating the element pattern from the *array factor*. The array factor is a function that describes the behaviour of the array as a result of the following properties of the array, as suggested by Balanis (2012):

- Geometrical placement
- Spacing
- Number of elements
- Element excitation (Magnitude and phase)

Consider the array shown in figure 2.8. The E -field in the far field for each element is:

$$E_1 = E_m F(\theta) \frac{e^{-jkr}}{r}$$

Analysing this array in the far field (in the xz/θ /elevation plane), the total E -field can be written as:

$$E_t = E_m \frac{F(\theta)}{r} e^{-jkr} [1 + e^{jkd \sin \theta} e^{j\xi_2} + e^{j2kd \sin \theta} e^{j\xi_3} + \dots + e^{j(n-1)kd \sin \theta} e^{j\xi_n}] \quad (2.1.22)$$

$$= E_m \frac{F(\theta)}{r} e^{-jkr} \sum_{N=1}^n e^{j(N-1)kd \sin \theta} e^{j\xi_N}$$

Thus the array factor is:

$$AF = \sum_{N=1}^n e^{j(N-1)kd \sin \theta} e^{j\xi_N} \quad (2.1.23)$$

The phase term introduced by the array, $e^{j(N-1)kd \sin \theta}$, originates from the extra distance that a plane wave needs to travel (after reaching element n) when approaching from an angle θ , to reach element 1, the reference element. In this section it will be assumed that all the excitations are in phase, thus ξ_2 to ξ_n is zero. Arrays with non-zero phase excitations are known as *phased arrays* and are discussed in section 2.2.1.

To see the individual effect of the array factor, simply plot the magnitude, $|AF|$:

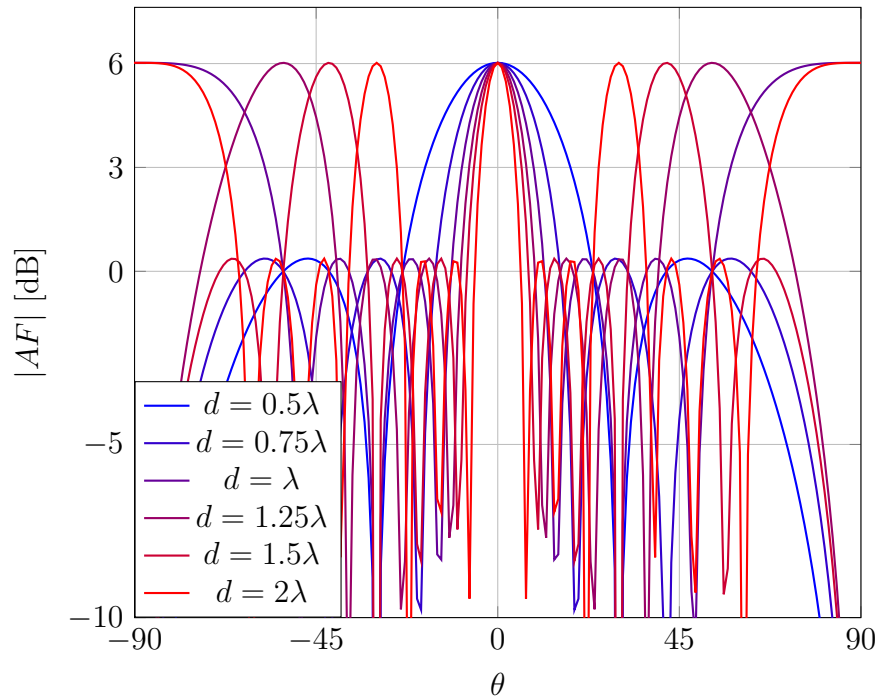
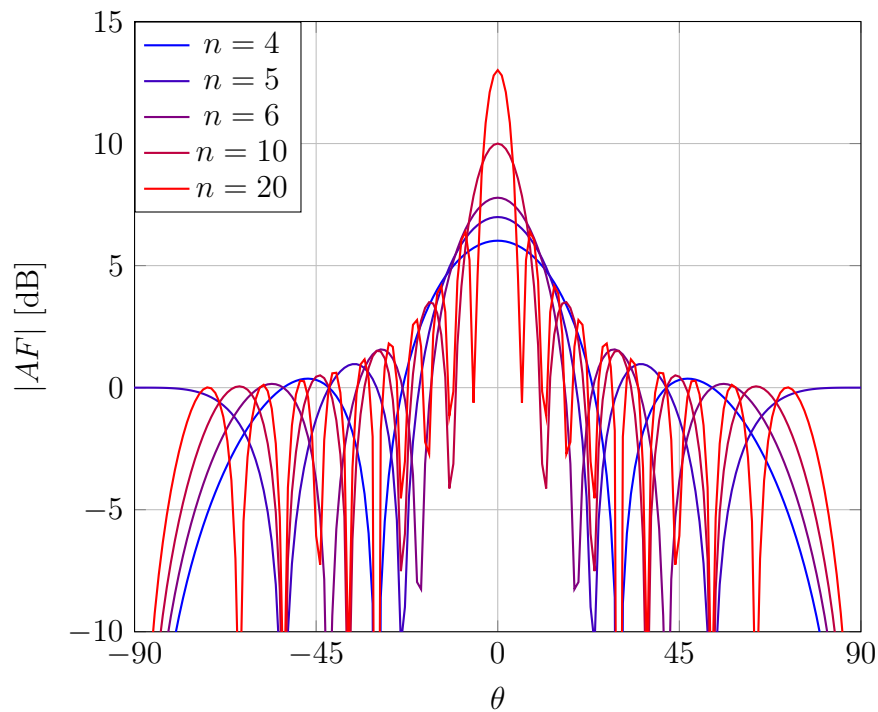
Figure 2.9: $|AF|$ for varying d , $n = 4$

Figure 2.9 and figure 2.10 shows $|AF|$ for different steps of d and n . Increasing d increases the amount of sidelobes that are introduced, and decreases the *HPBW*. Increasing n increases gain at the cost of *HPBW*. These two figures only plot the pattern from -90° to 90° . The array factor in this case is mirrored through the xy -plane, so it will have the pattern repeated from 90° to 270° . When the main lobe is pointing perpendicular to the axis on which the array is arranged, it is a *broadside array*, and when it is pointing along the axis, it is an *endfire array*.

A derivation of the array factor of a planar array, which will be useful in further sections can be found in Appendix A.

2.2 Beamforming

The concept of antenna arrays were introduced in section 2.1.4. The term *phased arrays* was used to describe arrays with non-zero phase excitations. Most arrays, especially phased arrays, need some form of *feed network*, that manipulate the signals that are fed to the antenna elements. This can consist of amplitude weighting, time delays, phase shifts, and splitting and combining of power, as suggested by Mailloux (2005). The feed network that does this is commonly referred to as a *beamforming network (BFN)*.

Figure 2.10: $|AF|$ for varying n , $d = 0.5\lambda$

2.2.1 Phased Arrays

Phased arrays are the simplest BFN's, aside from what was discussed in section 2.1.4, which could be considered a BFN as it involves a power combiner to combine the signals from the individual elements. In this section the concept is expanded and a phase shift is added.

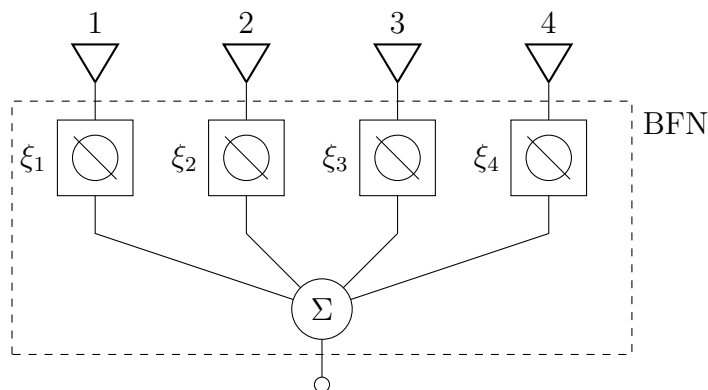


Figure 2.11: 4-element BFN

Figure 2.11 shows a basic 4-element BFN, on which the following analysis will be based. Element 1 is chosen as the phase reference, thus $\xi_1 = 0$.

The phase shift ξ_N is chosen to cancel out its corresponding phase term, $e^{j(N-1)kd \sin \theta}$, in the array factor equation 2.1.23. Cancelling out the aforementioned phase term makes it appear from the point of the antenna that the direction of arrival of a plane wave approaching from θ_0 is actually $\theta = 0^\circ$.

$$\xi_N = -(N - 1)kd \sin \theta_0 \quad (2.2.1)$$

$$\xi_2 = -kd \sin \theta_0$$

$$\xi_3 = -2kd \sin \theta_0$$

$$\xi_4 = -3kd \sin \theta_0$$

To illustrate an example, $|AF|$ is shown in figure 2.12, with different values for θ_0 . Some interesting things to note, with $\theta_0 = 0^\circ$, the array is a broadside array, and for $\theta_0 = 90^\circ$, the array is an endfire array.

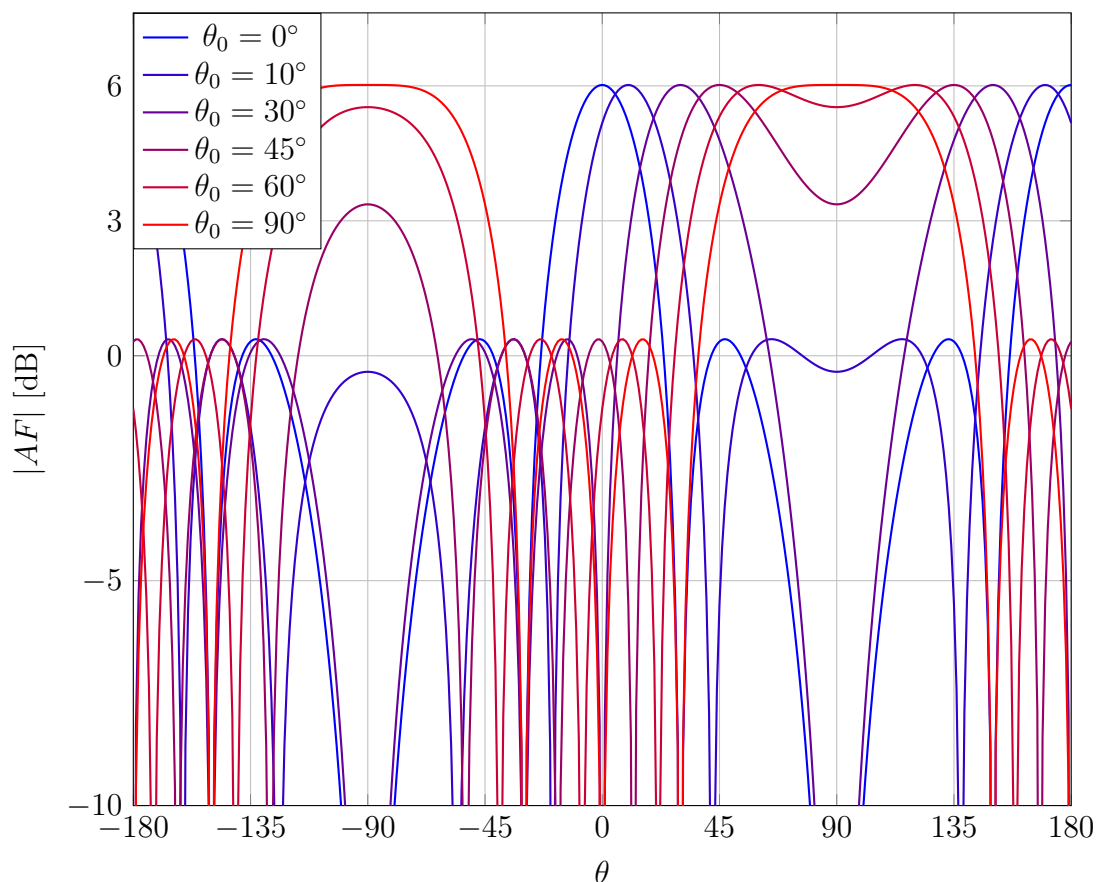


Figure 2.12: $|AF|$ for varying θ_0 , $n = 4$, $d = \frac{\lambda}{2}$

The difference between ξ_2 and ξ_1 , or more generally, $\xi_p = \xi_N - \xi_{N-1}$, is known as the progressive phase difference. For a uniform phased array, ξ_p is constant between all elements, which will be the case for most arrays.

There are limitations to what values can be chosen for θ_0 . Solving for θ_0 in equation 2.2.1:

$$\begin{aligned}\xi_N &= -(N-1)kd \sin \theta_0 \\ \xi_p &= \xi_2 = -kd \sin \theta_0\end{aligned}\quad (2.2.2)$$

$$\theta_0 = \sin^{-1} \left[\frac{-\xi_p}{kd} \right] \quad (2.2.3)$$

The argument in the arcsin function is bound to the conditions:

$$-1 \leq \frac{-\xi_p}{kd} \leq 1 \quad (2.2.4)$$

$$-kd \leq -\xi_p \leq kd \quad (2.2.5)$$

k is the wavenumber, thus $k = \frac{2\pi}{\lambda}$, and d is almost always chosen in terms of wavelength, thus kd is replaced with $2\pi i$, where i is the spacing d in terms of wavelengths:

$$i = \frac{d}{\lambda}$$

Rewriting equation 2.2.5:

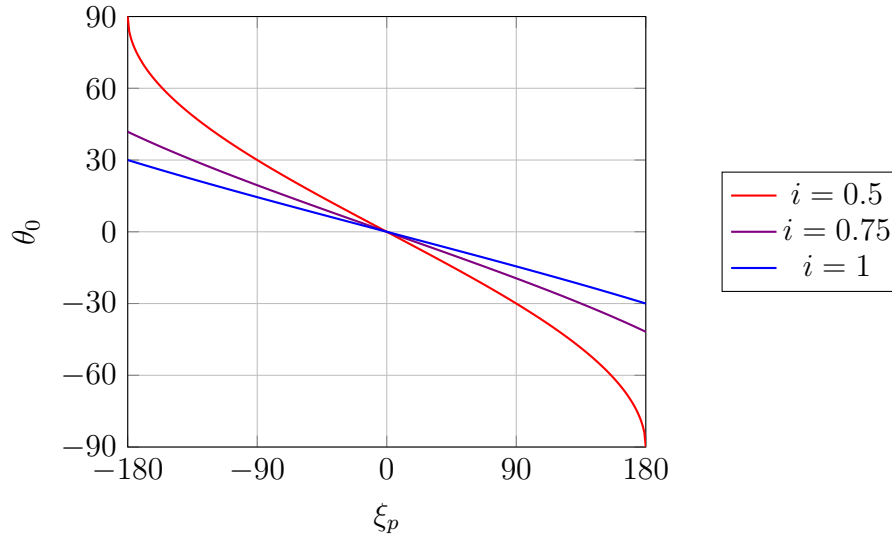
$$-2\pi i \leq \xi_p \leq 2\pi i$$

Figure 2.13 shows some possible combinations of i and ξ_p for a resulting θ_0 .

Any type of device that has a structure that is related to wavelength will be frequency-dependent. The phased array is no exception. If a system is designed to operate at a centre frequency f_c , with bandwidth B , then two frequency points can be defined as the lower and upper edges of the operating frequency band:

$$\begin{aligned}f_L &= f_c - \frac{B}{2} \\ f_H &= f_c + \frac{B}{2}\end{aligned}$$

Which leads to their respective wavelengths λ_L and λ_H .

Figure 2.13: Limits of scan angle θ_0 for varying i

$$\begin{aligned}\lambda_L &= \frac{f_L}{c_0} = \frac{f_c - \frac{B}{2}}{c_0} \\ &= \lambda_c - \frac{B}{2c_0} \\ \lambda_H &= \frac{f_H}{c_0} = \frac{f_c + \frac{B}{2}}{c_0} \\ &= \lambda_c + \frac{B}{2c_0}\end{aligned}$$

With bandwidth as a percentage of the centre frequency:

$$\begin{aligned}B_{\%} &= \frac{B}{f_c} \\ \lambda_L &= \frac{f_L}{c_0} = \frac{f_c - \frac{B_{\%}f_c}{2}}{c_0} \\ &= \lambda_c \left(1 - \frac{B_{\%}}{2}\right) \\ \lambda_H &= \frac{f_H}{c_0} = \frac{f_c + \frac{B_{\%}f_c}{2}}{c_0} \\ &= \lambda_c \left(1 + \frac{B_{\%}}{2}\right)\end{aligned}$$

Since the system is designed to operate at f_c , it will have a corresponding spacing d related to the wavelength of f_c , and subsequently a progressive phase

difference ξ_p will be calculated as in equation 2.2.2, for a given θ_0 . equation 2.2.3 can be rewritten to include the effect of frequency change:

$$\begin{aligned}\theta_L &= \sin^{-1} \left[\frac{-\xi_p}{\frac{2\pi}{\lambda_L} i \lambda_c} \right] \\ &= \sin^{-1} \left[\frac{-\xi_p}{\frac{2\pi}{\lambda_c \left(1 - \frac{B\%}{2}\right)} i \lambda_c} \right] \\ &= \sin^{-1} \left[\frac{-\xi_p \left(1 - \frac{B\%}{2}\right)}{2\pi i} \right]\end{aligned}$$

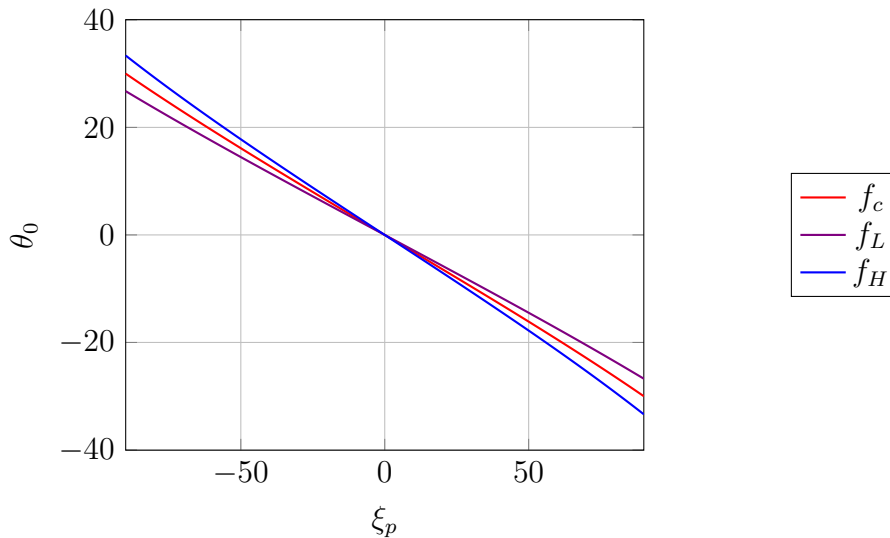


Figure 2.14: Change in scan angle θ_0 over frequency, $i = 0.5$, $B\% = 0.2$

Figure 2.14 shows an example of a phased array, designed for 20% bandwidth. The spacing between elements is $d = \frac{\lambda}{2}$. The scan angle with $\xi_p = -60^\circ$ is about 2° below and above its normal value for f_L and f_H respectively. This might seem like a small error, but as the bandwidth increases, or the beamwidth decreases, this effect becomes significant.

2.2.2 Multiple Beam Array

One of the simplest BFN's, the phased array, is discussed in section 2.2.1. Figure 2.15 shows a multiple beam array, which is very similar to the phased array, except that it has multiple beam ports, according to Mailloux (2005).

Basically, power from the antenna element is divided equally by N (for N beams), and every beam is fed through its own phased array network.

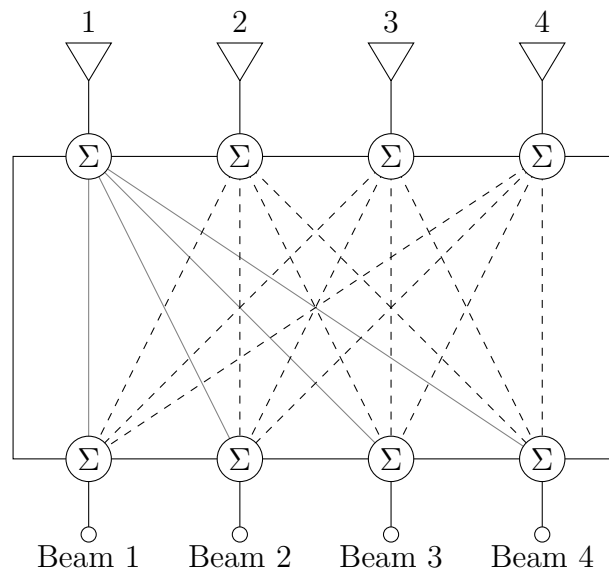


Figure 2.15: Example of a 4-element Multiple beam beamformer

Every Σ block is a power splitter/combiner, and every dashed line has a phase shifter. This network uses 4 power splitters, 4 power combiners, and 12 phase shifters, which is a high component count as stated by Bhattacharyya (2006). The Butler Matrix is a multiple beam BFN (MBBFN) that can implement the network in figure 2.15 much more efficiently, and will be discussed in detail in Chapter 3.

An important parameter of multiple beam BFN's is *beam crossover level*, which is the point at which two adjacent beams cross. BFN's should be designed in a way to maximise angular coverage, but still consider the beam crossover level as not to cause dips in gain.

2.2.3 Digital Beamforming

A digital beamformer is a BFN that exists mostly in the digital domain. Where a conventional BFN employs phase shifters and power dividers and combiners in the RF domain, a digital BFN (DBFN) digitizes the signal, and through complex algorithms apply phase shifts and other mathematical operations to have the desired beam formed.

The digitizing section requires an analog-to-digital converter (ADC) for each antenna element. Due to limitations in ADC technology, it is not always feasible or possible to directly convert the radio frequency (RF) signal into the digital domain. A downconverter needs to be placed after the antenna

element, converting the RF to an intermediate frequency (IF). The downconverter, along with low noise amplifiers (LNA) and IF filters are included in the RF block in figure 2.16.

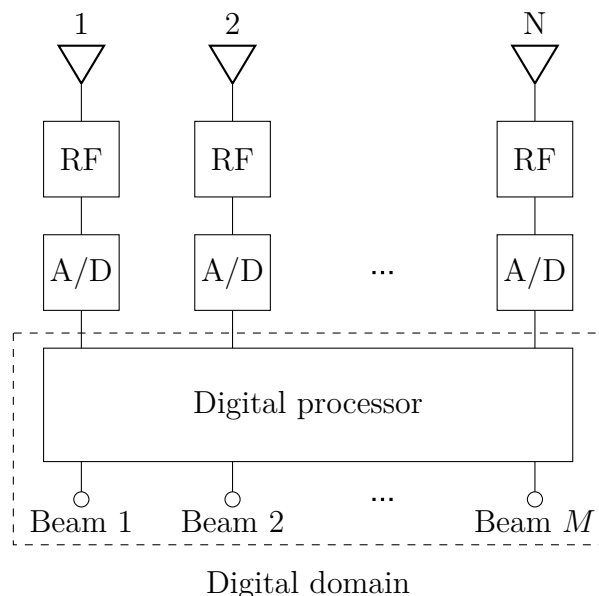


Figure 2.16: Digital beamformer - receive array

The designer of such a system will go to many lengths to insure that every one of the RF and digitizing chains are identical, but practically speaking this is extremely hard to achieve. However, since most of this beamformer is digital, thus the errors in the physical system can easily be calibrated out, or corrected for in software, as suggested by Litva and Lo (1996).

The “beam” formed by a DBFN is different from a conventional beam, as it exists in the digital domain only. This can be a great advantage, as most processing (demodulating, correlating, etc.) that is done on RF signals nowadays is done in the digital domain anyway. Since this digital beam is now already in the digital domain, it can easily be passed on to many endpoints.

All the (electromagnetic) information that is incident on each of the antenna elements, and within the operating range of the RF front-end and ADC’s, is captured. This makes the DBFN the most flexible of any BFN, as any digital processing can be done on the incoming information, limited only by the memory, speed and data bandwidth of the processor. There is also no need for power splitters to implement multiple simultaneous beams, as the incoming data can just be copied as many times as needed and processed in parallel, given enough processing power.

In a conventional BFN, the time to process a signal from arriving at the antenna until it exits the beam port happens at the speed of light. This is not

the case with DBFN, as some time is required for analog to digital conversion and processing. Most cases where BFN's and DBFN's are used, real-time operation is required, but fields such as radio astronomy do not necessarily require real-time operation. The data can be stored and processed over a longer period of time. This has the advantage of being able to run different algorithms on exactly the same data, especially when very complex algorithms are utilised that require a lot of processing power and can thus not be run in parallel. Storing the data also allows operations to be done on data sets from different locations and even times, this is very useful in radio astronomy.

Processing power is one of the biggest obstacles for DBFN's. This is becoming less and less of a problem as field programmable gate array (FPGA) technology is becoming much more widely available, especially System-on-Chip (SoC) technology. An SoC can incorporate a complete system from the RF chain to the application processor in one single chip, greatly reducing on power consumption and BOM cost.

Chapter 3

The Butler Matrix

This chapter will describe the Butler Matrix concept and analyse the theory behind it. The orthogonality principle will then be applied. A general derivation for a N^{th} -order Butler Matrix will be done, followed by a brief discussion about the equivalence between the Butler Matrix and the Fourier Transform.

3.1 Concept

The Butler Matrix is a BFN that was first described by Butler and Lowe (1961). It is essentially a more efficient version of the BFN mentioned in section 2.2.2. The number of beams, N , are equal to the number of antenna elements, $N = 2^m$, where m is a positive integer. According to Mailloux (2005), the Butler Matrix is an implementation of the *Fast Fourier Transform* (FFT), meaning it is also the most efficient implementation with regards to computations (power combiners/splitters/phase shifters). One drawback of this BFN is that the beams are fixed.

3.2 Derivation

Figure 3.1 is similar (if not identical) to figure 2.15. The concept is that beam port 1, or B_1 , represents an 4-element phased array, with complex weights $\mathbf{a} = [a_1 \ a_2 \ a_3 \ a_4]$. Assuming uniform amplitude excitation at the element ports, the array factor is:

$$AF_{B_1} = \sum_{n=1}^4 e^{j(n-1)kd \sin \theta} e^{j\psi_a(n-1)} \quad (3.2.1)$$

In equation 3.2.1, ψ_a is the progressive phase shift between element ports. Similarly for B_2 to B_4 , the array factor can be written, with ψ_b , ψ_c , and ψ_d as the progressive phase shifts. There will be a total of 12 (the first element

in the excitation vector is always 1) complex excitation vectors defined for a 4-element BFN like the one shown in figure 3.1.

$$\mathbf{a} = [a_1 \ a_2 \ a_3 \ a_4] = [1 \ e^{j\psi_a} \ e^{j2\psi_a} \ e^{j3\psi_a}] \quad (3.2.2)$$

$$\mathbf{b} = [b_1 \ b_2 \ b_3 \ b_4] = [1 \ e^{j\psi_b} \ e^{j2\psi_b} \ e^{j3\psi_b}] \quad (3.2.3)$$

$$\mathbf{c} = [c_1 \ c_2 \ c_3 \ c_4] = [1 \ e^{j\psi_c} \ e^{j2\psi_c} \ e^{j3\psi_c}] \quad (3.2.4)$$

$$\mathbf{d} = [d_1 \ d_2 \ d_3 \ d_4] = [1 \ e^{j\psi_d} \ e^{j2\psi_d} \ e^{j3\psi_d}] \quad (3.2.5)$$

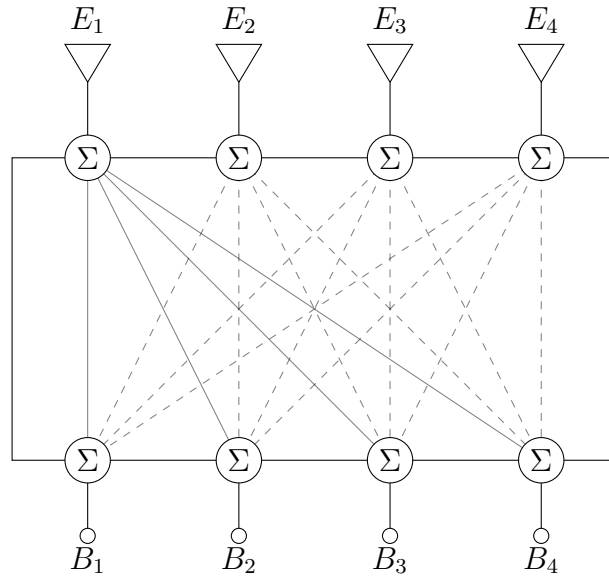


Figure 3.1: Example of a 4-element Butler Matrix

3.2.1 Orthogonality

The beams generated by the Butler matrix are orthogonal. When applying a signal to a specific beam port on an orthogonal BFN, that signal will only appear at the beam associated with that beam port, according to Hansen (2009). In simple terms, the beam ports are isolated. For the BFN in figure 3.1 to be orthogonal, equation 3.2.6 must hold:

$$\sum_{n=1}^4 a_n b_n^* = \sum_{n=1}^4 a_n c_n^* = \sum_{n=1}^4 a_n d_n^* = 0 \quad (3.2.6)$$

Equation 3.2.6 can be written in vector form, where $\bar{\mathbf{b}}$ represents the complex conjugate of the vector \mathbf{b} .

$$\mathbf{a} \cdot \bar{\mathbf{b}} = 0 \quad (3.2.7)$$

$$\mathbf{a} \cdot \bar{\mathbf{c}} = 0 \quad (3.2.8)$$

$$\mathbf{a} \cdot \bar{\mathbf{d}} = 0 \quad (3.2.9)$$

From equation 2.2.1 the progressive phase difference is:

$$\psi_a = -kd \sin \theta_a \quad (3.2.10)$$

where θ_a is the direction of the main beam associated with B_1 . Similar steps can be followed for ψ_b , ψ_c , and ψ_d :

$$\psi_b = -kd \sin \theta_b \quad (3.2.11)$$

$$\psi_c = -kd \sin \theta_c \quad (3.2.12)$$

$$\psi_d = -kd \sin \theta_d \quad (3.2.13)$$

Solve for $\mathbf{a} \cdot \bar{\mathbf{b}}$:

$$\mathbf{a} \cdot \bar{\mathbf{b}} = 1 + e^{j\psi_a} e^{-j\psi_b} + e^{j2\psi_a} e^{-j2\psi_b} + e^{j3\psi_a} e^{-j3\psi_b} \quad (3.2.14)$$

$$= 1 + e^{j(\psi_a - \psi_b)} + e^{j2(\psi_a - \psi_b)} + e^{j3(\psi_a - \psi_b)} \quad (3.2.15)$$

Equation 3.2.15 is a geometric series in the form $\sum_{k=0}^{n-1} ar^k = a \left(\frac{1-r^n}{1-r} \right)$, and can be written as:

$$\sum_{n=0}^3 e^{jn(\psi_a - \psi_b)} = \frac{1 - e^{j4(\psi_a - \psi_b)}}{1 - e^{j(\psi_a - \psi_b)}} \quad (3.2.16)$$

So to satisfy orthogonality between \mathbf{a} and \mathbf{b} :

$$\mathbf{a} \cdot \bar{\mathbf{b}} = \frac{1 - e^{j4(\psi_a - \psi_b)}}{1 - e^{j(\psi_a - \psi_b)}} = 0 \quad (3.2.17)$$

Two conditions need to hold:

$$1. e^{j4(\psi_a - \psi_b)} = 1$$

$$2. e^{j(\psi_a - \psi_b)} \neq 1$$

The solution to condition 1 is:

$$4(\psi_a - \psi_b) = 2m\pi \quad (3.2.18)$$

$$(\psi_a - \psi_b) = \frac{m\pi}{2} \quad (3.2.19)$$

$$m = 0, 1, 2 \dots \quad (3.2.20)$$

Condition 2 will only be violated when:

$$m = 0, 4, 8 \dots \quad (3.2.21)$$

Thus ψ_b can be rewritten in terms of ψ_a :

$$\psi_b = \psi_a - \frac{m\pi}{2} \quad (3.2.22)$$

To conclude, both conditions will be satisfied for any integer value of m , except 0, and multiples of 4. The same steps followed from equation 3.2.17 onward can be followed for dot-products between all the excitation vectors.

$$\psi_c = \psi_a - \frac{k\pi}{2} \quad (3.2.23)$$

$$\psi_d = \psi_a - \frac{p\pi}{2} \quad (3.2.24)$$

The constants k and p are chosen in a similar fashion than m . Each beam's progressive phase shift must be different, thus $m \neq k \neq p$. As an easy example, the constants are chosen as $m = 1$, $k = 2$ and $p = 3$.

$$\psi_a = -kd \sin \theta_a \quad (3.2.25)$$

$$\psi_b = \psi_a - \frac{\pi}{2} \quad (3.2.26)$$

$$\psi_c = \psi_a - \pi \quad (3.2.27)$$

$$\psi_d = \psi_a - \frac{3\pi}{2} \quad (3.2.28)$$

Following equations 3.2.11, 3.2.12, and 3.2.13, the beam angles associated with the specific beam ports can now be calculated. An interesting observation made by Bhattacharyya (2006) is that the beams are spaced equally in $\sin \theta$ -space, leading to:

$$\Delta \sin \theta_{peak} = \frac{\pi}{2kd}$$

3.2.2 Limitations

The same limitation that was laid out in equation 2.2.5 for the progressive phase shift ξ_p , applies to all the phase shifts ψ_a to ψ_d . To simplify the equations further, $kd = 2\pi i$, where i is element spacing in terms of wavelength.

$$\theta_a = \sin^{-1} \left[\frac{-\psi_a}{2\pi i} \right] \quad (3.2.29)$$

$$\sin \theta_b = \frac{-\psi_b}{2\pi i} = \left(\sin \theta_a + \frac{1}{4i} \right) \quad (3.2.30)$$

$$\sin \theta_c = \frac{-\psi_c}{2\pi i} = \left(\sin \theta_a + \frac{1}{2i} \right) \quad (3.2.31)$$

$$\sin \theta_d = \frac{-\psi_d}{2\pi i} = \left(\sin \theta_a + \frac{3}{4i} \right) \quad (3.2.32)$$

The progressive phase shift that will be the first to fail the inequality is ψ_d .

$$\begin{aligned} -1 &\leq \sin \theta_d \leq 1 \\ -1 &\leq \left(\sin \theta_a + \frac{3}{4i} \right) \leq 1 \end{aligned}$$

Equation 3.2.32 shows the relationship between $\sin \theta_d$ and $\sin \theta_a$ for a given i . The range of $\sin \theta_d$ is shown in figure 3.2, over θ_a and for possible values of element spacing. This illustrates the limitation when choosing the element spacing and beam angle θ_a , as $\sin \theta_d$ cannot violate the inequality in equation 3.2.33.

3.2.3 Generalised Derivation

It is possible to derive equations for progressive phase shift for a orthogonal BFN with N beam ports (Bhattacharyya, 2006). Equation 3.2.16 can be written for N antennas elements:

$$\sum_{n=0}^{N-1} e^{jn(\psi_a - \psi_b)} = \frac{1 - e^{jN(\psi_a - \psi_b)}}{1 - e^{j(\psi_a - \psi_b)}} \quad (3.2.33)$$

Orthogonality must be proved between vectors **a** and **b**, **a** and **c** and between **a** and every N subsequent vector.

$$\psi_b = \psi_a - \frac{2m\pi}{N} \quad (3.2.34)$$

$$m = 1, 2, 3, \dots \quad m \neq 0, N, 2N, \dots \quad (3.2.35)$$

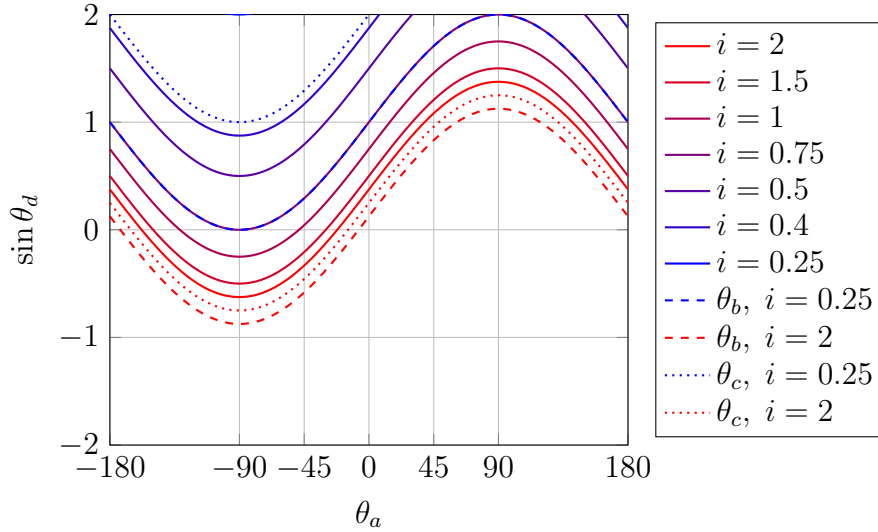


Figure 3.2: Valid region for orthogonality condition

Dot product	Progressive phase shift	Constant
$\mathbf{a} \cdot \bar{\mathbf{b}}$	$\psi_b = \psi_a - \frac{2m_1\pi}{N}$	$m_1 = 1$
$\mathbf{a} \cdot \bar{\mathbf{c}}$	$\psi_c = \psi_a - \frac{2m_2\pi}{N}$	$m_2 = 2$
$\mathbf{a} \cdot \bar{\mathbf{d}}$	$\psi_d = \psi_a - \frac{2m_3\pi}{N}$	$m_3 = 3$
...		
$\mathbf{a} \cdot \overline{(\mathbf{N}_{th} \text{vector})}$	$\psi_{N_{th}} = \psi_a - \frac{2m_{N-1}\pi}{N}$	$m_{N-1} = N - 1$

Table 3.1: Dot products for an N beam BFN

It can be seen that there is a constant difference between ψ_b and ψ_a , ψ_c and ψ_b , and ψ_N and ψ_{N-1} . From table 3.1 this progression is $\frac{2\pi}{N}$. The spacing of main beams can then be written as:

$$\Delta \sin \theta_{peak} = \frac{2\pi}{Nkd}$$

3.3 Fourier Transform Equivalence

The *Fourier Transform* is a well known transformation from the time domain to the frequency domain. It has uses in transformations in other domains as well. In the case of the Butler Matrix, it relates the beam port voltages and

the element port voltages (Bhattacharyya, 2006). Examining figure 3.1 from the element port side, with non-uniform amplitude excitations, yields:

$$E_1 = V_1 e^{j\psi_{a1}} + V_2 e^{j\psi_{b1}} + V_3 e^{j\psi_{c1}} + V_4 e^{j\psi_{d1}} \quad (3.3.1)$$

Similarly, for E_2 , E_3 and E_4 :

$$E_2 = V_1 e^{j\psi_{a2}} + V_2 e^{j\psi_{b2}} + V_3 e^{j\psi_{c2}} + V_4 e^{j\psi_{d2}} \quad (3.3.2)$$

$$E_3 = V_1 e^{j\psi_{a3}} + V_2 e^{j\psi_{b3}} + V_3 e^{j\psi_{c3}} + V_4 e^{j\psi_{d3}} \quad (3.3.3)$$

$$E_4 = V_1 e^{j\psi_{a4}} + V_2 e^{j\psi_{b4}} + V_3 e^{j\psi_{c4}} + V_4 e^{j\psi_{d4}} \quad (3.3.4)$$

Which can be written in terms of progressive phase shifts:

$$E_1 = V_1 + V_2 + V_3 + V_4 \quad (3.3.5)$$

$$E_2 = V_1 e^{j\psi_a} + V_2 e^{j\psi_b} + V_3 e^{j\psi_c} + V_4 e^{j\psi_d} \quad (3.3.6)$$

$$E_3 = V_1 e^{j2\psi_a} + V_2 e^{j2\psi_b} + V_3 e^{j2\psi_c} + V_4 e^{j2\psi_d} \quad (3.3.7)$$

$$E_4 = V_1 e^{j3\psi_a} + V_2 e^{j3\psi_b} + V_3 e^{j3\psi_c} + V_4 e^{j3\psi_d} \quad (3.3.8)$$

⋮

$$E_{n+1} = V_1 e^{jn\psi_a} + V_2 e^{jn\psi_b} + V_3 e^{jn\psi_c} + V_4 e^{jn\psi_d} \quad (3.3.9)$$

$$= V_1 e^{jn\psi_a} + V_2 e^{jn(\psi_a - \frac{\pi}{2})} + V_3 e^{jn(\psi_a - \pi)} + V_4 e^{jn(\psi_a - \frac{3\pi}{2})} \quad (3.3.10)$$

A value must be chosen for ψ_a . This can be chosen for a desired beam angle of θ_a . A value of $\psi_a = \frac{3\pi}{4}$ will be chosen, this will distribute the beams evenly around 0° .

$$E_{n+1} = V_1 e^{jn\frac{3\pi}{4}} + V_2 e^{jn\frac{\pi}{4}} + V_3 e^{-jn\frac{\pi}{4}} + V_4 e^{-jn\frac{3\pi}{4}} \quad (3.3.11)$$

$$(3.3.12)$$

Replace $\frac{\pi}{4}$ with the variable ω , which has no relation to frequency:

$$E_{n+1} = V_1 e^{j3n\omega} + V_2 e^{jn\omega} + V_3 e^{-jn\omega} + V_4 e^{-j3n\omega} \quad (3.3.13)$$

From Fourier transform tables:

$$\mathcal{F}[\delta(t)] = 1 \quad (3.3.14)$$

$$\mathcal{F}[f(t - t_0)] = F(\omega) e^{-j\omega t_0} \quad (3.3.15)$$

The terms in equation 3.3.13 can be written in a form that is similar to the right-hand side of equation 3.3.15. A function $f(x)$ can easily be constructed using equation 3.3.14 and equation 3.3.15, of which the Fourier transform would be:

$$\mathcal{F}[f(x)] = F(n\omega) = E_{n+1} \quad (3.3.16)$$

$$f(x) = V_1\delta(x+3) + V_2\delta(x+1) + V_3\delta(x-1) + V_4\delta(x-3) \quad (3.3.17)$$

$F(n\omega)$ is actually a continuous function over $n\omega$, but since $\omega = \frac{\pi}{4}$ and n a discrete index, the only values of interest will be $n\omega = 0$, $n\omega = \frac{\pi}{4}$, $n\omega = \frac{\pi}{2}$ and $n\omega = \frac{3\pi}{4}$. $F(n\omega)$ is calculated as an example, with the following values, and plotted in figures 3.4a and 3.4b.

- $V_1 = 1$
- $V_2 = 1.5$
- $V_3 = 2$
- $V_4 = 0.5$

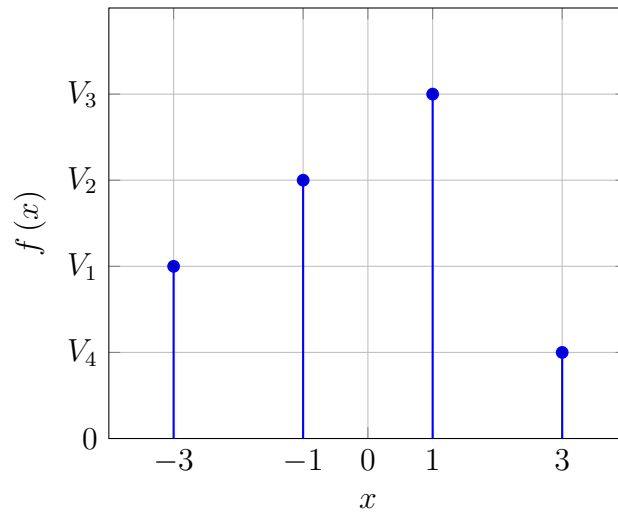
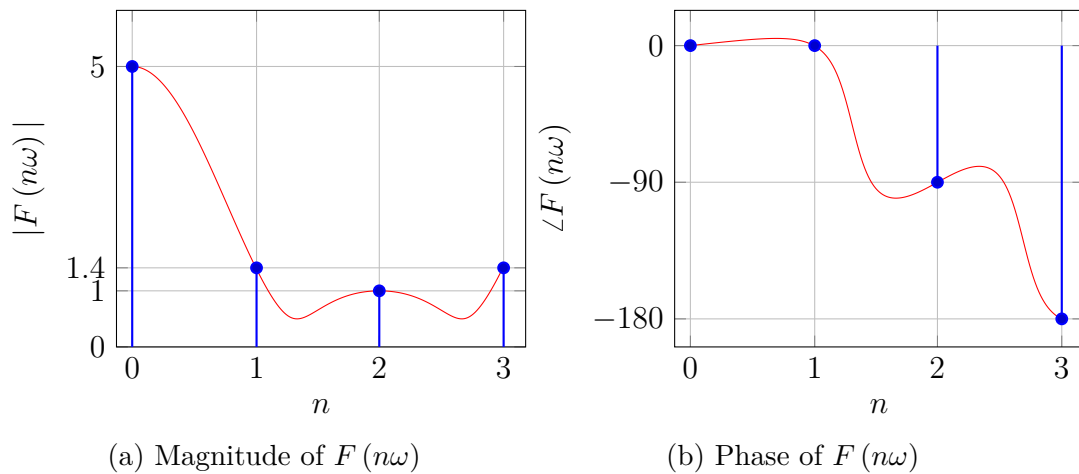


Figure 3.3: Excitation amplitudes as $f(x)$

The values from $F(n\omega)$ represent actual excitations, and can be used as excitation coefficients to plot an array factor. It should be noted that the array factor is highly dependent on the spacing between the array elements. It does not, however, effect the orthogonality. A couple of examples will be shown.

The excitation magnitudes from figure 3.3 are used to demonstrate the example. The array setup is similar to that in figure 2.8, with 4 isotropic

Figure 3.4: Magnitude and phase of $\mathcal{F}[f(x)]$

elements placed along the x -axis. The spacing is $d = \frac{\lambda}{2}$. Figure 3.5 shows the individual beams (only one excitation applied at a time), equal excitations are used. Figure 3.6 shows the same but with different excitations, along with the combined beam (all excitations simultaneously).

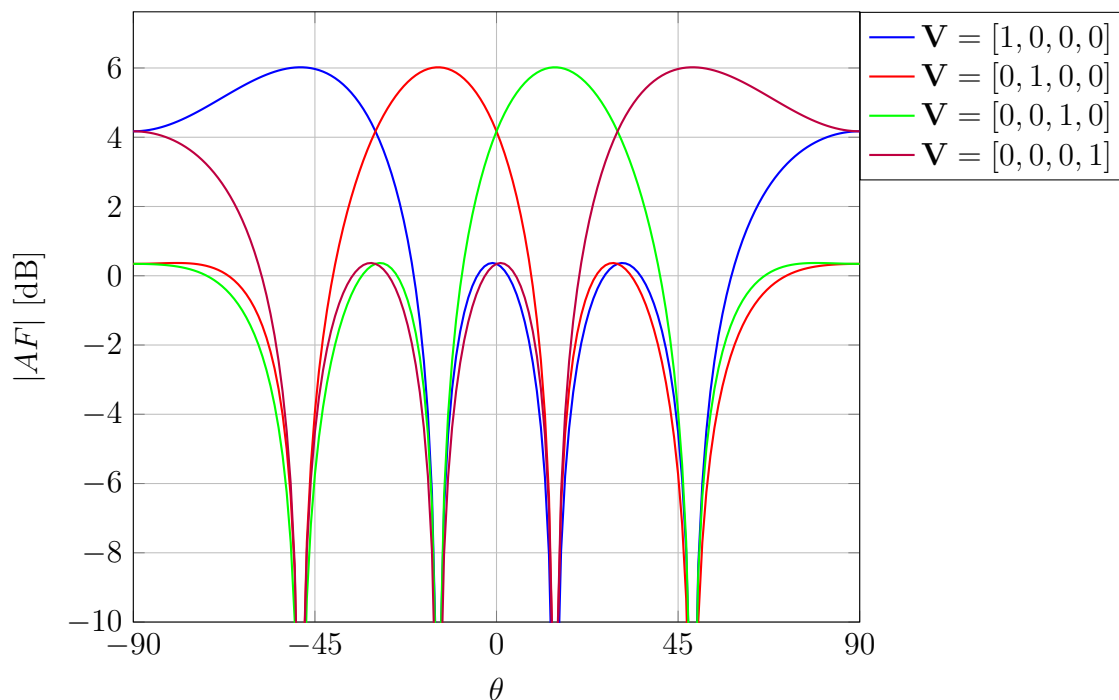
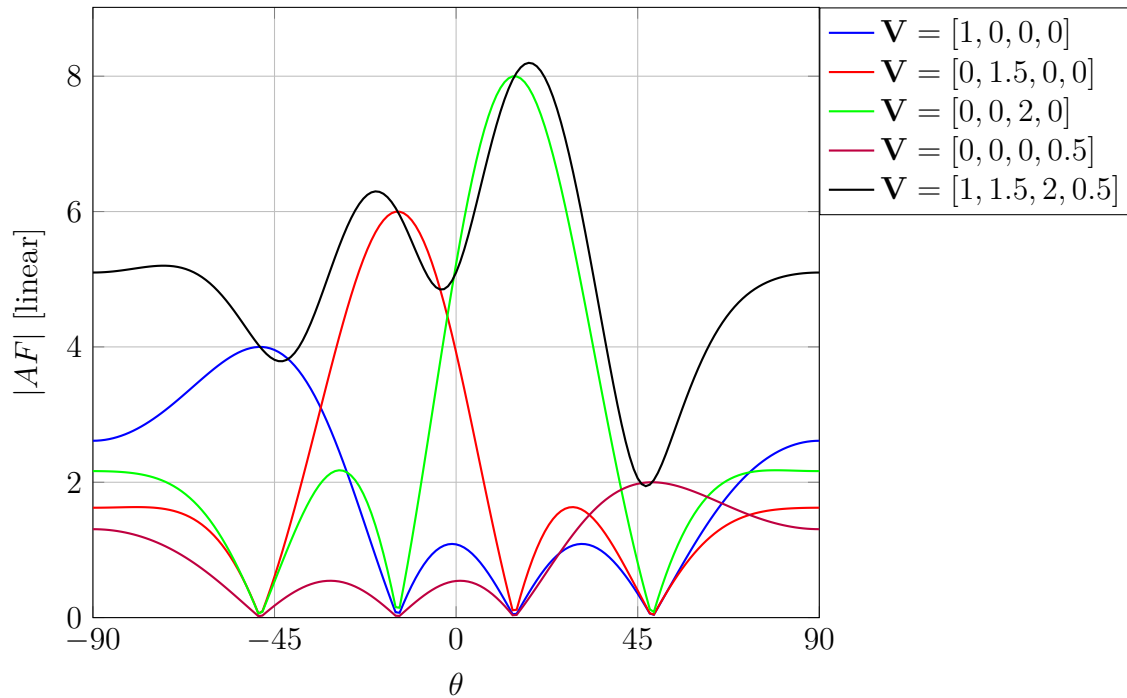
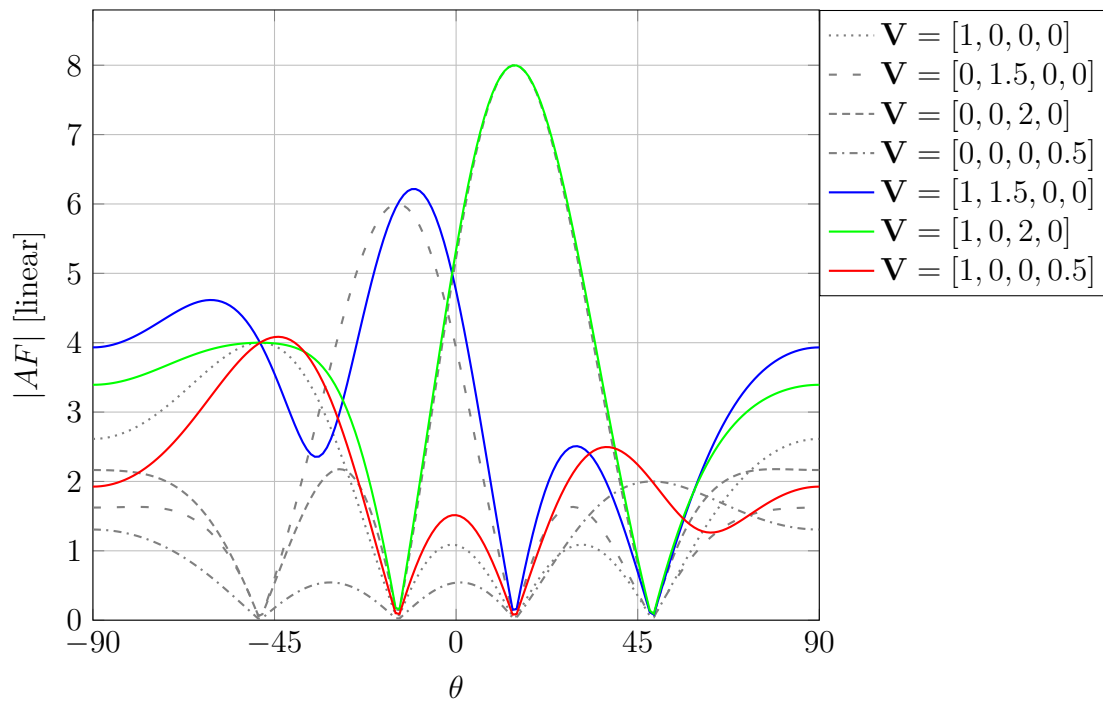
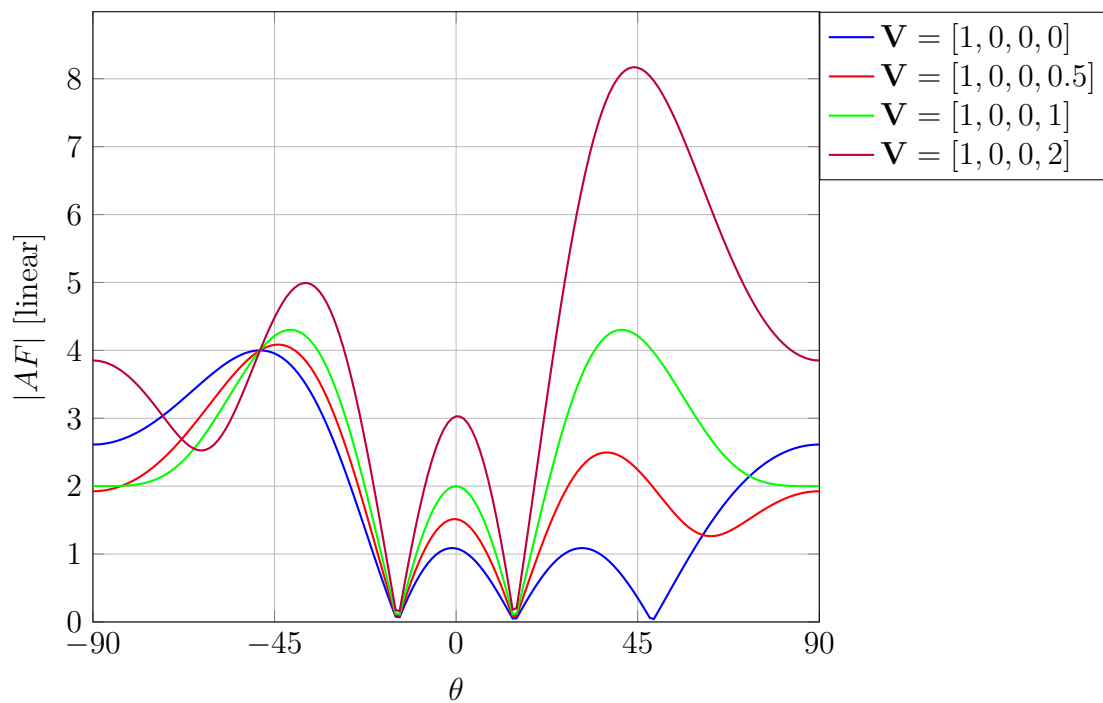
Figure 3.5: $|AF|$ - Single beams

Figure 3.7 shows certain pairs of excitations. This displays how the different beams combine, and gives an indication that sidelobes and nulls have a big effect on the resulting beam. Finally figure 3.8 shows 2 beams, but for varying

Figure 3.6: $|AF|$ - Single port excitations

amplitude of one of the beams. This confirms that the power on one port can be varied, which results in power in the associated beam varying, without it affecting the beam associated with another beam port.

It can be concluded that an orthogonal multiple beam BFN like the one discussed in this section computes the Fourier Transform of the beam excitation, and delivers the output on the antenna element ports. The Butler Matrix is efficient implementation of an orthogonal BFN (the Fourier Transform), which is similar to a Fast Fourier Transform. (Bhattacharyya, 2006)

Figure 3.7: $|AF|$ - Different beam pairsFigure 3.8: $|AF|$ - Increasing excitation on 1 beam

Chapter 4

Implementation of the Butler Matrix

This chapter will discuss how the Butler Matrix can be implemented, and 2 different implementations will be proposed, followed up by simulations and practical implementations. These 2 implementations differ in both frequency of operation and components.

4.1 Ideal Implementation

The Butler Matrix can be implemented using quadrature hybrids and phase shifts to apply the necessary power division/combination and multiplication. To illustrate a completely ideal implementation, a model was built in AWR Microwave Office using phase specified transmission lines. This is the perfect way to start off a design as it can confirm the core theory.

The model is based on the “Hybrid Matrix” derived by Bhattacharyya (2006) using the FFT algorithm to implement equation 3.3.16, and on a similar implementation done by Adamidis *et al.* (2019). Shown in figure 4.1, it comprises of 4 interconnected hybrid couplers, with 2 45° phase shifts applied using transmission lines.

This model is of course not practical, and the reasons will be discussed in section 4.2. The results related to this model are discussed in section 5.1.

4.2 Practical considerations

The biggest concern with implementing the Butler Matrix is the two lines that cross, shown in figure 4.2 and labelled b and c . Assuming that the implementation will be on a single layer microstrip transmission line, there is no way that two lines can cross without breaking the ground plane by routing one of the lines on the bottom of the substrate. The only option is then to break the ground plane in some way, but to keep the disturbance to a minimum,

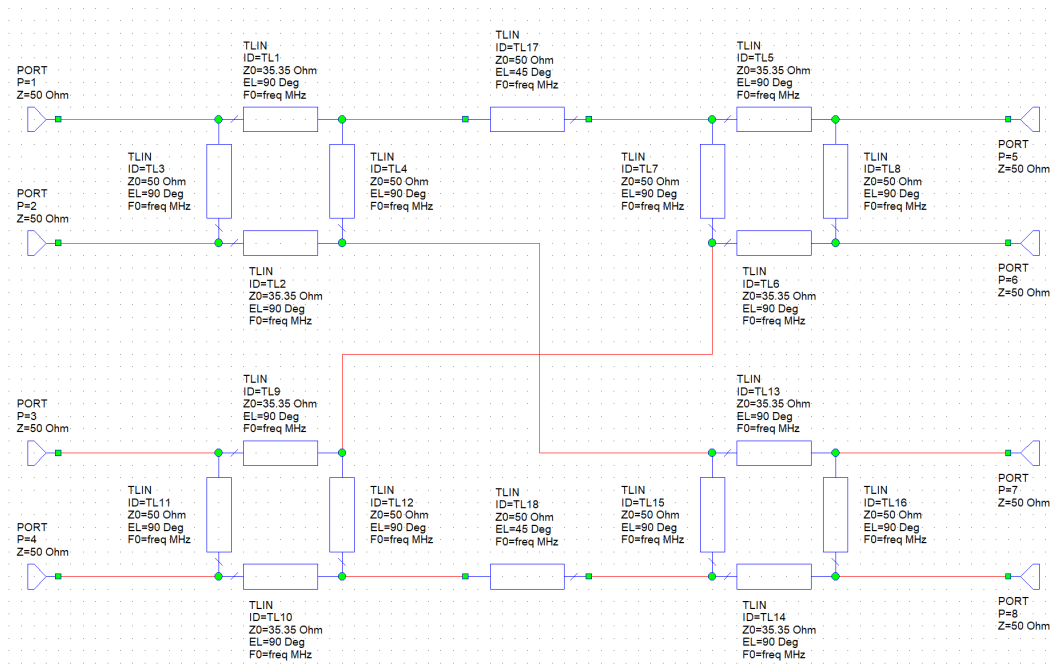


Figure 4.1: AWR circuit of ideal circuit

or have some compensation to restore the line impedance. With two lines crossing, they will be in close proximity to each other, thus there is a risk of coupling. However, if the lines cross perpendicularly, the coupling will be kept to a minimum.

The second concern is that the line labelled b in figure 4.2 has zero length, which is not realisable. When b is replaced with a finite length line, it will be physically longer than line a because of the placement of the hybrids, as long as a is a straight line. To realise the 45° phase difference, a must be meandered that it is 45° electrically longer than b .

4.3 Microstrip Implementation at 1.5 GHz

The Butler Matrix can be implemented on a microstrip interface, which will be the preferred interface for this piece of work due to its ease of manufacturing and reduced cost. The first implementation will be designed to operate at 1.5 GHz. Most of the components used in this implementation, like the hybrid couplers, rely on transmission-line lengths. This means its size scales inversely with frequency, making it impractically large for lower frequencies (< 750 MHz) and small for higher frequencies (> 20 GHz).

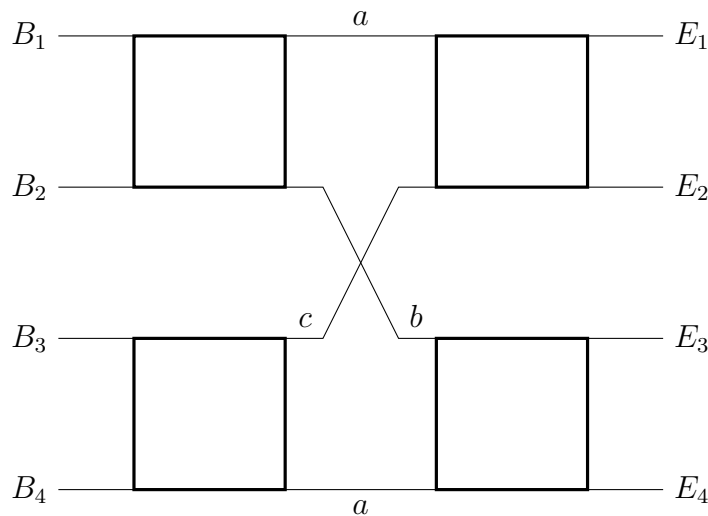


Figure 4.2: Butler Matrix - Indicating non-zero and crossing lines

Frequency	1.5 GHz
Z_0	50Ω
$\frac{Z_0}{\sqrt{2}}$	35.36Ω
ϵ_r	3.5
Board thickness	0.508 mm
Line width (50Ω)	1.075 mm
Line width (35.36Ω)	1.834 mm
Quarter wavelength (50Ω)	30.18 mm
Quarter wavelength (35.36Ω)	28.717 mm

Table 4.1: Microstrip Implementation at 1.5 GHz - Design parameters

4.3.1 Simulation

A real implementation of Butler Matrix will have to overcome the shortcomings of the ideal implementation mentioned in section 4.2. The first step to start a microstrip implementation is to define the various parameters for microstrip lines.

Table 4.1 lists the required line widths and lengths associated with the operating frequency on the specified substrate for a characteristic impedance of 50Ω . A characteristic impedance of 35.36Ω is also required for the hybrid coupler.

Referring to figure 4.2, to overcome the issue of the crossing lines, line b is cut about half of a 50Ω -line width on both sides of line c . This allows just enough space for an 0805 resistor to be soldered across line c . The resistor only has conductive material on its ends, making it possible to mount it on

top of line c without risk of having electrical contact with line c . A 0Ω resistor is used. Figure 4.3a shows the crossing.

The length of line c (and consequently b), is chosen so that there is the same length of separation between B_2 and B_3 than between B_1 and B_2 , as can be seen in figure 4.2. Line b and c cross with a 45° angle meaning that the separation between B_2 and B_3 will directly influence the length of a . Extra line length is added horizontally to create more separation between the hybrids on the left side and on the right side, to create enough space for a meander.

The total length of a including the meander, is set to the electrical length of c plus 45° . The resulting circuit is shown in figure 4.3b.

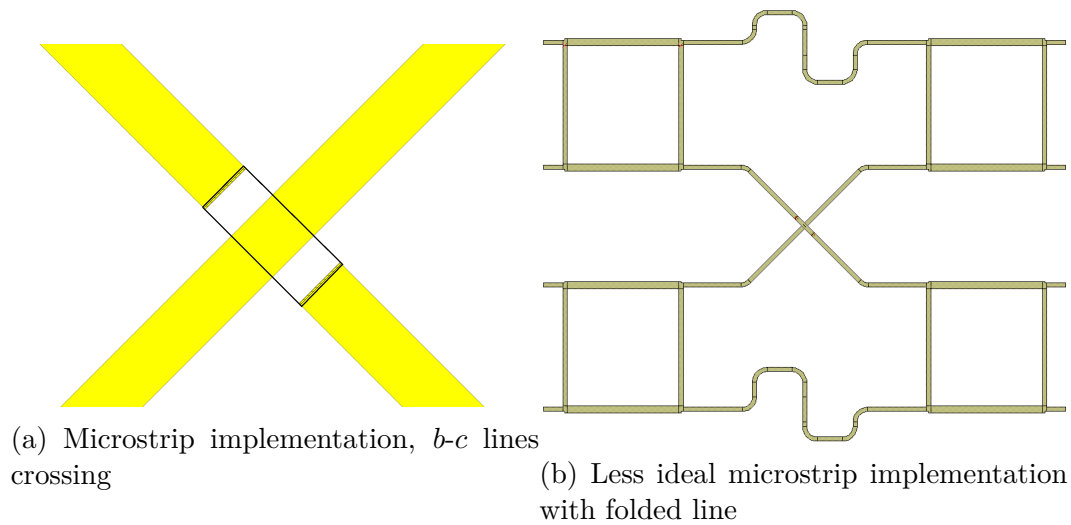


Figure 4.3

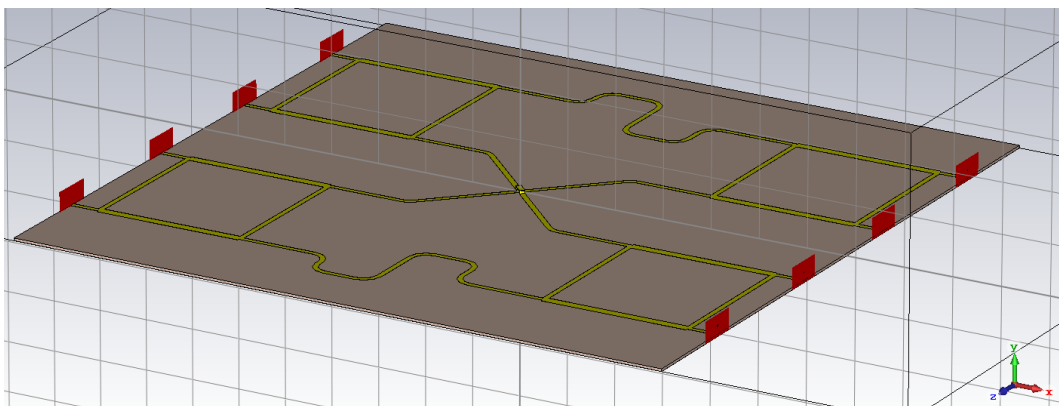


Figure 4.4: 3D Model of Butler Matrix in CST

	Measured ports	50 Ω Terminated ports
Setup 1	1, 2, 3, 4	5, 6, 7, 8
Setup 2	1, 2, 5, 6	3, 4, 7, 8
Setup 3	1, 2, 7, 8	3, 4, 5, 6
Setup 4	3, 4, 5, 6	1, 2, 7, 8
Setup 5	3, 4, 7, 8	1, 2, 5, 6
Setup 6	5, 6, 7, 8	1, 2, 3, 4

Table 4.2: Microstrip Implementation - Measurement setup

AWR uses closed-form methods to solve these circuits, and doesn't perform a full-wave simulation. This is not as accurate as is required, especially in the case with the crossing lines. To accurately simulate this, a full-wave simulation is required. This layout was built in CST Studio, and a full wave simulation of this network was performed, using the frequency domain solver. Figure 4.4 shows the 3D model in CST Studio, having the same dimensions as the model in AWR, but more accurately modelling the fringing fields of the 0 Ω resistor in the crossover. The 0 Ω resistor is modelled with a strip of copper suspended in air over the line that it crosses. The width, length and thickness of the strip are the same as the conductive strip on the resistor.

The results of these two simulations will be discussed in section 5.2.

4.3.2 Physical Implementation

As indicated by the discussion in section 5.2, the results of the simulation were adequate to motivate a physical implementation. The first step is to use the same dimensions and properties defined in the simulation to manufacture a physical *printed circuit board* (PCB). There already exists a complete 3D-model that was constructed for full wave simulation, which was exported from CST and manufactured. The manufactured PCB was finalised by soldering the 0 Ω resistor and SMA connectors onto the board.

The network was then measured on a 4-port network analyser, but since the network in question is an 8-port network, a set of 6 measurements had to be done and recombined to construct the complete 8×8 matrix of scattering parameters. Table 4.2 lists the different ports that are measured with each setup. The ports not being measured during a specific setup are terminated with a 50 Ω SMA load.

The results will be discussed in section 5.2.2.

4.3.3 Antenna Integration

The results in section 5.2.2 seems to confirm that the microstrip circuit provides all the necessary parameters:

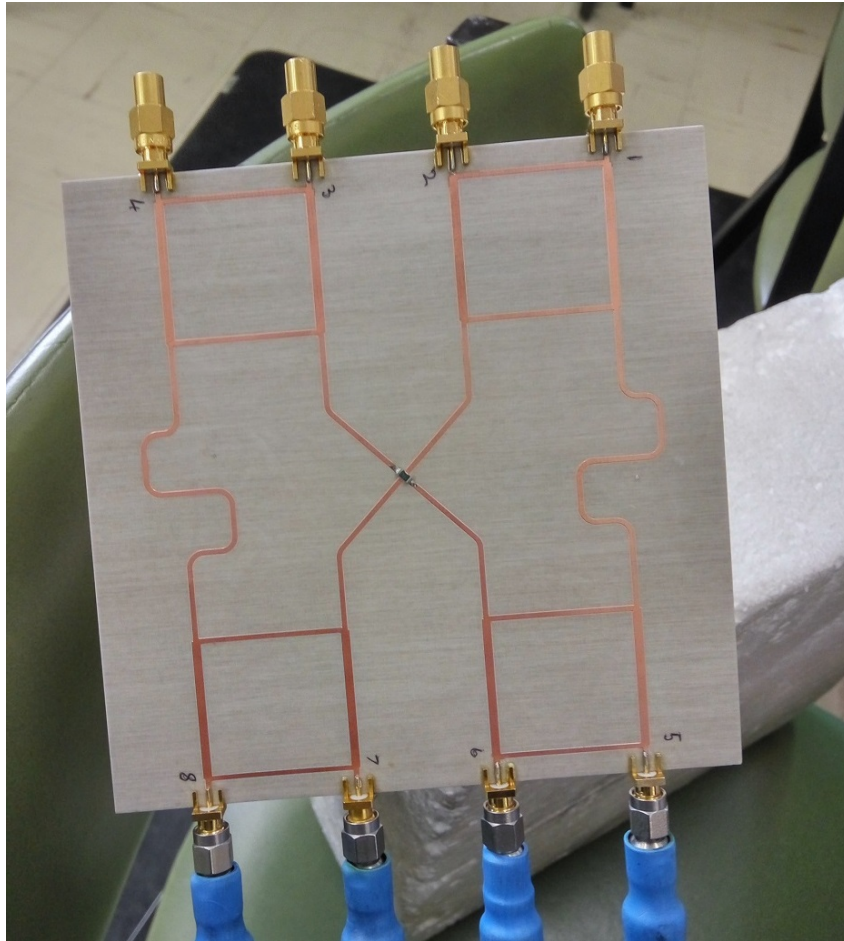


Figure 4.5: Microstrip implementation - measurement setup

- Good match (return loss)
- Isolation between beam ports
- Isolation between element ports
- Transmission magnitude
- Transmission phases/Progressive phase shifts

This gives confidence that the Butler Matrix (In this implementation) has the multiple beam beamforming capabilities as discussed in Chapter 3. To confirm this hypothesis, a pin-fed microstrip patch antenna array was designed, consisting of 4 elements. As the design of the antenna is not the topic of this thesis, only a brief explanation of the design will be given.

The design process of a transmission-line model rectangular patch, as outlined by (Balanis, 2012), was followed. The first step is to calculate the effective dielectric constant, ϵ_{eff} of the substrate, using equation 4.3.1:

$L = a$	52.8 mm
$W = b$	67.7 mm
$d = \frac{\lambda}{2}$	99.9 mm
c	16.5 mm

Table 4.3: Microstrip antenna array dimensions

$$\frac{W}{h} > 1$$

$$\epsilon_{eff} = \frac{\epsilon_r + 1}{2} + \frac{\epsilon_r - 1}{2} \left[1 + 12 \frac{h}{W} \right]^{-\frac{1}{2}} \quad (4.3.1)$$

The next step is to calculate the effective length, $L_{eff} = L + 2\Delta L$, which is a result of fringing fields. For this application, L_{eff} is $\frac{\lambda}{2}$. ΔL is a function of ϵ_{eff} and $\frac{W}{h}$ and can be approximated with equation 4.3.2:

$$\frac{\Delta L}{h} = 0.412 \frac{(\epsilon_{eff} + 0.3) \left(\frac{W}{h} + 0.264 \right)}{(\epsilon_{eff} - 0.258) \left(\frac{W}{h} + 0.8 \right)} \quad (4.3.2)$$

Finally the width W of the patch is calculated using equation 4.3.3.

$$W = \frac{c_0}{2f_r} \sqrt{\frac{2}{\epsilon_r + 1}} \quad (4.3.3)$$

The parameters used in these equations are:

- W – Width of the patch
- L – Length of the patch
- h – Substrate height
- f_r – Resonant frequency
- c_0 – Speed of light
- ϵ_r – Dielectric constant

This Butler Matrix was designed to operate at 1.5 GHz, thus $f_r = 1.5$ GHz. The substrate chosen was Rogers 4003C, $h = 1.524$ mm, $\epsilon_r = 3.5$. Figure 4.6 shows the configuration of the array, along with the required dimensions listed in table 4.3. The dimensions of the substrate on which the patches are located is $2b \times 9a$.

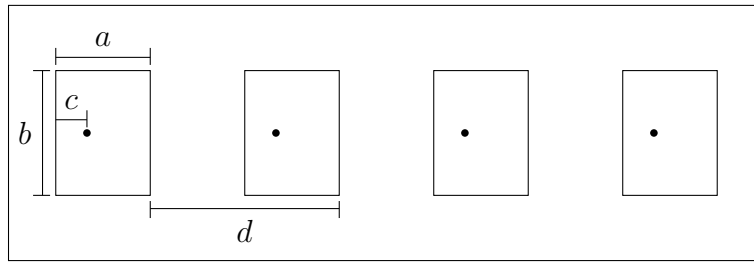
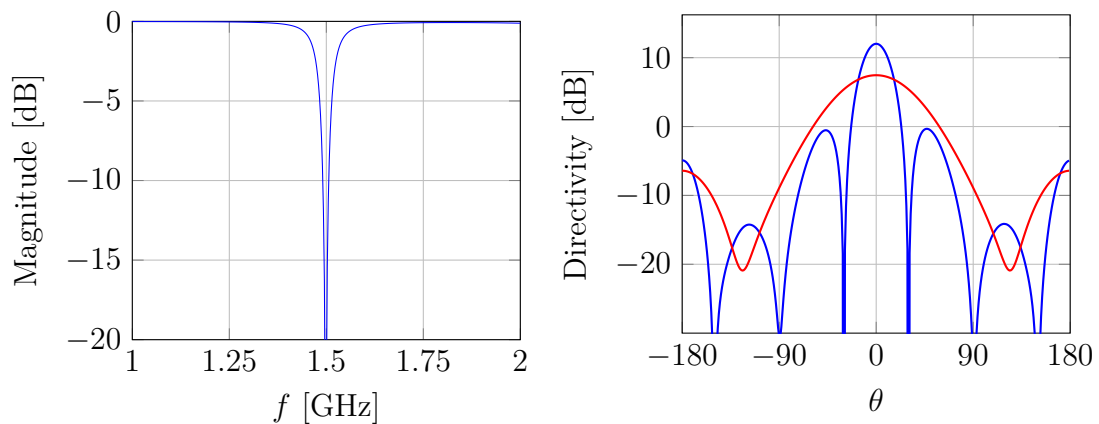


Figure 4.6: Microstrip antenna array dimensions

A model of a single patch was built in CST. Each patch is pin fed, and the location where the pin is located (Distance c from the W -edge) greatly influences the input impedance of the antenna. The input impedance is required to be around $50\ \Omega$. The distance c was determined by optimisation in CST to achieve the lowest return loss at 1.5 GHz. The resulting return loss (s_{11}) is shown in figure 4.7a. The match is good at 1.5 GHz, but falls off quickly, this is expected as patch antennas are known to be narrow-band. The directivity is shown in figure 4.7b, where the red line represents a single patch, and the blue line represents the 4-element array.



(a) Microstrip patch CST simulation - Reflection

(b) Microstrip patch CST simulation - Directivity

Figure 4.7

Following these results, the antenna was manufactured. The findings in table 5.20 suggest that the element ports need to be connected to the antenna array in a different order. Figure 4.8 shows the order in which the individual patches were connected to the element ports on the Butler Matrix during the measurement. The antenna was mounted in the anechoic chamber in the antenna lab at Stellenbosch University, as shown in figure 4.9. The measured results are discussed in section 5.2.3.

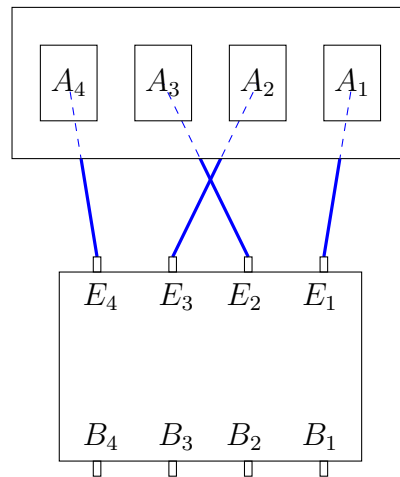


Figure 4.8: Interconnection between microstrip patch and Butler Matrix

4.4 Microstrip Implementation at 15 GHz

Although the implementation in section 4.3 worked very well, there are some points that need investigation, leading to this implementation at 15 GHz:

- Decrease the total size due to shorter wavelength
- Yield a much larger bandwidth
- Showcase an alternative to the $0\ \Omega$ resistor crossing method
- Prove the Butler Matrix can work for Ku-band applications

The first issue with this implementation is the $0\ \Omega$ resistor. The wavelength is only a tenth of what it was for the 1.5 GHz version, meaning that small disturbance in path length now has a much bigger effect. Traii (2008) suggests cascading two hybrid couplers to synthesise a crossover. Figure 4.10 shows an example of such a crossover, with Q_1 and Q_2 denoting the couplers. P_1 and P_2 denotes the signal passing in each transmission line between the couplers. Pozar (2011) analyses the hybrid coupler, and the outputs can be written as:

$$P_1 = \frac{-jA_1 - A_2}{\sqrt{2}}$$

$$P_2 = \frac{-A_1 - jA_2}{\sqrt{2}}$$

$$B_1 = jA_2$$

$$B_2 = jA_1$$

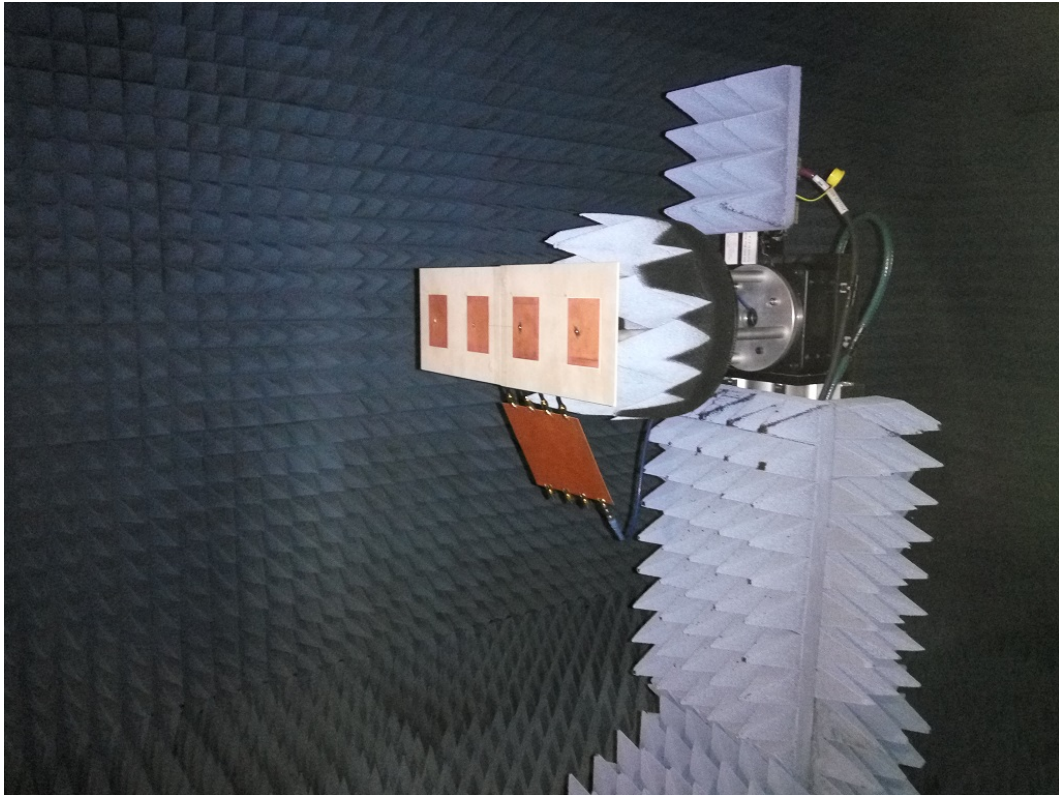


Figure 4.9: Microstrip patch array, mounted in anechoic chamber

The only issue with this implementation of a crossover is that its bandwidth is now limited because a hybrid coupler is bandwidth limited. However, the Butler Matrix already consists of 4 hybrids, meaning the bandwidth is already limited.

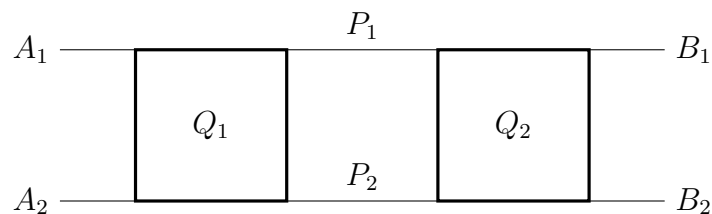


Figure 4.10: Crossover, utilising 2 quadrature hybrids

4.4.1 Simulation

An ideal version (using phase specified transmission lines) of this implementation was simulated in AWR, the circuit is shown in figure 4.11. The results

Frequency	15 GHz
Z_0	50Ω
$\frac{Z_0}{\sqrt{2}}$	35.36Ω
ϵ_r	3.5
Board thickness	0.203 mm
Line width (50Ω)	0.43 mm
Line width (35.36Ω)	0.72 mm
Quarter wavelength (50Ω)	2.9 mm
Quarter wavelength (35.36Ω)	2.58 mm

Table 4.4: Microstrip Implementation at 15 GHz - Design parameters

can be found in section B.4 and since it is almost identical to the results in section 5.1, it won't be discussed here.

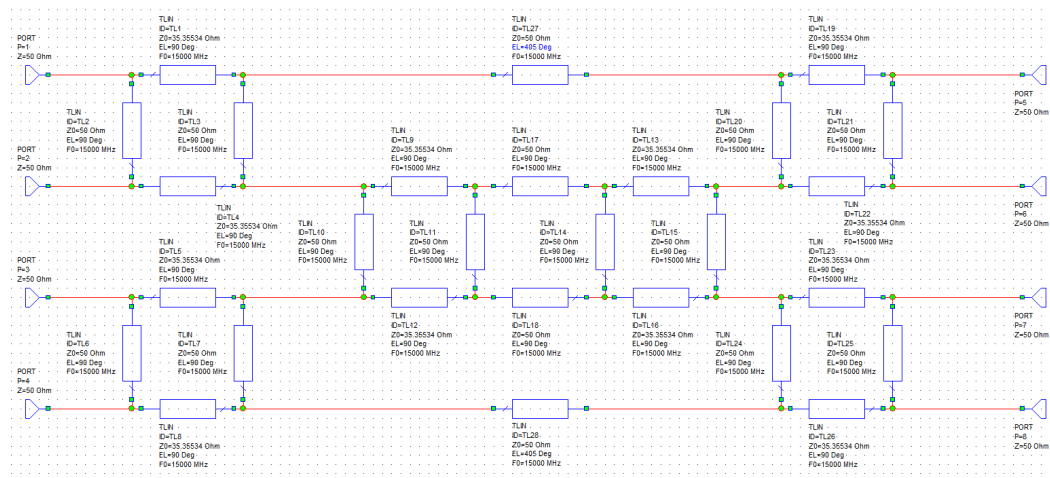


Figure 4.11: Ideal AWR model, with hybrid crossover

A 3D model, similar to the one discussed in section 4.3.1 was constructed and simulated using the frequency domain solver. There are only a couple of differences. The obvious one is that it is much smaller. This can immediately be observed from the design parameters listed in table 4.4. The quarter wavelength is not much longer than the track width, for this reason a thinner substrate was chosen to keep the line width much narrower than the quarter wavelength.

The 0Ω resistor crossover was replaced with the quadrature hybrid crossover. The meander was also changed slightly to accommodate for the required phase shift. The last change that was implemented is the feed lines. The physical size of the Butler Matrix section was too small and there was not enough space

to fit connectors, hence the feed lines were added. They are all electrically the same length. Figure 4.13 shows the 3D model.

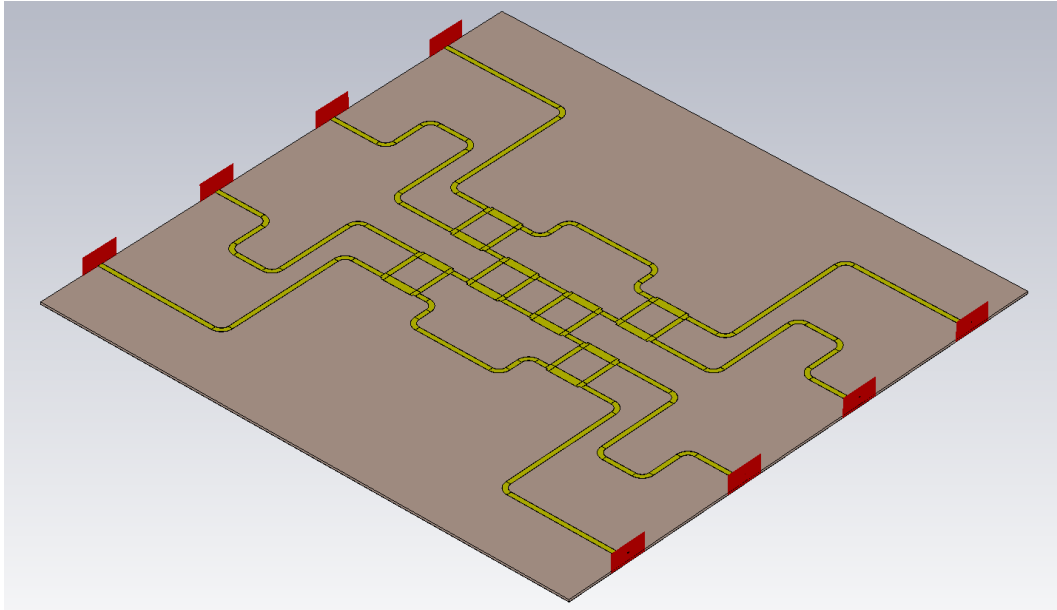


Figure 4.12: CST model, with hybrid crossover, feed lines

The simulation results are summarised and discussed in section 5.3.1. Much higher losses were seen compared to other implementations. This can be attributed to much longer path lengths due to the feed lines and thinner lines because a thinner substrate was used, resulting in higher conduction losses. Despite the higher losses, and greater phase length error, the average progressive phase shift was still close to the ideal. The circuit was manufactured, and will be discussed in section 4.4.2.

4.4.2 Physical Implementation

The circuit discussed in section 4.4.1 was manufactured. The manufactured circuit can be seen in figure 4.13. An attempt was made to add a TRL (Thru-reflect-line) calibration kit to the PCB, with the line lengths identical to the feed lines. The purpose of the TRL circuit was to calibrate out the losses and path lengths of the feed lines. However, the TRL circuit wasn't designed correctly and was thus not used during the measurement of this circuit. The results are discussed in section 5.3.2.

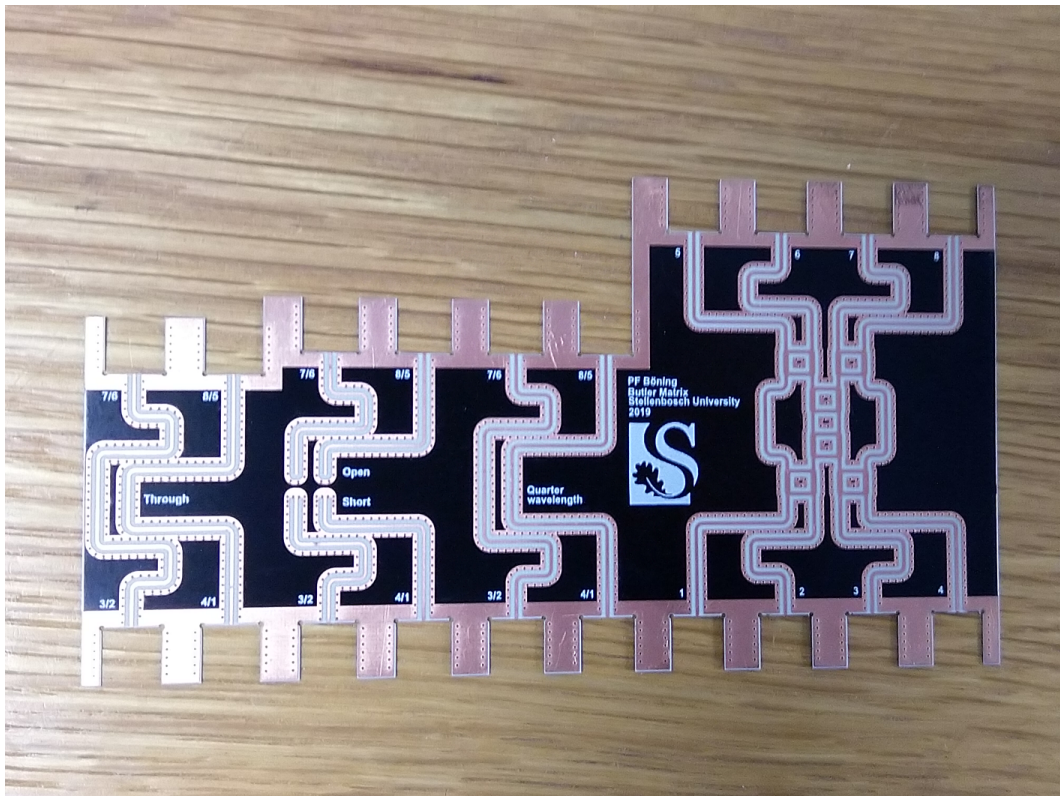


Figure 4.13: Manufactured PCB, with TRL calibration

Chapter 5

Results

This chapter discusses the results obtained from the various simulations and practical measurements discussed in Chapter 4. Conclusions are also discussed regarding the results and the overall performance of the underlying circuits.

5.1 Ideal Implementation

Even though this is an ideal implementation that will have a perfect match to 50Ω , it is still dependent on line lengths, so it will only have a good match over a finite frequency range. For the purposes of bandwidth analysis in this section, an operating bandwidth of 10% will be assumed, centred around the centre frequency, 1.5 GHz. All of the scattering parameters are graphed in Appendix B, but a reference will be made to a specific graph when the relevant performance parameter is being discussed.

Table 5.1 summarises the input reflection on all the ports, as well as the beam port and element port isolation. The worst cases at the centre, as well as the upper and lower edges of the frequency band are listed. Figure B.1 shows the input reflection. Figure B.2 shows the beam port and element port isolation.

Frequency	Reflection	Beam isolation	Element isolation
$f_L = 1425 \text{ MHz}$	-17.59 dB	-16.05 dB	-16.05 dB
$f_C = 1500 \text{ MHz}$	< -50 dB	< -50 dB	< -50 dB
$f_H = 1575 \text{ MHz}$	-15.88 dB	-17.31 dB	-17.31 dB

Table 5.1: AWR Ideal simulation - Reflection and Isolation

Figure B.3 shows the path loss and Figure B.4 shows the path length in terms of phase. Table 5.2 summarises the path between beam port 1 and element ports 1 to 4. The s -parameters that relate to these paths are s_{51} , s_{61} , s_{71} , and s_{81} . The summarised phase lengths are not the actual lengths but

rather the relative length, with s_{51} being the reference. The relative lengths are important to know because they are equivalent to the progressive phase shifts from equation 3.2.10.

The path loss in this ideal implementation is not really relevant as it only explains the power splitter, and doesn't take into account actual copper and dielectric loss. Only $\frac{1}{4}$ of the power going into the beam port reaches each element port, which is trivial.

Frequency	Transmission mag. [dB]	s_{51} (ref) [°]	s_{61} [°]	s_{71} [°]	s_{81} [°]
$f_L = 1425$ MHz	-6.57 dB	0	-89	-47.4	-137.4
$f_C = 1500$ MHz	-6.02 dB	0	-90	-45	-135
$f_H = 1575$ MHz	-6.52 dB	0	-91.1	-44.4	-134.6

Table 5.2: AWR Ideal simulation - Transmission phase, beam port 1

Figure B.5 shows the path length in terms of phase. Table 5.3 summarises the path between beam port 2 and element ports 1 to 4. The s -parameters that relate to these paths are s_{52} , s_{62} , s_{72} , and s_{82} . The summarised phase lengths are not the actual lengths but rather the relative length, with s_{52} being the reference.

Frequency	Transmission mag. [dB]	s_{52} (ref) [°]	s_{62} [°]	s_{72} [°]	s_{82} [°]
$f_L = 1425$ MHz	-6.52 dB	0	-90	133.1	41.5
$f_C = 1500$ MHz	-6.02 dB	0	-90	135	45
$f_H = 1575$ MHz	-6.3 dB	0	-90.1	138.6	46.7

Table 5.3: AWR Ideal simulation - Transmission phase, beam port 2

Figure B.6 shows the path length in terms of phase. Table 5.4 summarises the path between beam port 3 and element ports 1 to 4. The s -parameters that relate to these paths are s_{53} , s_{63} , s_{73} , and s_{83} . The summarised phase lengths are not the actual lengths but rather the relative length, with s_{53} being the reference.

Frequency	Transmission mag. [dB]	s_{53} (ref) [°]	s_{63} [°]	s_{73} [°]	s_{83} [°]
$f_L = 1425$ MHz	-6.52 dB	0	91.6	-131.5	-41.5
$f_C = 1500$ MHz	-6.02 dB	0	90	-135	-45
$f_H = 1575$ MHz	-6.3 dB	0	91.9	-136.8	-46.7

Table 5.4: AWR Ideal simulation - Transmission phase, beam port 3

Figure B.7 shows the path length in terms of phase. Table 5.5 summarises the path between beam port 4 and element ports 1 to 4. The s -parameters that relate to these paths are s_{54} , s_{64} , s_{74} , and s_{84} . The summarised phase

lengths are not the actual lengths but rather the relative length, with s_{54} being the reference.

Frequency	Transmission mag. [dB]	s_{54} (ref) [°]	s_{64} [°]	s_{74} [°]	s_{84} [°]
$f_L = 1425$ MHz	-6.57 dB	0	90	48.5	137.4
$f_C = 1500$ MHz	-6.02 dB	0	90	45	135
$f_H = 1575$ MHz	-6.52 dB	0	90.3	43.6	134.6

Table 5.5: AWR Ideal simulation - Transmission phase, beam port 4

Table 5.6 summarises the progressive phase shifts measured within this circuit. In order for the progressive phase shifts to be consistent, the columns containing element ports 2 and 3 must be swapped. If beam port 1 was associated with progressive phase shift ψ_a from Table 3.2.26, then ψ_b would be associated with beam port 3, ψ_c with beam port 2 and ψ_d with beam port 4. This is the reason why the rows for beam ports 2 and 3 are also swapped.

	Element port				ψ
Beam port	1	3	2	4	
1	0	-45	-90	-135	$\psi_a = -45$
3	0	-135	90	-45	$\psi_b = -135$
2	0	135	-90	45	$\psi_c = 135$
4	0	45	90	135	$\psi_d = 45$

Table 5.6: AWR Ideal simulation - Progressive phase shift

5.2 Microstrip Implementation at 1.5 GHz

The results of the ideal implementation of the Butler Matrix was discussed in section 5.1. This section follows up with the results of an implementation on microstrip, operating at 1.5 GHz. Firstly two simulations of the implementations on microstrip will be analysed and compared to the ideal case, then the physical measurements will be discussed.

5.2.1 Simulated

Two versions of this implementation was simulated and is discussed in section 4.3.1. The first simulation utilises microstrip, dimension-based transmission line models in AWR Microwave Office. The second simulation is a full wave simulation of a 3D model, built in CST Studio, using the same dimensions as with the AWR simulation. The results of these two simulations are discussed in this section. Similar to section 5.1, an operating bandwidth of 10% will be

assumed, centred around 1.5 GHz, and all the s -parameters are graphed in Appendix B.

Tables 5.7, and 5.8 summarises the input reflection on all the ports, as well as the beam port and element port isolation. Figure B.8 shows the input reflection. Figures B.9 and B.10 show the beam port and element port isolation.

The circuit is well matched and comparable to the ideal simulation. The full wave simulation follows the closed-form solution very closely. This is a good indication that the lengths and widths of the lines are calculated correctly. The isolation tells the same story, and is comparable with the ideal simulation.

Frequency [MHz]	Reflection	
	AWR	CST
$f_L = 1425$ MHz	-16.31 dB	-14.46 dB
$f_C = 1500$ MHz	< -50 dB	-26.57 dB
$f_H = 1575$ MHz	-18.98 dB	-19.53 dB

Table 5.7: Microstrip CST and AWR simulation - Reflection

Frequency [MHz]	Beam isolation		Element isolation	
	AWR	CST	AWR	CST
$f_L = 1425$ MHz	-19.16 dB	-18.59 dB	-19.41 dB	-16.8 dB
$f_C = 1500$ MHz	< -50 dB	-30.16 dB	< -50 dB	-29.92 dB
$f_H = 1575$ MHz	-21.29 dB	-25.34 dB	-21.29 dB	-23.72 dB

Table 5.8: Microstrip CST and AWR simulation - Isolation

Figure B.11 shows the path loss and Figure B.12 shows the path length in terms of phase. Table 5.2 summarises the path between beam port 1 and element ports 1 to 4.

The path loss in this implementation starts to become relevant as it takes into account actual copper and dielectric loss. $\frac{1}{4}$ (≈ -6 dB) of the power going into the beam port reaches each element port, the rest is attributed to losses. The phase length of the AWR simulation differs from the ideal by up to 1° , and similarly for the CST simulation. The CST results are omitted from these tables, as the results are similar to those of the AWR simulation, and it can be found in Appendix B.

Figure B.13 shows the path length in terms of phase. Table 5.3 summarises the path between beam port 2 and element ports 1 to 4.

Figure B.14 shows the path length in terms of phase. Table 5.4 summarises the path between beam port 3 and element ports 1 to 4.

Frequency	Transmission mag. [dB]	s_{51} (ref) [°]	s_{61} [°]	s_{71} [°]	s_{81} [°]
$f_L = 1425$ MHz	-6.7 dB	0	-90.8	-49.3	-139
$f_C = 1500$ MHz	-6.26 dB	0	-90	-46	-136
$f_H = 1575$ MHz	-6.42 dB	0	-91.4	-43.8	-134.2

Table 5.9: Microstrip AWR simulation - Beam port 1 bandwidth

Frequency	Transmission mag. [dB]	s_{52} (ref) [°]	s_{62} [°]	s_{72} [°]	s_{82} [°]
$f_L = 1425$ MHz	-6.47 dB	0	-89.9	-226.9	-318.5
$f_C = 1500$ MHz	-6.27 dB	0	-90	-226	-316
$f_H = 1575$ MHz	-6.42 dB	0	-90.4	-223.6	-312.4

Table 5.10: Microstrip AWR simulation - Beam port 2 bandwidth

Frequency	Transmission mag. [dB]	s_{53} (ref) [°]	s_{63} [°]	s_{73} [°]	s_{83} [°]
$f_L = 1425$ MHz	-6.49 dB	0	91.6	228.2	318.1
$f_C = 1500$ MHz	-6.27 dB	0	90	225.6	315.6
$f_H = 1575$ MHz	-6.42 dB	0	88.7	221.6	312.1

Table 5.11: Microstrip AWR simulation - Beam port 3 bandwidth

Figure B.15 shows the path length in terms of phase. Table 5.5 summarises the path between beam port 4 and element ports 1 to 4.

Frequency	Transmission mag. [dB]	s_{54} (ref) [°]	s_{64} [°]	s_{74} [°]	s_{84} [°]
$f_L = 1425$ MHz	-6.7 dB	0	89.7	47.7	138.6
$f_C = 1500$ MHz	-6.26 dB	0	90	45.6	135.6
$f_H = 1575$ MHz	-6.42 dB	0	90.3	42.3	133.8

Table 5.12: Microstrip AWR simulation - Beam port 4 bandwidth

Tables 5.13 and 5.14 summarise the progressive phase shifts, similar to Table 5.6 and the same column/row swaps are done. The progressive phase shift is not consistent over element ports, thus the average of the phase shifts are taken and the result is what is displayed in the ψ -column.

The CST simulation has a slightly worse progressive phase shift, which can most likely be attributed to the little extra length introduced by the 0Ω resistor.

5.2.2 Measured

This section will discuss the results obtained from measuring the Butler matrix that was built, mentioned in section 4.3.2. Similar to section 5.1, an operating

	Element port				ψ
Beam port	1	3	2	4	
1	0	-46	-90	-136	$\psi_a = -45.33$
3	0	-134.4	90	-44.4	$\psi_b = -134.8$
2	0	134	-90	44	$\psi_c = 134.7$
4	0	45.6	90	135.6	$\psi_d = 45.2$

Table 5.13: Microstrip AWR simulation - Progressive phase shift

	Element port				ψ
Beam port	1	3	2	4	
1	0	-46.5	-88.6	-136.3	$\psi_a = -45.43$
3	0	-133.3	90	-42	$\psi_b = -134$
2	0	132.1	-91.3	42	$\psi_c = 134$
4	0	47.9	89.9	136.4	$\psi_d = 45.47$

Table 5.14: Microstrip CST simulation - Progressive phase shift

bandwidth of 10% will be assumed, centred around 1.5 GHz, and all the s -parameters are graphed in Appendix B.

Table 5.15 summarises the input reflection on all the ports, as well as the beam port and element port isolation. Figure B.16 shows the input reflection. Figures B.17 and B.18 show the beam port and element port isolation.

This is where real world effects start to become visible. Figure B.16 clearly shows that the resonant part of the circuit, or the frequency point for which it is supposed to be perfectly matched, is not on the design frequency of 1.5 GHz. It is shifted slightly to the left, likely an indicator that the wavelength used in the design is very slightly too long. The match is still quite good, especially at 1.5 GHz, but the circuit still achieves a match of < -12 dB over the entire operating band. The isolation is good, very similar to the AWR and CST simulations.

Frequency	Reflection	Beam isolation	Element isolation
$f_L = 1425$ MHz	-17.43 dB	-17.95 dB	-21.78 dB
$f_C = 1500$ MHz	< -21.61 dB	< -23.54 dB	< -23.18 dB
$f_H = 1575$ MHz	-12.84 dB	-16.15 dB	-16.06 dB

Table 5.15: Measured microstrip PCB - Reflection and Isolation

Figure B.19 shows the path loss and Figure B.20 shows the path length in terms of phase. Table 5.16 summarises the path between beam port 1 and element ports 1 to 4.

The path loss is higher than what was seen in the AWR and CST simulations, which is expected, especially considering the slightly worse match. This is very significant at the high edge of the operating band, where the worst match is -12.84 dB. The path length also starts to show significant errors when compared to the ideal path length, having errors of multiple degrees.

Frequency	Transmission magnitude [dB]	s_{51} (ref) [°]	s_{61} [°]	s_{71} [°]	s_{81} [°]
$f_L = 1425$ MHz	-6.81 dB	0	-86.3	-50.7	-140
$f_C = 1500$ MHz	-6.89 dB	0	-86.3	-48.5	-138.3
$f_H = 1575$ MHz	-7.48 dB	0	-86.8	-45	-136.5

Table 5.16: Measured microstrip PCB - Beam port 1 bandwidth

Figure B.21 shows the path length in terms of phase. Table 5.17 summarises the path between beam port 2 and element ports 1 to 4.

Frequency	Transmission magnitude [dB]	s_{52} (ref) [°]	s_{62} [°]	s_{72} [°]	s_{82} [°]
$f_L = 1425$ MHz	-6.73 dB	0	-94.4	125.7	36
$f_C = 1500$ MHz	-6.73 dB	0	-95.1	126.7	37.4
$f_H = 1575$ MHz	-7.24 dB	0	-97.8	126.7	39.6

Table 5.17: Measured microstrip PCB - Beam port 2 bandwidth

Figure B.22 shows the path length in terms of phase. Table 5.18 summarises the path between beam port 3 and element ports 1 to 4.

Frequency	Transmission magnitude [dB]	s_{53} (ref) [°]	s_{63} [°]	s_{73} [°]	s_{83} [°]
$f_L = 1425$ MHz	-6.82 dB	0	90.2	-131.8	-37.3
$f_C = 1500$ MHz	-6.82 dB	0	89.8	-135.2	-40.6
$f_H = 1575$ MHz	-7.1 dB	0	86.4	-141.2	-46

Table 5.18: Measured microstrip PCB - Beam port 3 bandwidth

Figure B.23 shows the path length in terms of phase. Table 5.19 summarises the path between beam port 4 and element ports 1 to 4.

Frequency	Transmission magnitude [dB]	s_{54} (ref) [°]	s_{64} [°]	s_{74} [°]	s_{84} [°]
$f_L = 1425$ MHz	-6.87 dB	0	89.9	51.4	137.8
$f_C = 1500$ MHz	-7.04 dB	0	90.1	49.8	136.1
$f_H = 1575$ MHz	-7.55 dB	0	91	48	133.3

Table 5.19: Measured microstrip PCB - Beam port 4 bandwidth

Table 5.20 summarises the progressive phase shifts, similar to Table 5.6 and the same column/row swaps are done. The progressive phase shift is not consistent over element ports, thus the average of the phase shifts are taken and the result is what is displayed in the ψ -column.

Even though the relative phase shifts show significant errors ($< 10^\circ$), when looking at the average progressive phase shift, it doesn't differ that significantly from the ideal case. To see what effect this error will have on the resulting beam angle, ψ_a is used in equation 3.2.10. For an array spacing of $d = \frac{\lambda}{2}$, $\theta_a = -14.84^\circ$, as opposed to $\theta_a = -14.48^\circ$ when $\psi_a = -45$. This is just a rough approximation, as ψ_a is an average.

	Element port				ψ
Beam port	1	3	2	4	
1	0	-48.5	-86.3	-138.3	$\psi_a \approx -46.1$
3	0	-135.2	89.8	-40.6	$\psi_b \approx -133.5$
2	0	126.7	-95.1	37.4	$\psi_c \approx 132.5$
4	0	49.8	90.1	136.1	$\psi_d \approx 45.4$

Table 5.20: Measured microstrip PCB - Progressive phase shift

The results obtained from this measurement provides enough confidence that this BFN will work as hypothesised. The next step is to connect this circuit to an antenna and measure the resulting radiation patterns.

5.2.3 Measured Antenna Patterns

The setup is as described in section 4.3.3 and the measured radiation pattern will be discussed in this section. Figure 5.1 shows the normalised gain pattern that was measured. Each beam port had to be excited individually, because a 2-port network analyser was used. This limited the measurement in that simultaneous beamforming could not be evaluated.

The result is very similar to figure 3.5, which confirms that this implementation of the Butler Matrix works. The sidelobes are quite high, but this is an issue that can likely be solved by increasing the number of elements (and the order of the Butler Matrix).

5.3 Microstrip Implementation at 15 GHz

5.3.1 Simulated

This implementation was simulated and is discussed in section 4.4.1. The simulation is a full wave simulation of a 3D model, built in CST Studio. The

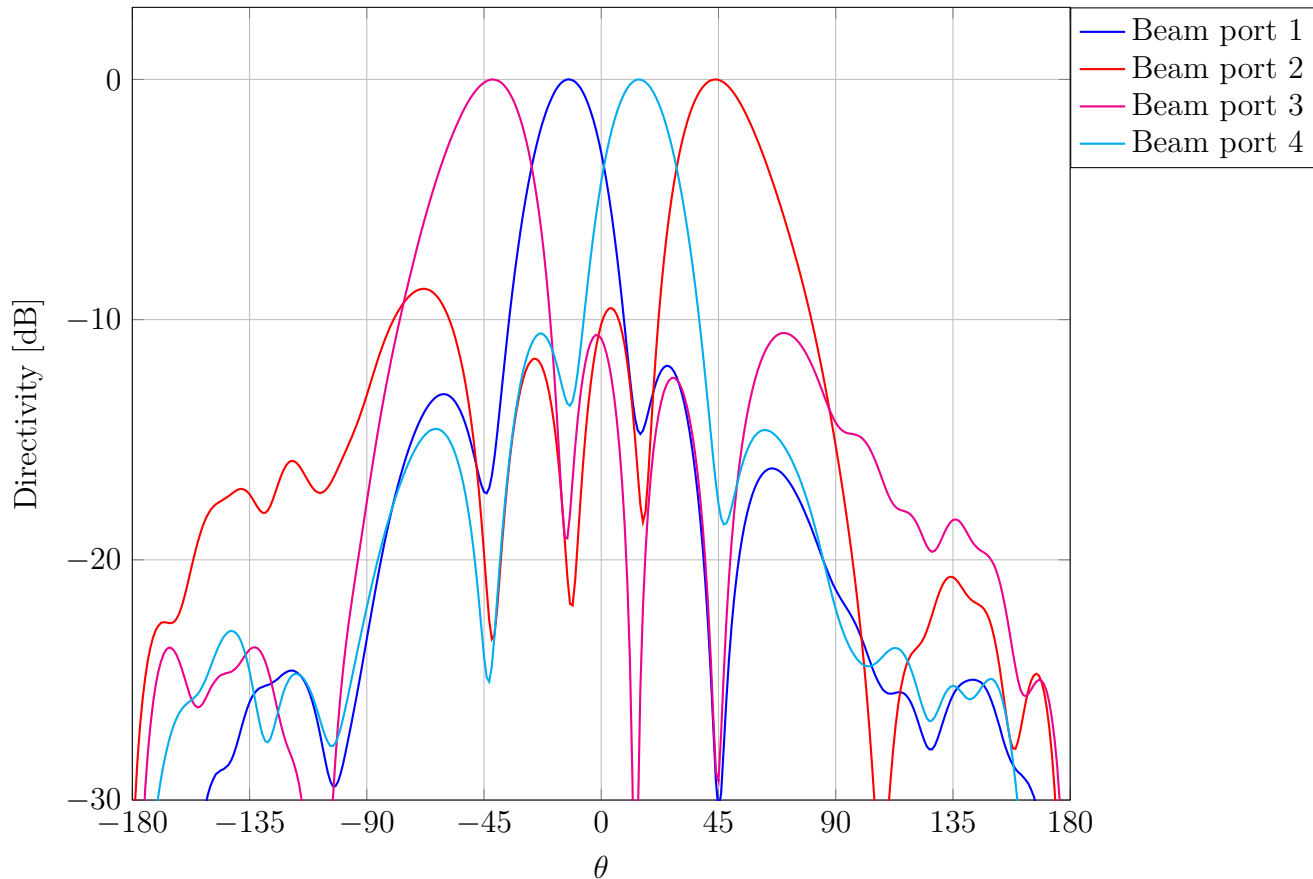


Figure 5.1: Butler Matrix, patch antenna integration - Directivity, normalised

results are discussed in this section. Similar to section 5.1, an operating bandwidth of 10% will be assumed, but this time centred around 15 GHz, and all the s -parameters are graphed in Appendix B.

Figure B.31 shows the input reflection. Figure B.32 shows the beam port isolation. Figure B.33 shows the path loss and figure B.34 shows the path length in terms of phase. Table 5.21 summarises the path between beam port 1 and element ports 1 to 4.

The first thing to note is that the loss is significantly higher. The match is surprisingly good, and the isolation is very good. The phase lengths seem to be shifted in frequency. At the low end of the operating band, the phase is closer to what is expected than at the centre frequency.

Frequency	Transmission magnitude [dB]	s_{51} (ref) [°]	s_{61} [°]	s_{71} [°]	s_{81} [°]
$f_L = 14250$ MHz	-7.85 dB	0	-91.6	-45.6	-135.7
$f_C = 15000$ MHz	-7.79 dB	0	-86.9	-50.4	-140.9
$f_H = 15750$ MHz	-7.81 dB	0	-84.7	-54.8	-146.5

Table 5.21: CST Simulation - Beam port 1 bandwidth, 15 GHz

Figure B.35 shows the path length in terms of phase. Table 5.22 summarises the path between beam port 2 and element ports 1 to 4.

The phase lengths once again seem to be closer to the expected value at the lower end of the operating band.

Frequency	Transmission magnitude [dB]	s_{52} (ref) [°]	s_{62} [°]	s_{72} [°]	s_{82} [°]
$f_L = 14250$ MHz	-7.78 dB	0	268.9	135	46.1
$f_C = 15000$ MHz	-7.63 dB	0	-91.1	127.2	36.5
$f_H = 15750$ MHz	-8.25 dB	0	-92.6	122.6	29.8

Table 5.22: CST Simulation - Beam port 2 bandwidth, 15 GHz

Figure B.36 shows the path length in terms of phase. Table 5.23 summarises the path between beam port 3 and element ports 1 to 4.

The phase lengths once again seem to be closer to the expected value at the lower end of the operating band.

Frequency	Transmission magnitude [dB]	s_{53} (ref) [°]	s_{63} [°]	s_{73} [°]	s_{83} [°]
$f_L = 14250$ MHz	-7.76 dB	0	88.9	221.9	-47.1
$f_C = 15000$ MHz	-7.64 dB	0	90.7	231.7	-37.4
$f_H = 15750$ MHz	-8.25 dB	0	92.75	236.8	-30.9

Table 5.23: CST Simulation - Beam port 3 bandwidth, 15 GHz

Figure B.37 shows the path length in terms of phase. Table 5.24 summarises the path between beam port 4 and element ports 1 to 4.

The phase lengths once again seem to be closer to the expected value at the lower end of the operating band.

Frequency	Transmission magnitude [dB]	s_{54} (ref) [°]	s_{64} [°]	s_{74} [°]	s_{84} [°]
$f_L = 14250$ MHz	-7.81 dB	0	90	43.1	134.8
$f_C = 15000$ MHz	-7.77 dB	0	90.44	53.2	140
$f_H = 15750$ MHz	-7.81 dB	0	91.7	60.95	145.6

Table 5.24: CST Simulation - Beam port 4 bandwidth, 15 GHz

Table 5.25 summarises the progressive phase shifts, similar to table 5.6 and the same column/row swaps are done. The progressive phase shift is not consistent over element ports, thus the average of the phase shifts are taken and the result is what is displayed in the ψ -column.

In this case the phase lengths errors are quite significant, but the average progressive phase shift doesn't seem to be that far off of the expected value.

	Element port				ψ
Beam port	1	3	2	4	
1	0	-50.4	-86.9	-140.9	$\psi_a \approx -46.97$
3	0	-128.3	90.7	-37.4	$\psi_b \approx -132.47$
2	0	127.2	-91.1	36.5	$\psi_c \approx 132.17$
4	0	53.2	90.44	140	$\psi_d \approx 46.67$

Table 5.25: CST Simulation - Progressive phase shift, 15 GHz

5.3.2 Measured

This circuit is discussed in section 4.4.2. Similar to section 5.1, an operating bandwidth of 10% will be assumed, but this time centred around 15 GHz, and all the s -parameters are graphed in Appendix B.

Figure B.38 shows the input reflection. Figure B.39 shows the beam port and element port isolation. Figure B.40 shows the path loss and figure B.41 shows the path length in terms of phase. Table 5.26 summarises the path between beam port 1 and element ports 1 to 4.

The losses in this circuit are unacceptable. The match is also unacceptable, which contributes to the bad losses. Isolation is acceptable. The path lengths are off by, significantly more than was seen in section 5.3.1. In the same way, the path length is much closer to the ideal at the bottom end of the operating band. There is clearly a pattern emerging.

Frequency	Transmission magnitude [dB]	s_{51} (ref) [°]	s_{61} [°]	s_{71} [°]	s_{81} [°]
$f_L = 14250$ MHz	-10.1 dB	0	-79.2	-38.2	-134.5
$f_C = 15000$ MHz	-9.44 dB	0	-85.5	-53.4	-148.8
$f_H = 15750$ MHz	-10.45 dB	0	-83.2	-59	-146.3

Table 5.26: Measured PCB - Beam port 1 bandwidth, 15 GHz

Figure B.42 shows the path length in terms of phase. Table 5.27 summarises the path between beam port 2 and element ports 1 to 4.

The phase lengths once again seem to be closer to the expected value at the lower end of the operating band.

Frequency	s_{52} (ref) [°]	s_{62} [°]	s_{72} [°]	s_{82} [°]
$f_L = 14250$ MHz	0	272.9	129.2	41.4
$f_C = 15000$ MHz	0	277.1	129.6	34
$f_H = 15750$ MHz	0	269.5	114.9	23.17

Table 5.27: Measured PCB - Beam port 2 bandwidth, 15 GHz

Figure B.43 shows the path length in terms of phase. Table 5.28 summarises the path between beam port 3 and element ports 1 to 4.

The phase lengths once again seem to be closer to the expected value at the lower end of the operating band.

Frequency	s_{53} (ref) [°]	s_{63} [°]	s_{73} [°]	s_{83} [°]
$f_L = 14250$ MHz	0	88.1	226.5	-45.3
$f_C = 15000$ MHz	0	95.7	238.1	-38
$f_H = 15750$ MHz	0	90.7	241.2	-29.6

Table 5.28: Measured PCB - Beam port 3 bandwidth, 15 GHz

Figure B.44 shows the path length in terms of phase. Table 5.29 summarises the path between beam port 4 and element ports 1 to 4.

The phase lengths once again seem to be closer to the expected value at the lower end of the operating band.

Frequency	s_{54} (ref) [°]	s_{64} [°]	s_{74} [°]	s_{84} [°]
$f_L = 14250$ MHz	0	96.7	51.6	129.5
$f_C = 15000$ MHz	0	94.7	57.8	143.9
$f_H = 15750$ MHz	0	85	56.7	138.8

Table 5.29: Measured PCB - Beam port 4 bandwidth, 15 GHz

Table 5.30 summarises the progressive phase shifts, similar to table 5.6 and the same column/row swaps are done. The progressive phase shift is not consistent over element ports, thus the average of the phase shifts are taken and the result is what is displayed in the ψ -column.

With the physical circuit, the losses are completely unacceptable, but some information can still be derived by looking at the path lengths. The path lengths at the center frequency are far off from the ideal, but at the low end of the operating band they are much closer. For this reason the average progressive phase shift is calculated for the low end of the band as well, and is shown in Table 5.31.

One explanation for this phenomenon is that the effective length is incorrect. This can be attributed to a mismatch in the dielectric constant design value and the actual dielectric constant of the manufactured PCB. It can also be manufacturing tolerances and defects, such as board height, or etch dimensions. The interface to the board (SMA connector) is soldered on, and there is some variation in the way each connector is soldered on, which causes a slight variation in input impedance and phase length.

	Element port				ψ
Beam port	1	3	2	4	
1	0	-53.4	-85.5	-148.8	$\psi_a \approx -49.6$
3	0	238.1	95.7	-38	$\psi_b \approx -132.67$
2	0	129.6	277.1	34	$\psi_c \approx 132.337$
4	0	57.8	94.7	143.9	$\psi_d \approx 47.97$

Table 5.30: Measured PCB - Progressive phase shift, 15 GHz

	Element port				ψ
Beam port	1	3	2	4	
1	0	-38.2	-79.2	-134.5	$\psi_a \approx -44.83$
3	0	226.5	88.1	-45.3	$\psi_b \approx -135.1$
2	0	129.2	272.9	41.4	$\psi_c \approx 133.8$
4	0	51.6	96.7	129.5	$\psi_d \approx 43.17$

Table 5.31: Measured PCB - Progressive phase shift, 14.25 GHz

Chapter 6

Conclusion

The main aim of this thesis was to analyse the Butler Matrix as a simultaneous, multiple beam beamforming network. A brief discussion was done on antennas and antenna arrays, to achieve a general understanding to the radiation properties thereof. This helps the reader in understanding some of the basics behind antenna arrays before the Butler Matrix was introduced.

The Butler Matrix concept was then broken down and analysed mathematically to support one of the defining characteristics of the Butler Matrix, orthogonal beams. Some of the limitations of the Butler Matrix were brought to light, followed by a generalised derivation, indicating its scalability.

The viability of the Butler Matrix was then established through the investigation of 2 different implementations. The first implementation worked very well. Good isolation was achieved between beam ports (and between antenna ports), and the network was matched to 50Ω over the operating bandwidth. The progressive phase shifts were as expected, within some margin of error and proved the viability of the Butler Matrix as a BFN.

The second implementation didn't work as well, which was a result of manufacturing tolerances. This issue can likely be solved with another iteration of the same design, as the design did execute its function, just with degraded results.

Finally the thesis concluded with a chapter discussing the results that were obtained through simulation and practical measurement. The results supported the theoretical analyses of the Butler Matrix that was discussed.

Future Work

- **Higher order Butler Matrices** - Some of the theory behind N^{th} -order Butler Matrices was briefly discussed, but the discussion didn't include any specific analyses or examples. No implementations were suggested for Butler Matrices higher than 4^{th} -order. There would be value in investigating higher order Butler Matrices, as the effect of higher

orders would probably be similar to the effect of increasing the number of elements in a conventional array.

- **More real world tests - Complex modulations** - More measurements could be done involving real world scenarios. One such a scenario is the effect that complex modulated signals have on simultaneous beams. It was proven in this thesis that changing the excitation amplitude on one beam port has very little effect on the perceived gain in a beam associated with a different beam port, which is a consequence of the beams' orthogonality. Applying complex modulated signals (modulation techniques utilising phase and amplitude) might have an effect on orthogonality since orthogonality is established using phase related components in the implementation.
- **Two-dimensional/Cascaded Butler Matrices** - The Butler Matrix concept discussed in this thesis only considers it as a beamforming network that can change the angle of the main beam in one angular dimension. Many practical applications require beams to be directed in more than one angular dimension, for example Azimuth and Elevation. These are known as 2D-BFN's. Ding and Kishk (2018) have done research on this topic.

Appendices

Appendix A

$M \times N$ Planar Array Factor Derivation

Similar to the analysis in 2.1.4, each element in the array is excited with magnitude E_{nm} and phase ξ_{nm} . The radiation pattern used for each element is $F_{nm}(\theta_{nm}, \phi_{nm})$. The total E-field is:

$$E_t = \sum_{n=1}^N \sum_{m=1}^M E_{nm} F_{nm}(\theta_{nm}, \phi_{nm}) \frac{e^{j\xi_{nm}} e^{-jk r_{nm}}}{r_{nm}} \quad (\text{A.0.1})$$

The far-field approximation simplifies the following terms:

- $\theta_{nm} \approx \theta$
- $\phi_{nm} \approx \phi$
- $\frac{1}{r_{nm}} \approx \frac{1}{r_{11}} = \frac{1}{r}$

Thus:

$$E_t = \sum_{n=1}^N \sum_{m=1}^M E_{nm} F_{nm}(\theta, \phi) \frac{e^{j\xi_{nm}} e^{-jk r_{nm}}}{r} \quad (\text{A.0.2})$$

The r_{nm} factor in the phase term ($e^{-jk r_{nm}}$) needs some other simplification as a very small difference in in this term will lead to a significant difference in phase. From figure A.1 a better approximation for r_{nm} can be made (which translates to a certain phase difference at a specific frequency).

Assume that the plane wave is arriving from angles θ and ϕ . With element 11 as reference, the differential distance can be calculated for each element in the array, in terms of r_{11} (or just r) (Balanis, 2012). The differential distance from the origin (for element 32 as example) is shown in figure A.1 as Δr_{nm} .

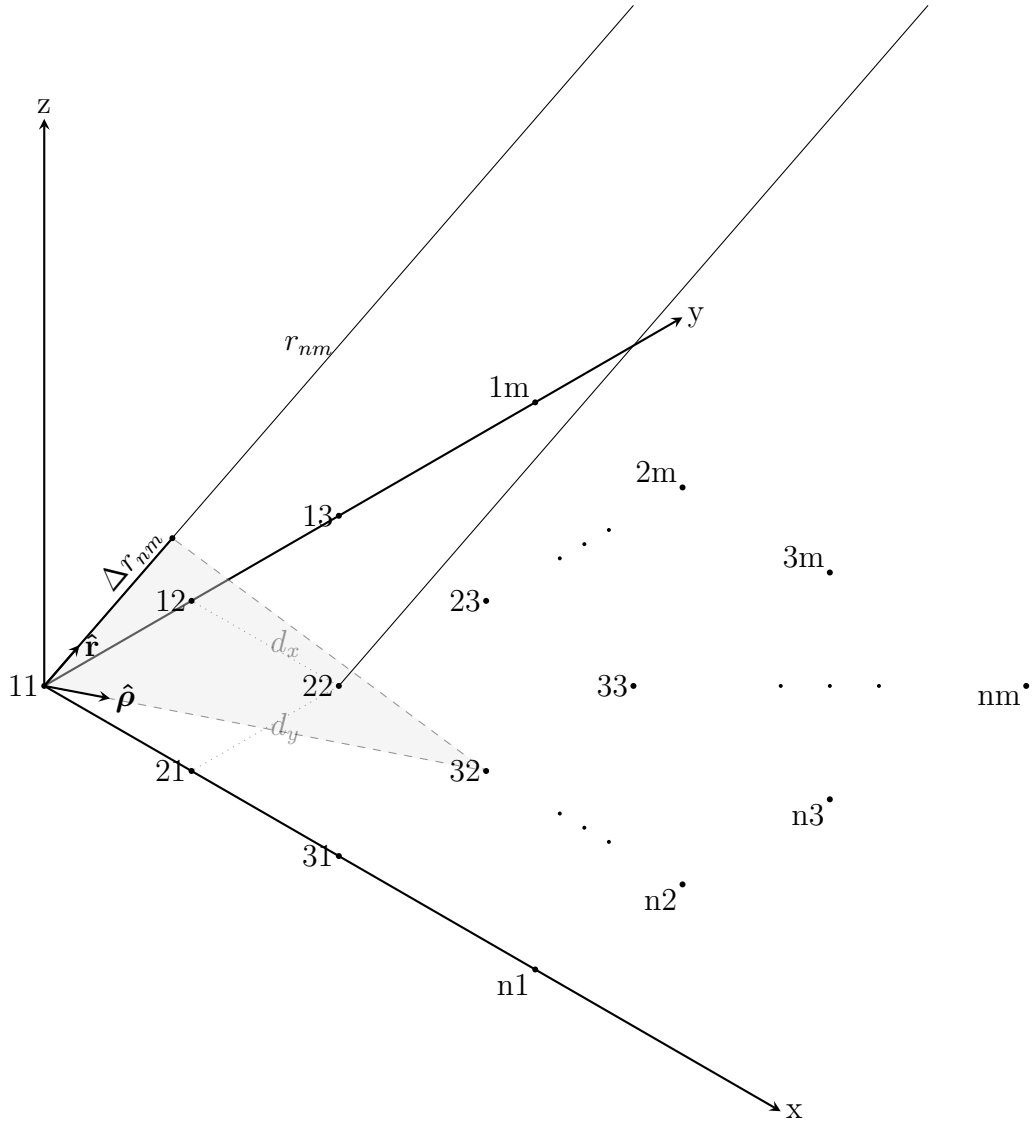


Figure A.1: 2D Planar Array

The elements are spaced d_x apart in the x -direction and d_y apart in the y -direction. The coordinates of element nm is $(nd_x, md_y, 0)$, where n and m relates to the nm^{th} element. The distance from the reference element to the nm^{th} element is thus:

$$d_{nm} = \sqrt{(nd_x)^2 + (md_y)^2} \quad (\text{A.0.3})$$

The unit vector $\hat{\mathbf{r}}$ is the direction from which the plane wave is arriving (in terms of θ and ϕ). The unit vector $\hat{\boldsymbol{\rho}}$ is the direction from the reference element to element nm . The angle ψ between the unit vectors $\hat{\mathbf{r}}$ and $\hat{\boldsymbol{\rho}}$ can be found by taking the dot-product of these unit vectors.

$$\hat{\mathbf{r}} = \sin \theta \cos \phi \hat{\mathbf{x}} + \sin \theta \sin \phi \hat{\mathbf{y}} + \cos \theta \hat{\mathbf{z}} \quad (\text{A.0.4})$$

$$\hat{\boldsymbol{\rho}} = \frac{md_x}{\sqrt{(nd_x)^2 + (md_y)^2}} \hat{\mathbf{x}} + \frac{nd_y}{\sqrt{(nd_x)^2 + (md_y)^2}} \hat{\mathbf{y}} \quad (\text{A.0.5})$$

$$= \frac{md_x}{d_{nm}} \hat{\mathbf{x}} + \frac{nd_y}{d_{nm}} \hat{\mathbf{y}} \quad (\text{A.0.6})$$

$$\hat{\mathbf{r}} \cdot \hat{\boldsymbol{\rho}} = \cos \psi \quad (\text{A.0.7})$$

The differential distance can then be calculated:

$$\Delta r_{nm} = d_{nm} \cos \psi \quad (\text{A.0.8})$$

$$= d_{nm} \hat{\mathbf{r}} \cdot \hat{\boldsymbol{\rho}} \quad (\text{A.0.9})$$

$$= d_{nm} \left(\frac{\sin \theta \cos \phi md_x}{d_{nm}} + \frac{\sin \theta \sin \phi nd_y}{d_{nm}} \right) \quad (\text{A.0.10})$$

$$= \sin \theta \cos \phi md_x + \sin \theta \sin \phi nd_y \quad (\text{A.0.11})$$

r_{nm} can now be written in terms of r :

$$r_{nm} = r - \Delta r_{nm} \quad (\text{A.0.12})$$

This is substituted back into the phase term ($e^{-j\beta r_{nm}}$), in the E-field equation A.0.2:

$$E_t = \sum_{n=1}^N \sum_{m=1}^M E_{nm} F_{nm}(\theta, \phi) \frac{e^{j\xi_{nm}} e^{-jkr} e^{jk\Delta r_{nm}}}{r} \quad (\text{A.0.13})$$

$$= \frac{e^{-jkr}}{r} \sum_{n=1}^N \sum_{m=1}^M E_{nm} F_{nm}(\theta, \phi) e^{j\xi_{nm}} e^{jk\Delta r_{nm}} \quad (\text{A.0.14})$$

To further simplify A.0.14, identical element patterns can be used, and uniform amplitude excitation can be applied, thus:

$$E_t = E_{max} \frac{F(\theta, \phi)}{r} e^{-jkr} \sum_{n=1}^N \sum_{m=1}^M e^{j\xi_{nm}} e^{jk\Delta r_{nm}} \quad (\text{A.0.15})$$

Appendix B

Results - Graphs

B.1 Butler Matrix results - Ideal

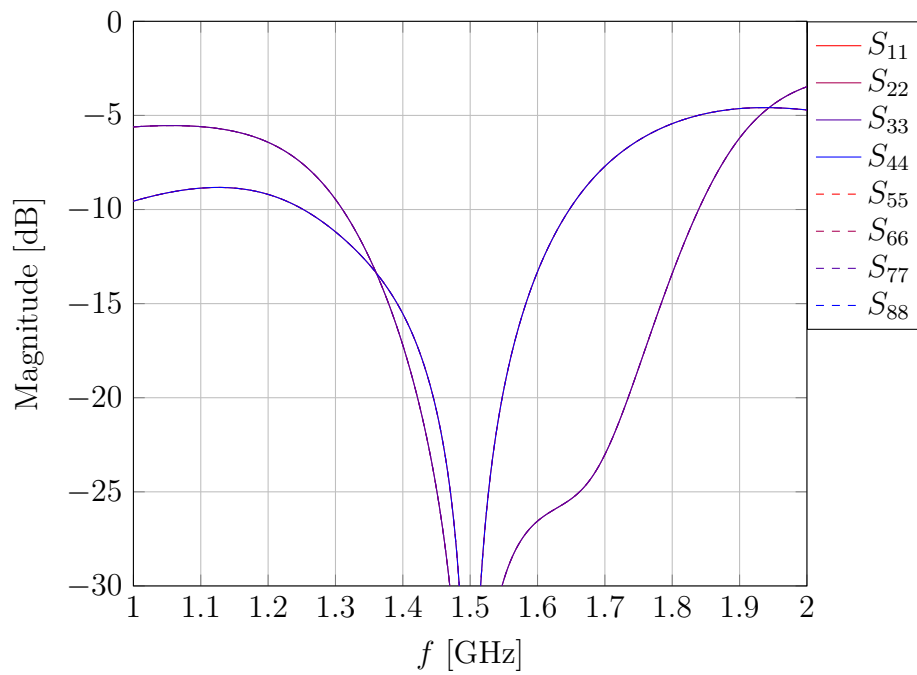


Figure B.1: AWR Ideal simulation - Reflection

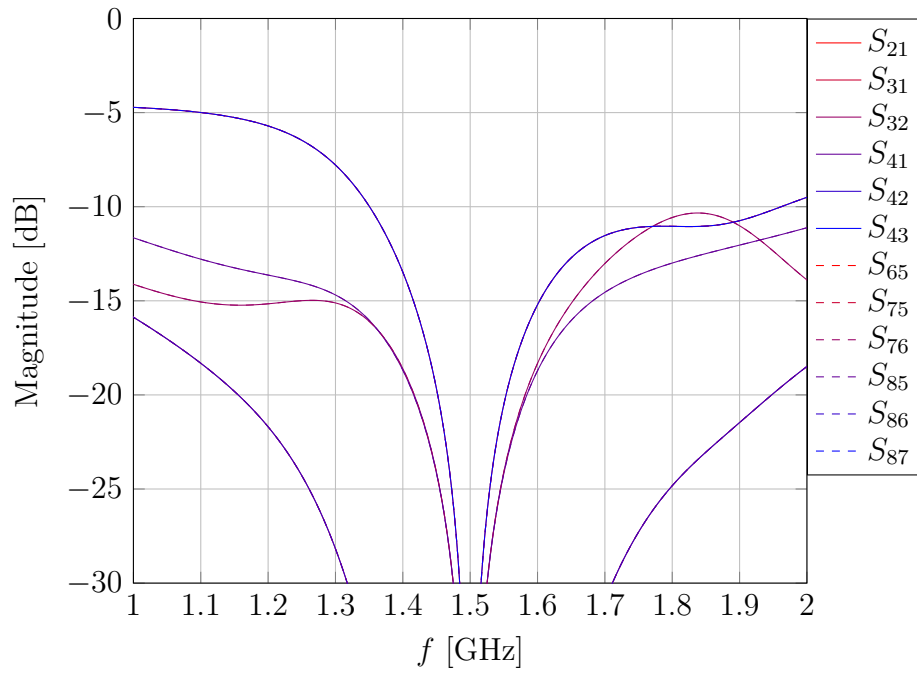


Figure B.2: AWR Ideal simulation - Isolation

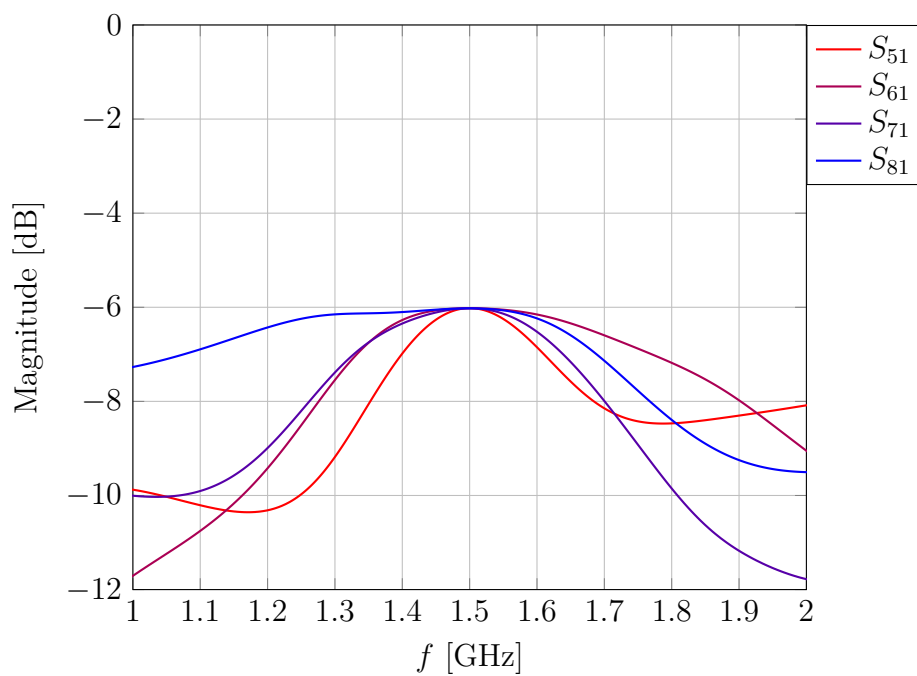


Figure B.3: AWR Ideal simulation - Transmission magnitude, beam port 1

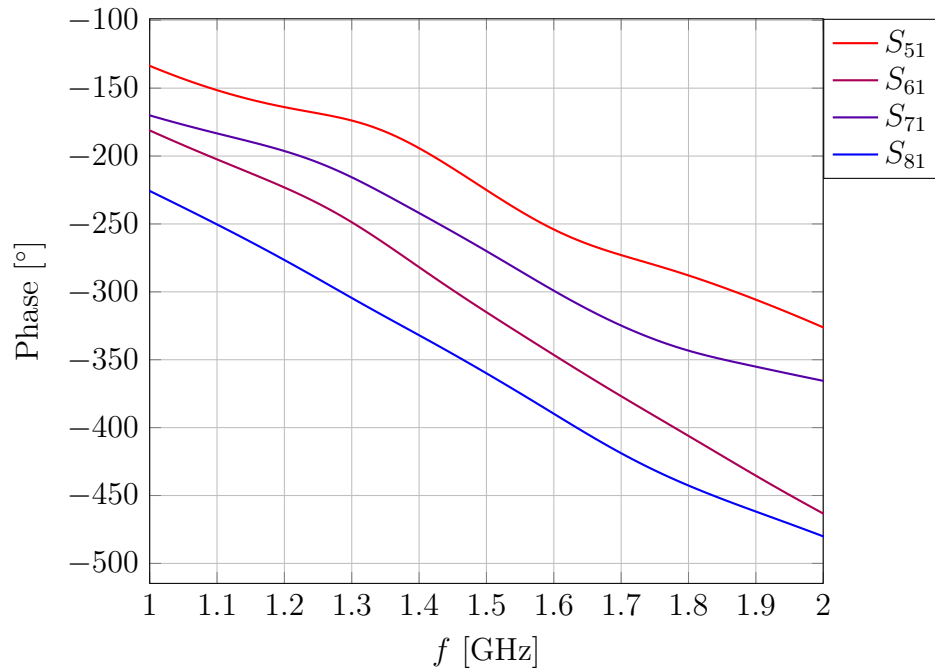


Figure B.4: AWR Ideal simulation - Transmission phase, beam port 1

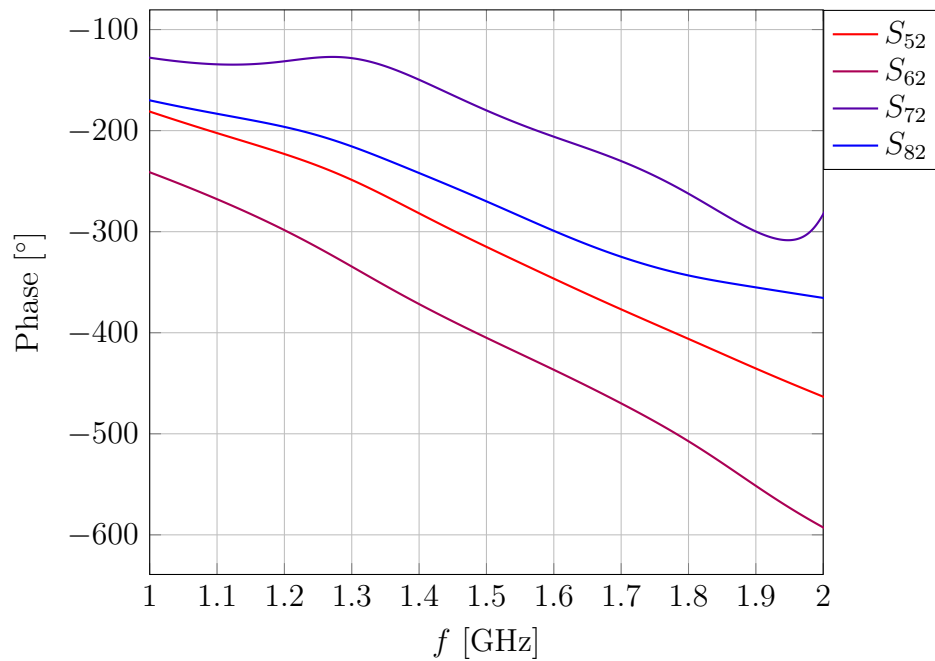


Figure B.5: AWR Ideal simulation - Transmission phase, beam port 2

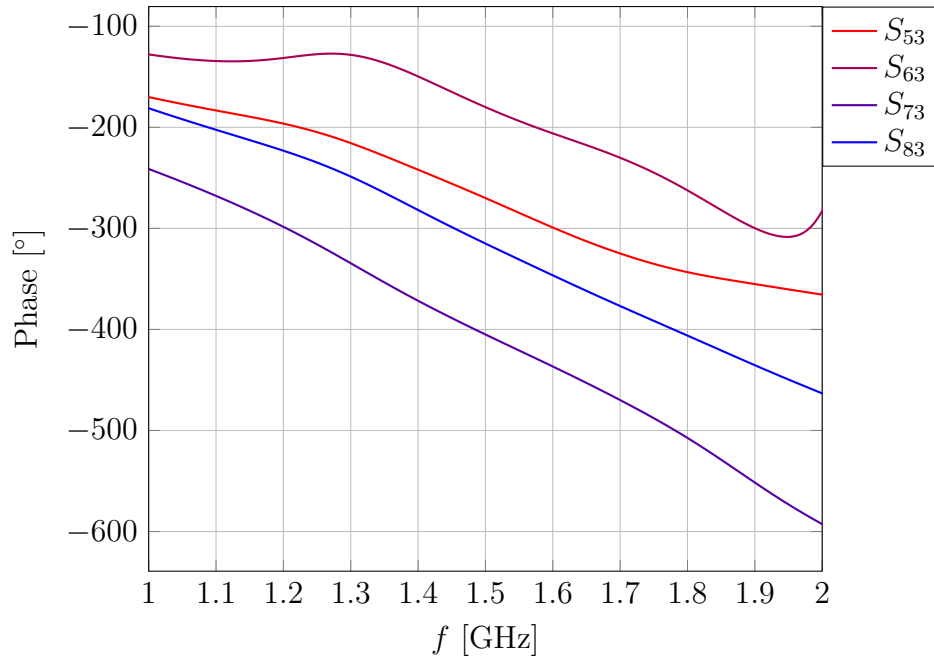


Figure B.6: AWR Ideal simulation - Transmission phase, beam port 3

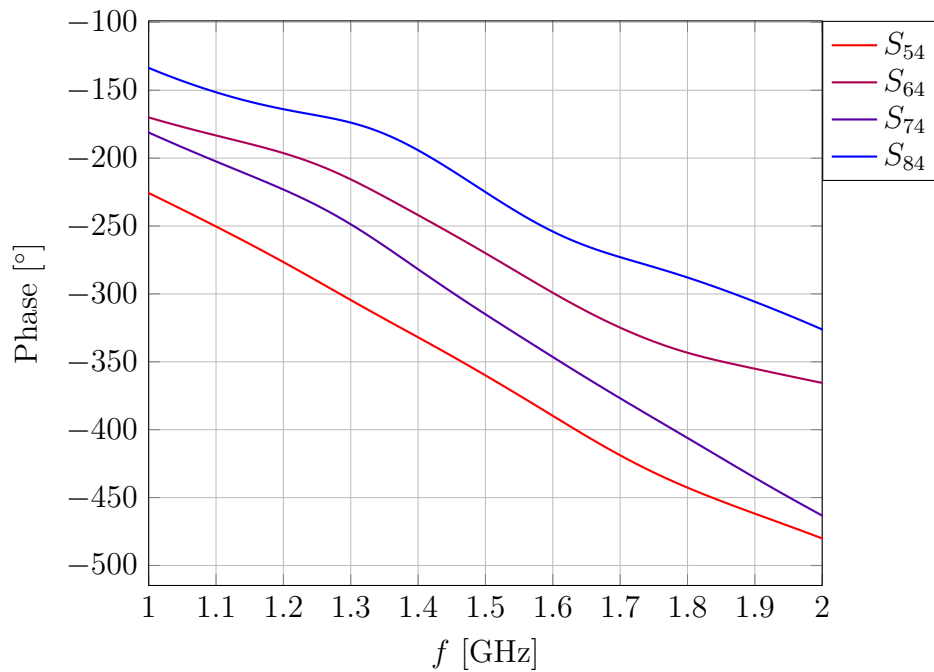


Figure B.7: AWR Ideal simulation - Transmission phase, beam port 4

B.2 Butler Matrix results - Microstrip, CST and AWR simulation

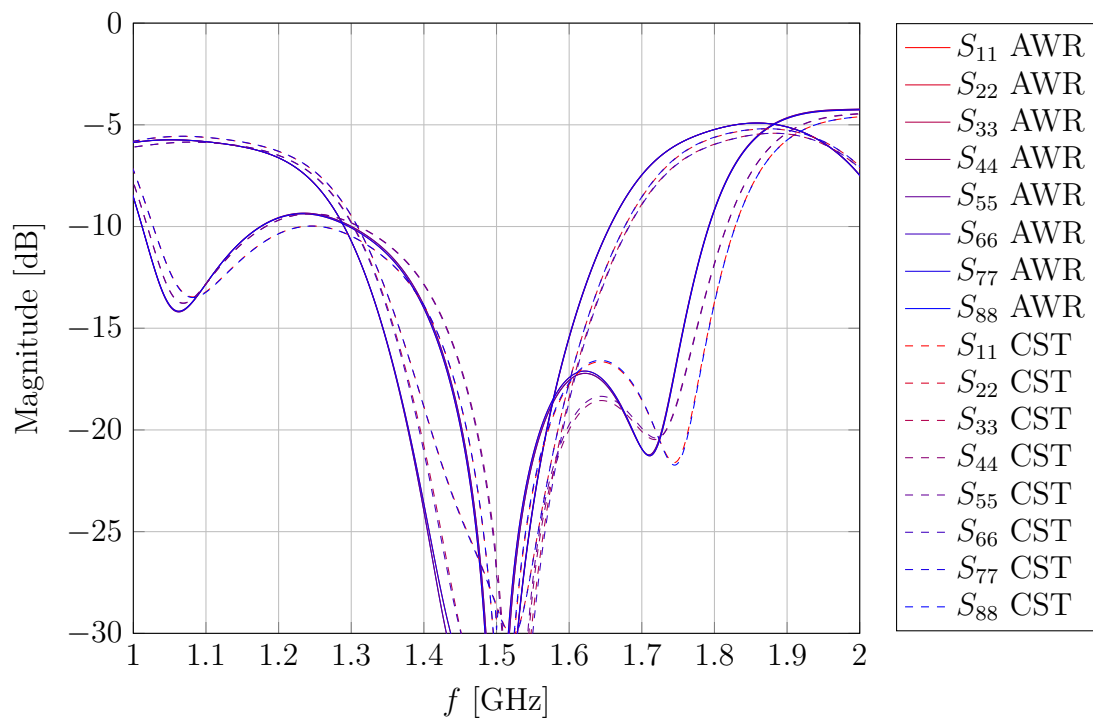


Figure B.8: Microstrip CST and AWR simulation - Reflection

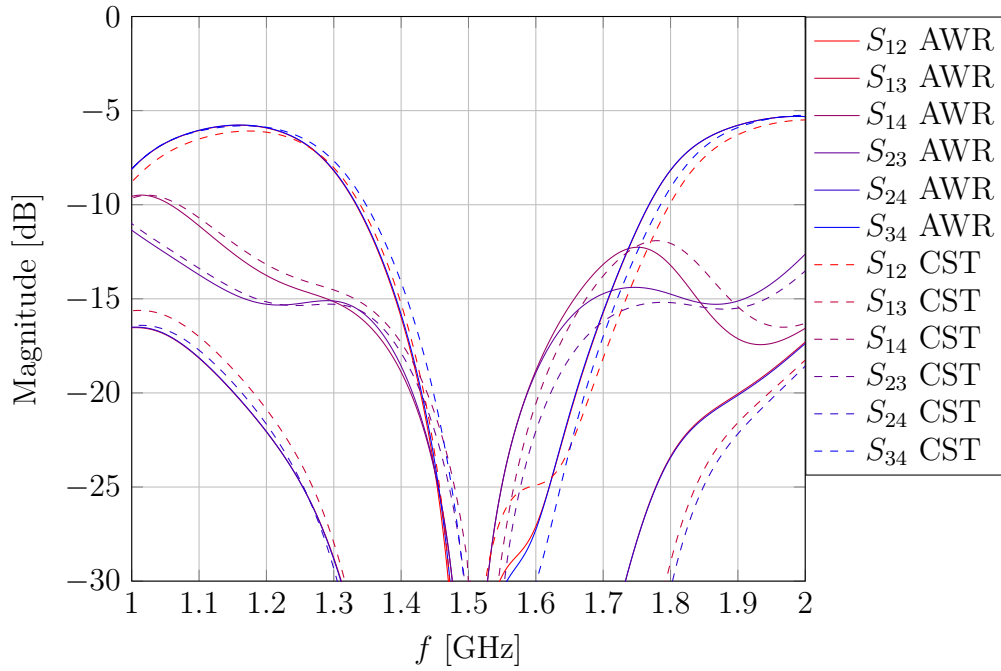


Figure B.9: Microstrip CST and AWR simulation - Beam port isolation

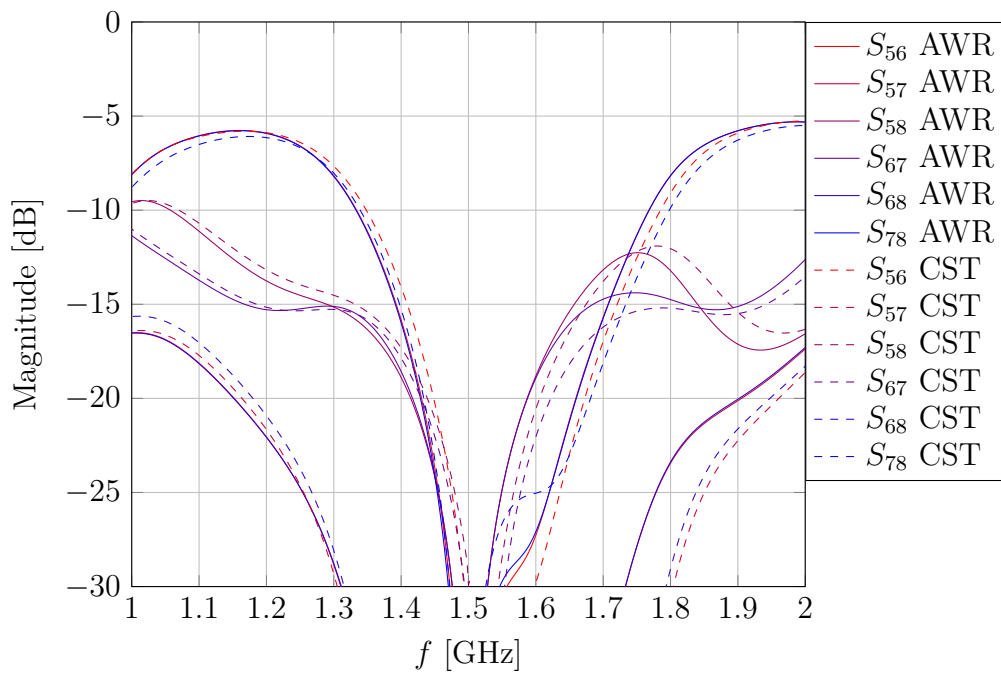


Figure B.10: Microstrip CST and AWR simulation - Element port isolation

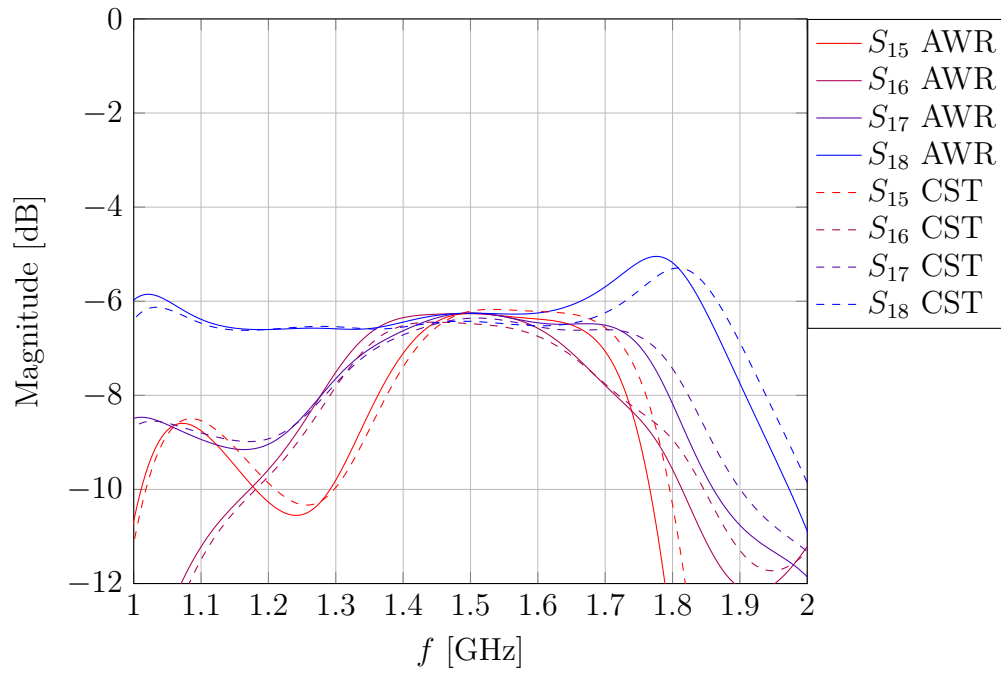


Figure B.11: Microstrip CST and AWR simulation - Transmission magnitude, beam port 1

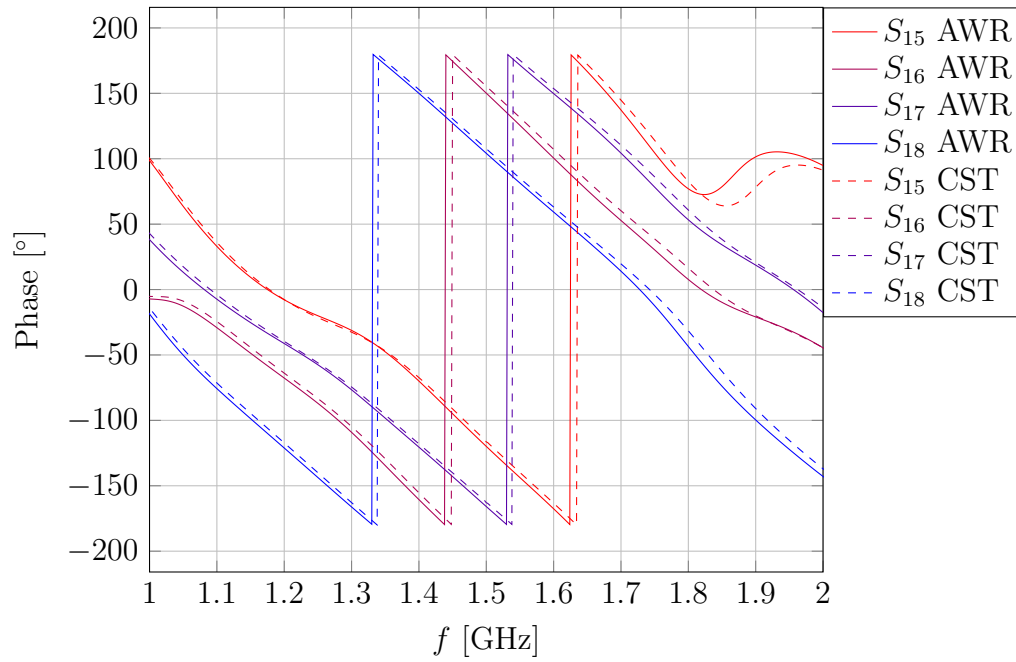


Figure B.12: Microstrip CST and AWR simulation - Transmission phase, beam port 1

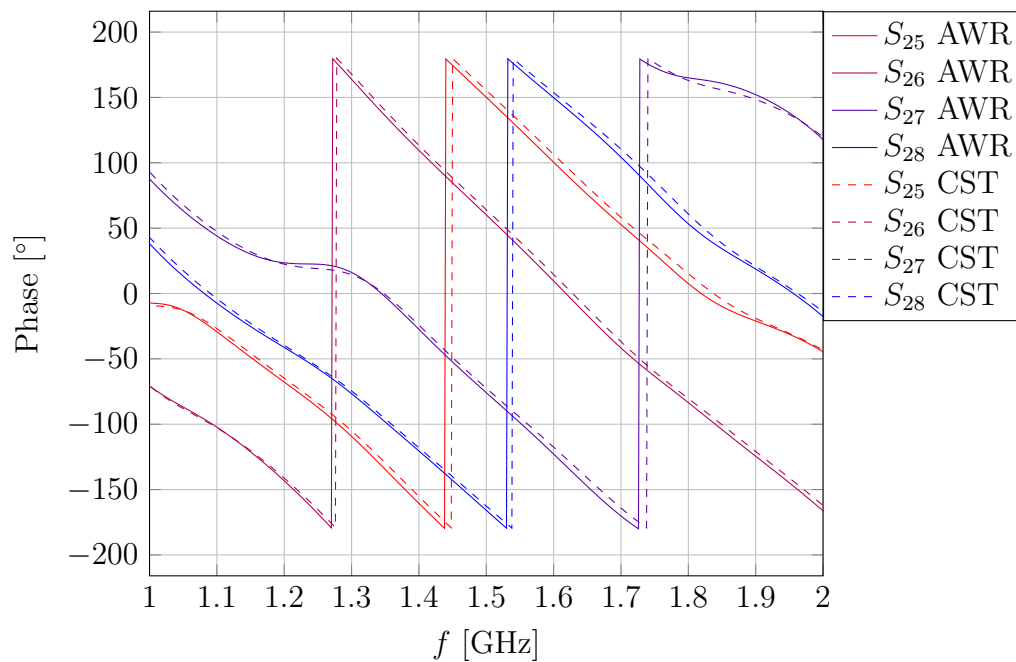


Figure B.13: Microstrip CST and AWR simulation - Transmission phase, beam port 2

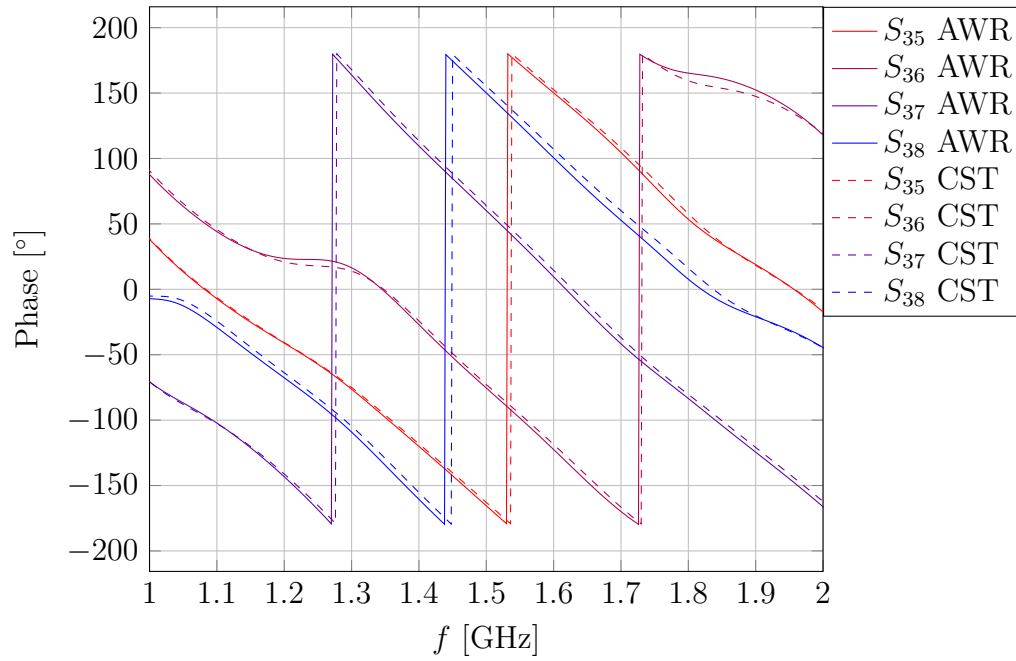


Figure B.14: Microstrip CST and AWR simulation - Transmission phase, beam port 3

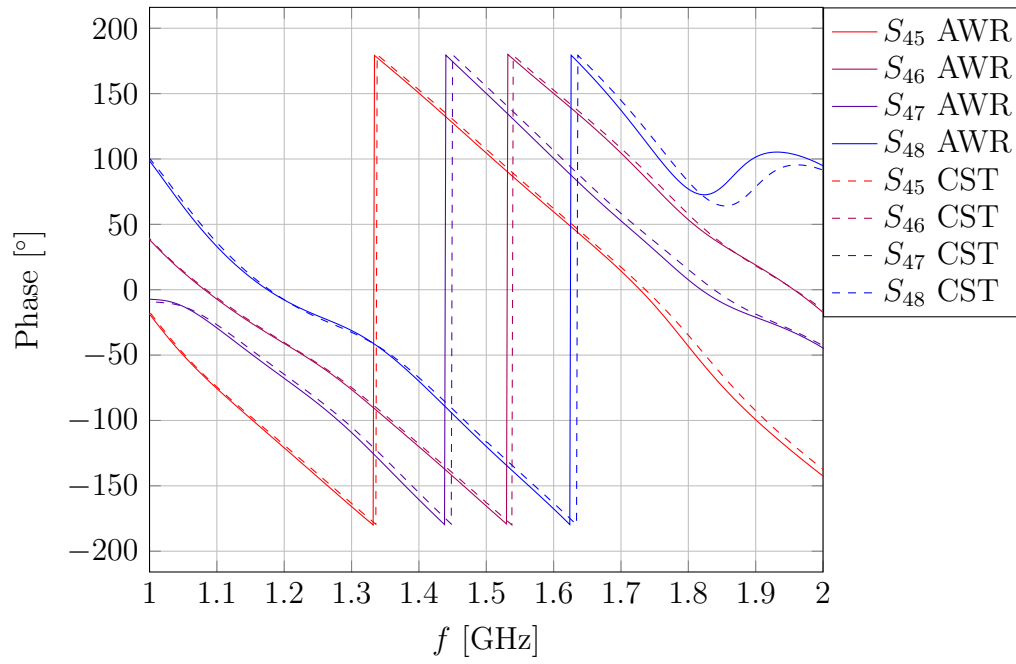


Figure B.15: Microstrip CST and AWR simulation - Transmission phase, beam port 4

B.3 Butler Matrix results - Measured PCB

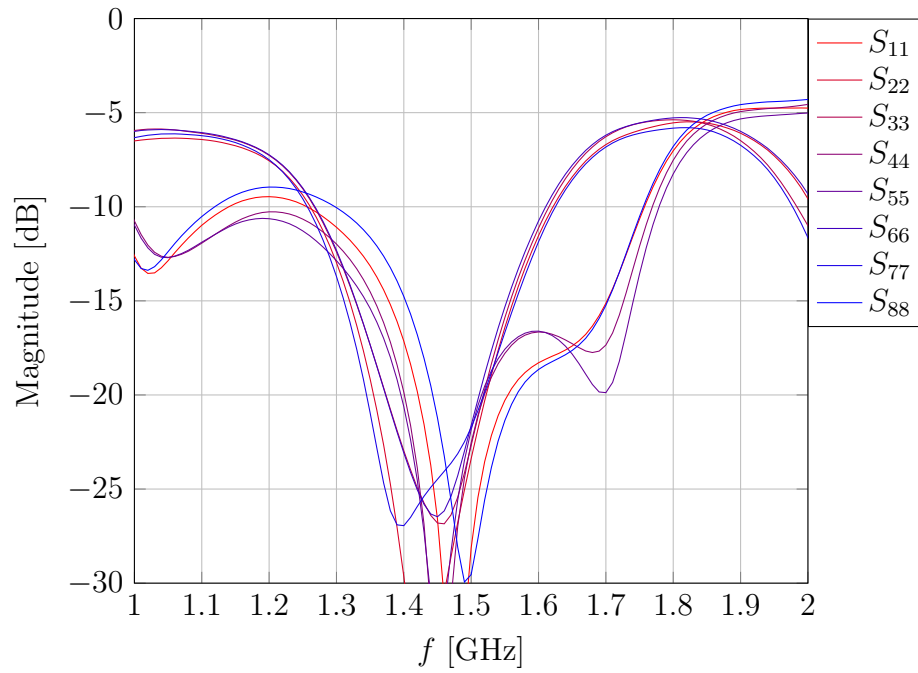


Figure B.16: Measured microstrip PCB - Reflection

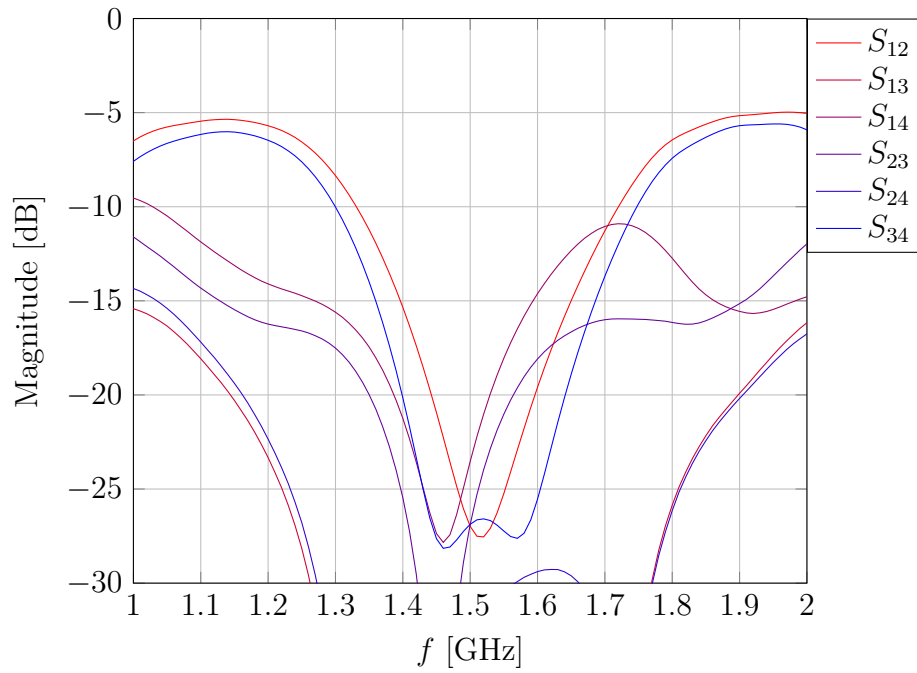


Figure B.17: Measured microstrip PCB - Beam port isolation

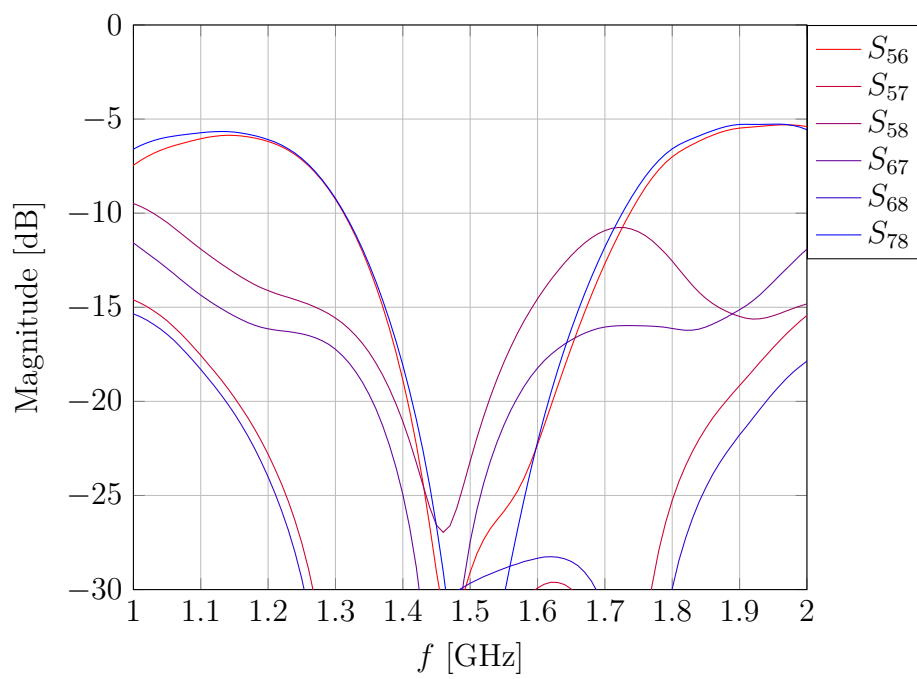


Figure B.18: Measured microstrip PCB - Element port isolation

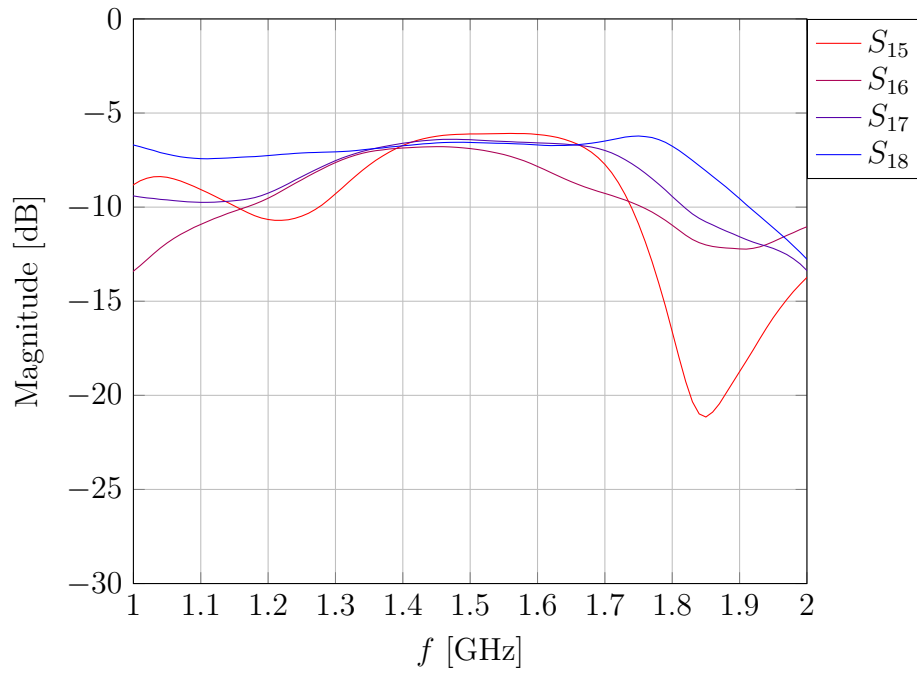


Figure B.19: Measured microstrip PCB - Transmission magnitude, beam port 1

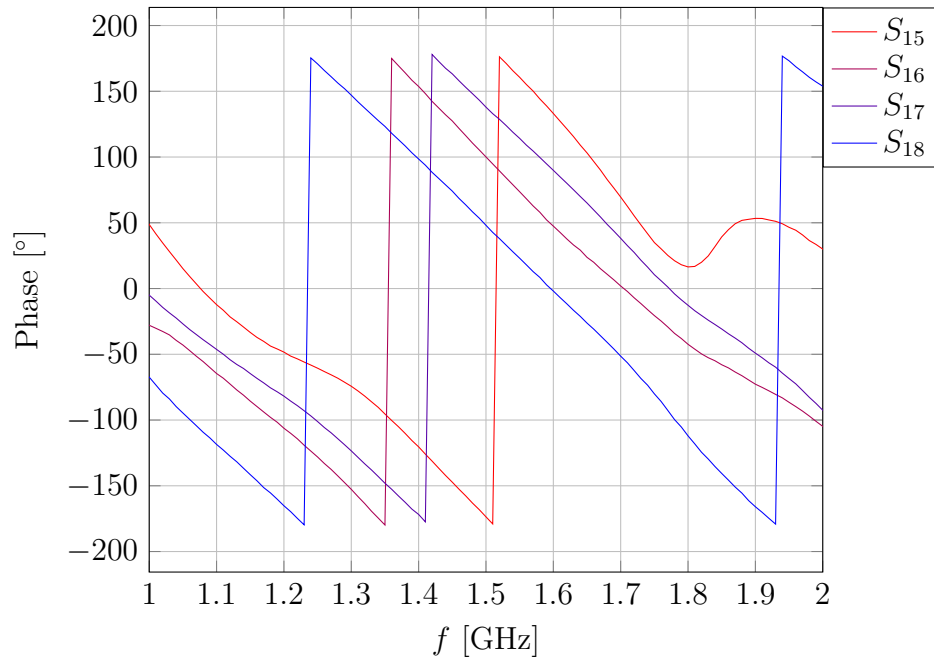


Figure B.20: Measured microstrip PCB - Transmission phase, beam port 1

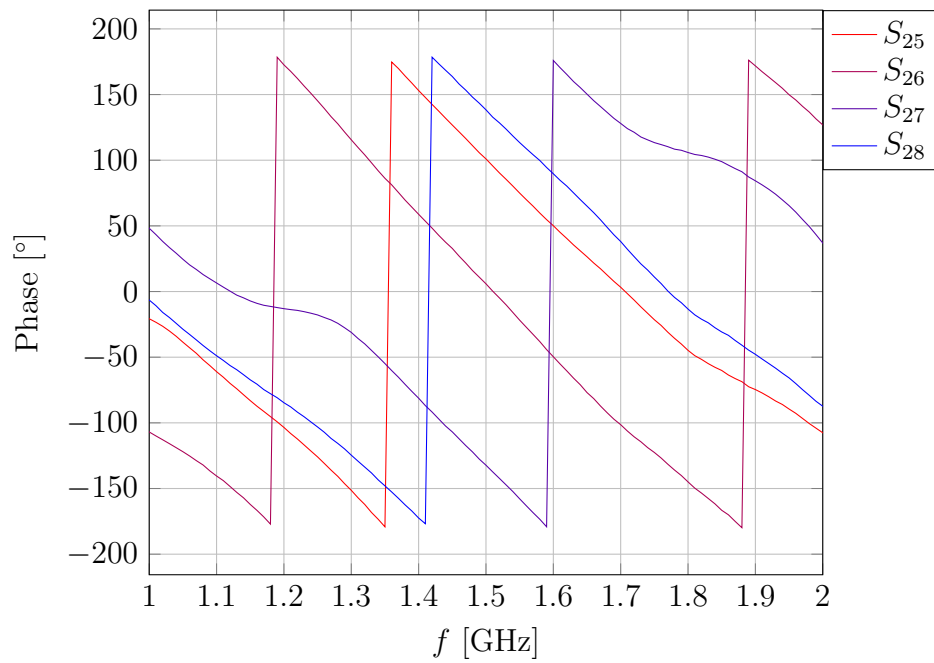


Figure B.21: Measured microstrip PCB - Transmission phase, beam port 2

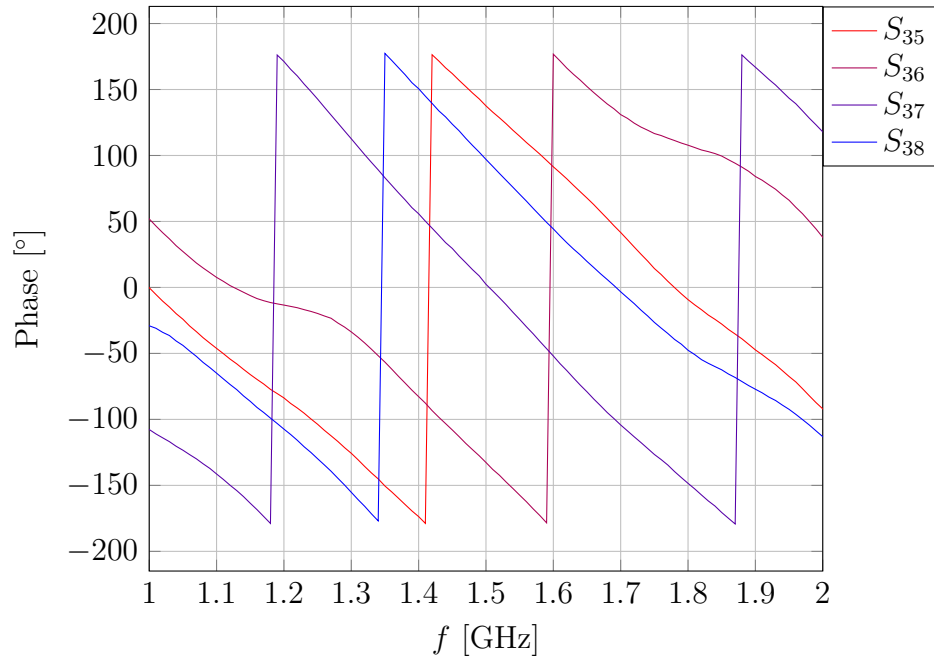


Figure B.22: Measured microstrip PCB - Transmission phase, beam port 3

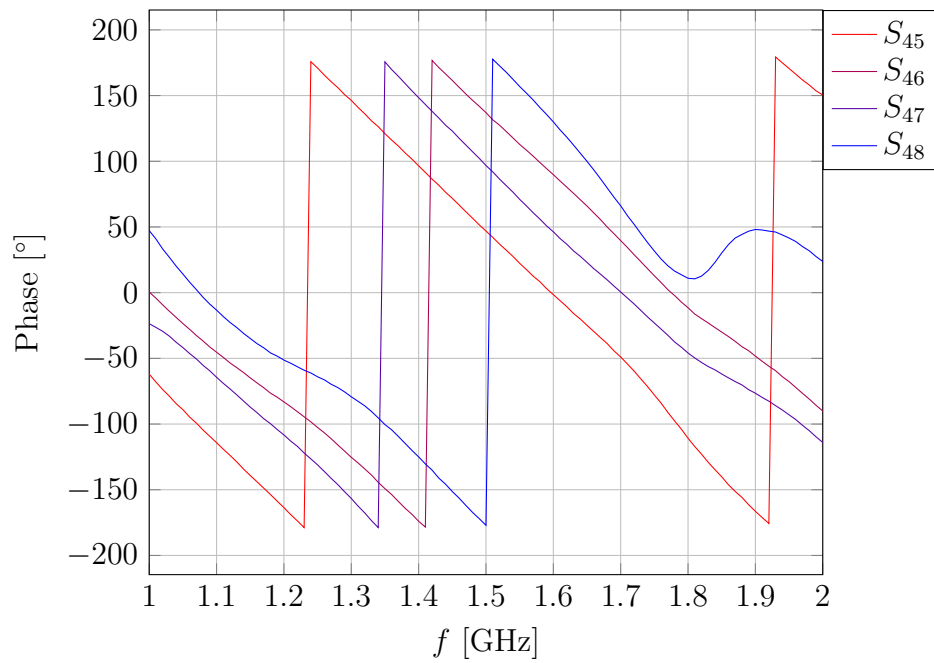


Figure B.23: Measured microstrip PCB - Transmission phase, beam port 4

B.4 Butler Matrix results - Ideal, 15 GHz

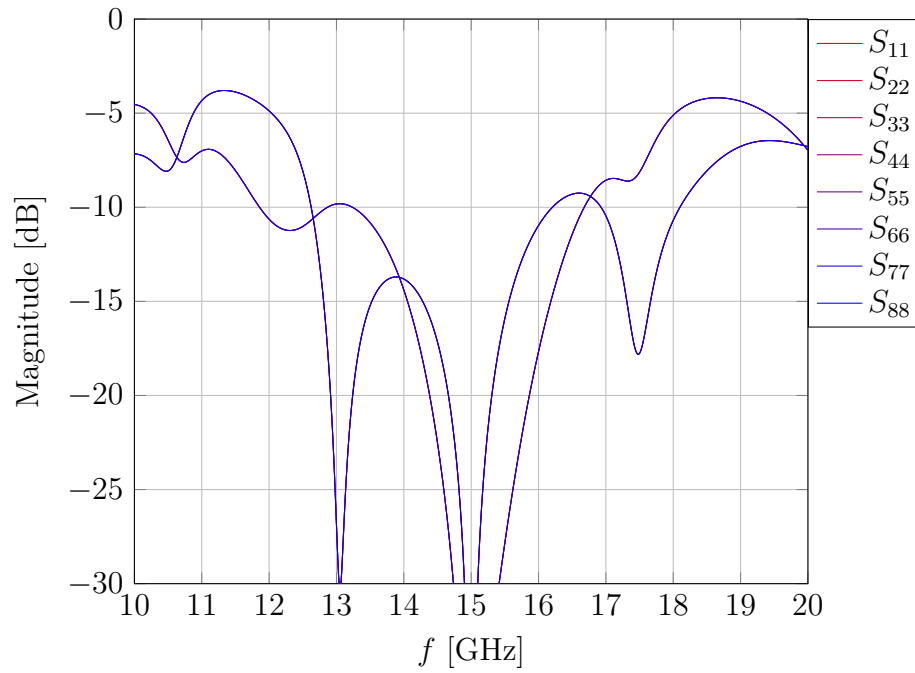


Figure B.24: AWR Ideal simulation - Reflection, 15 GHz

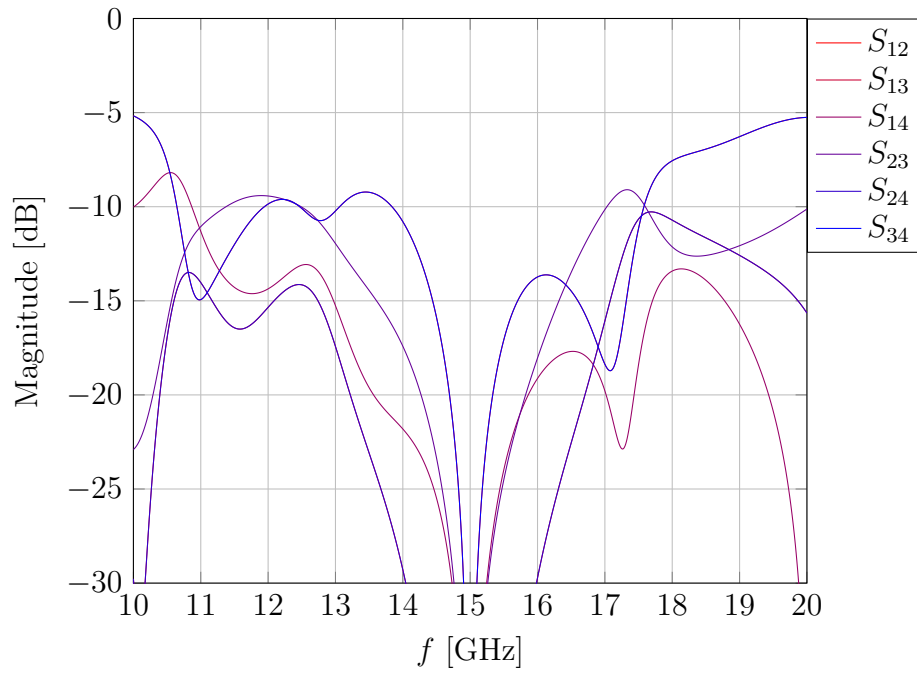


Figure B.25: AWR Ideal simulation - Isolation, 15GHz

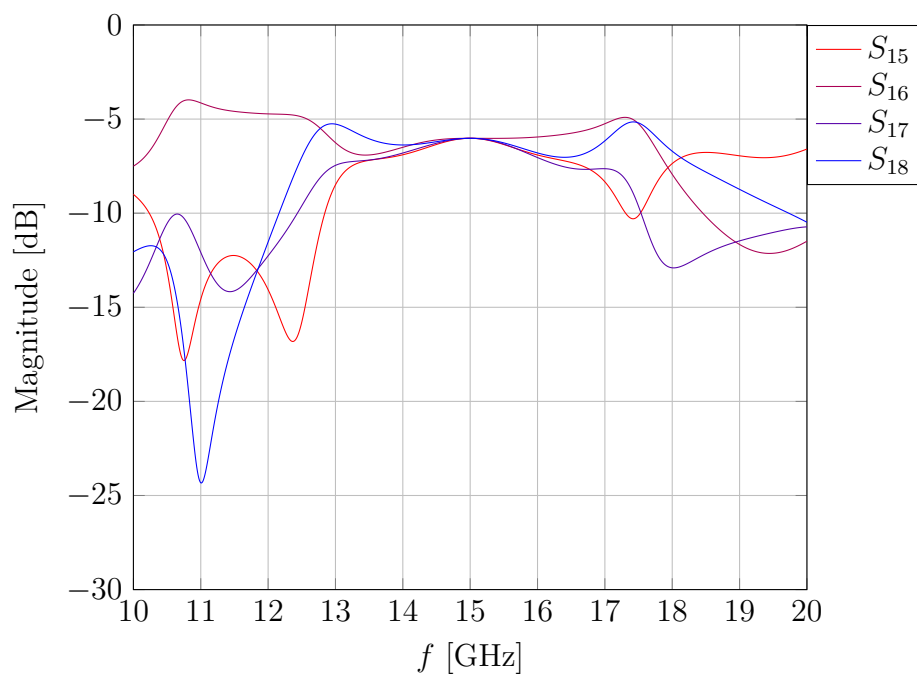


Figure B.26: AWR Ideal simulation - Transmission magnitude, beam port 1, 15 GHz

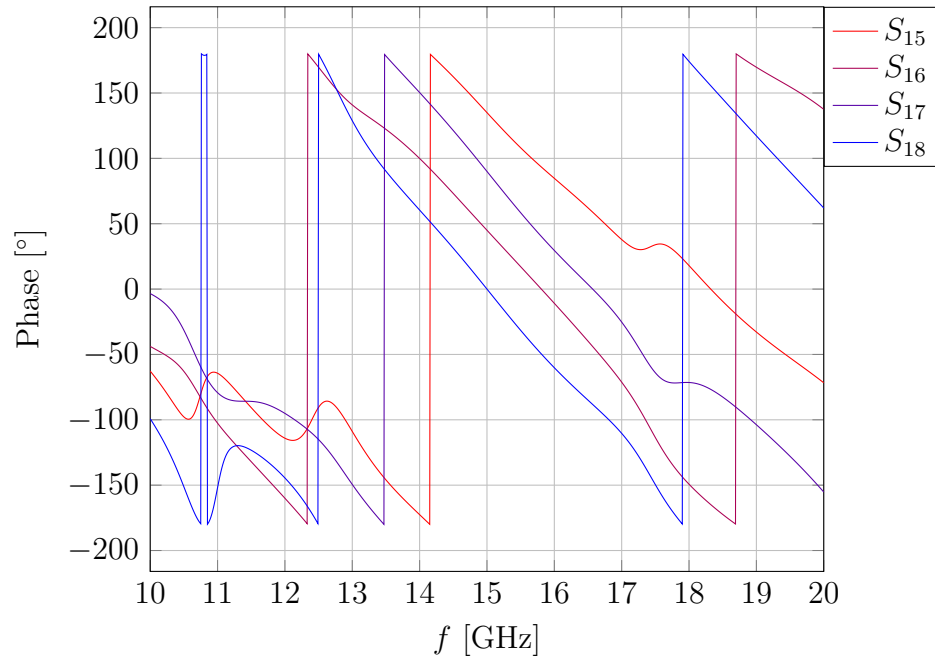


Figure B.27: AWR Ideal simulation - Transmission phase, beam port 1, 15 GHz

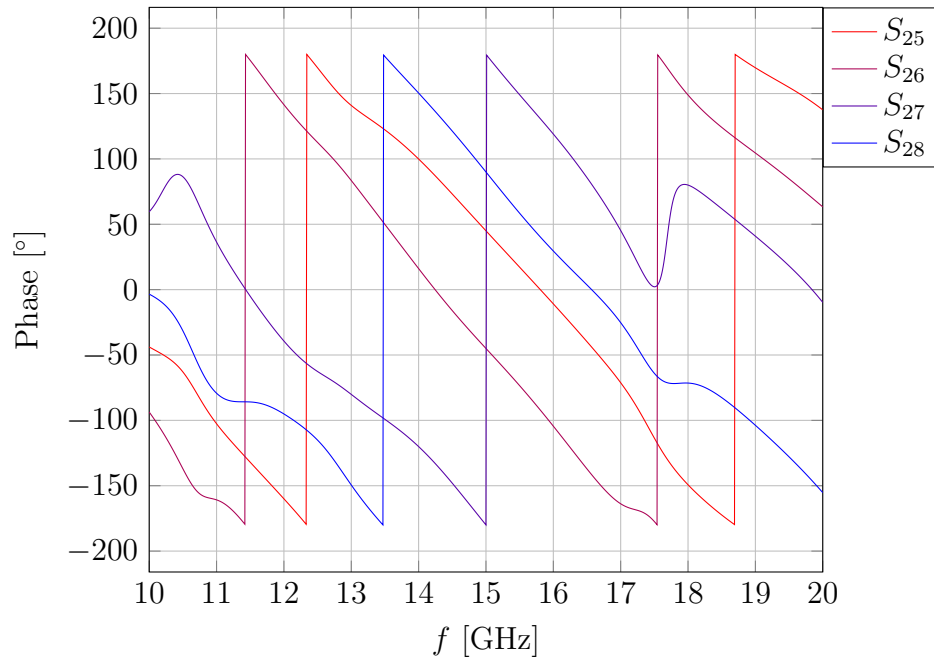


Figure B.28: AWR Ideal simulation - Transmission phase, beam port 2, 15 GHz

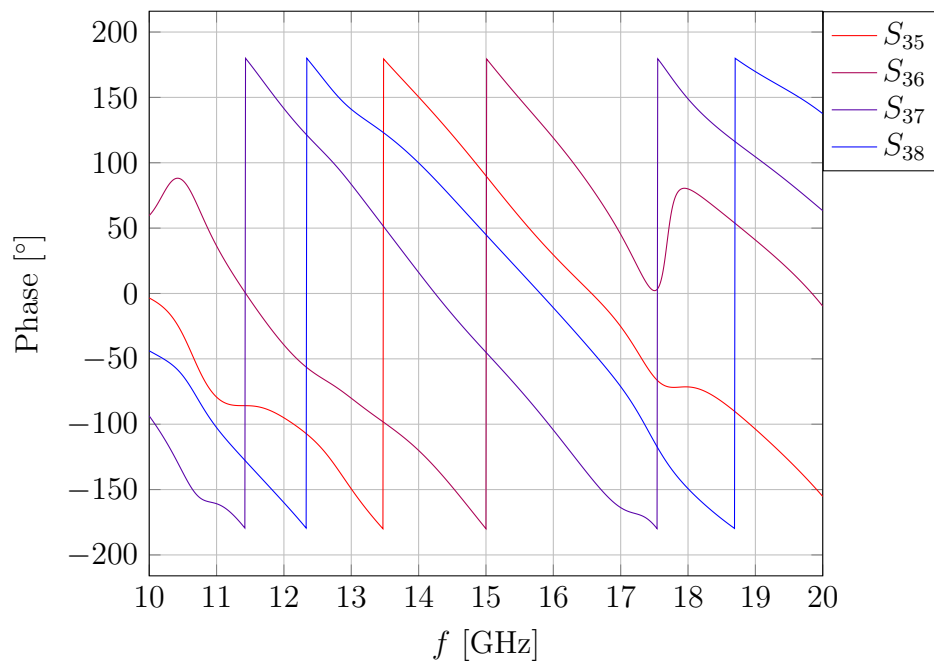


Figure B.29: AWR Ideal simulation - Transmission phase, beam port 3, 15 GHz

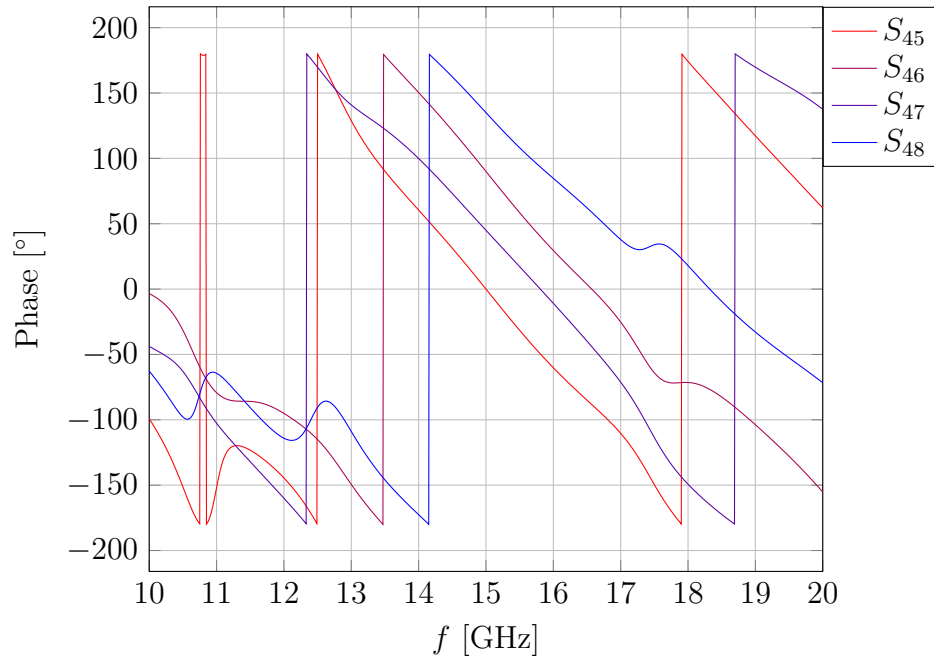
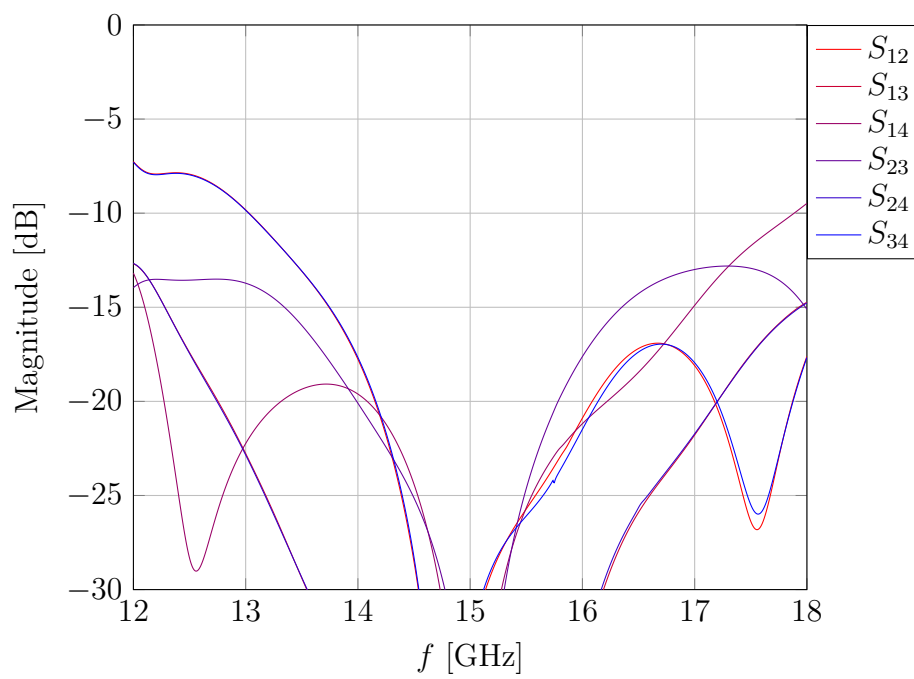
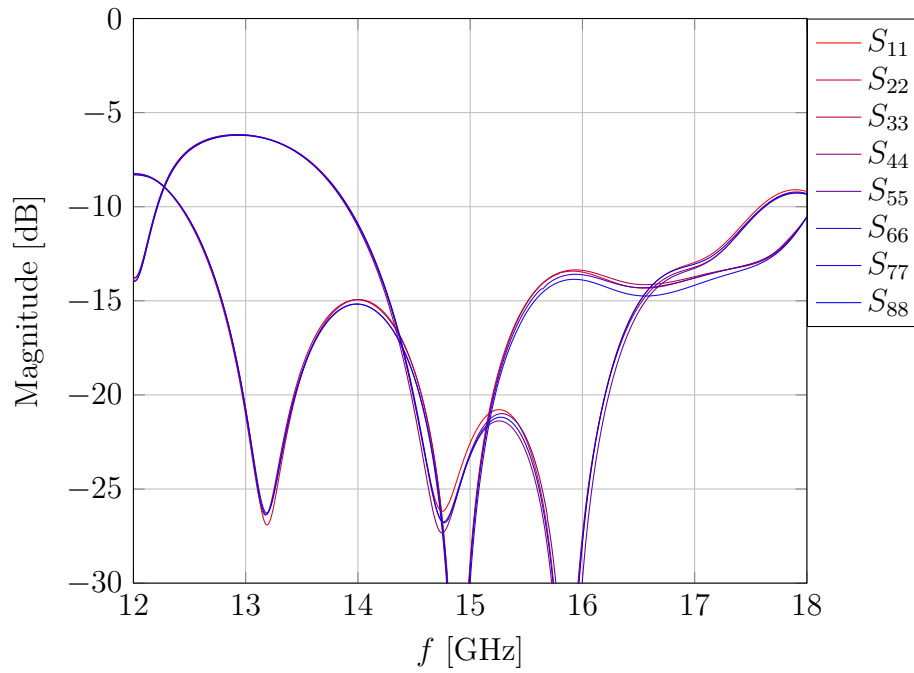


Figure B.30: AWR Ideal simulation - Transmission phase, beam port 4, 15 GHz

B.5 Butler Matrix results - CST Simulation, 15 GHz



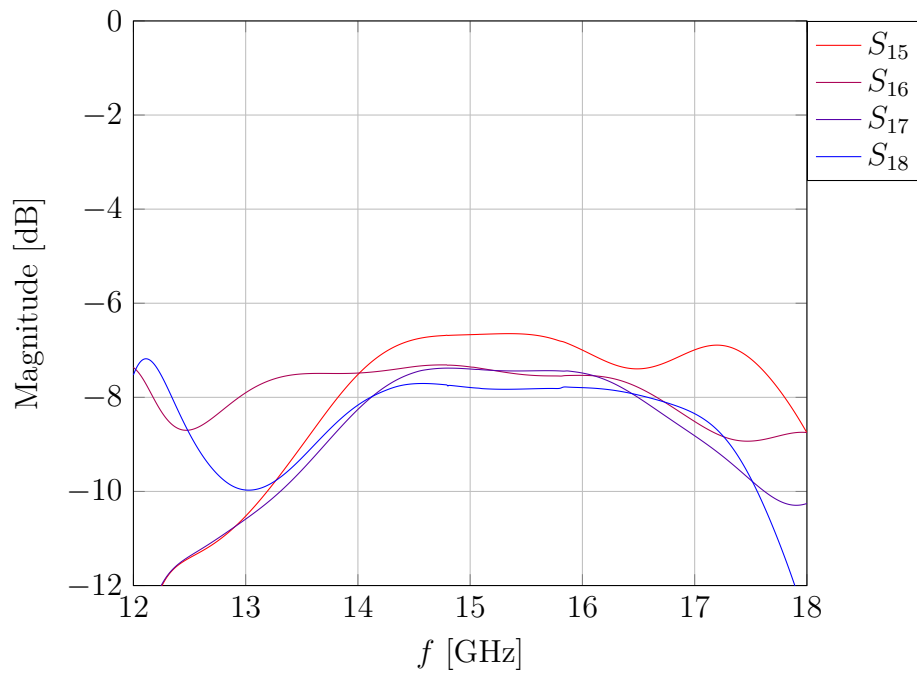


Figure B.33: CST simulation - Transmission magnitude, beam port 1, 15 GHz

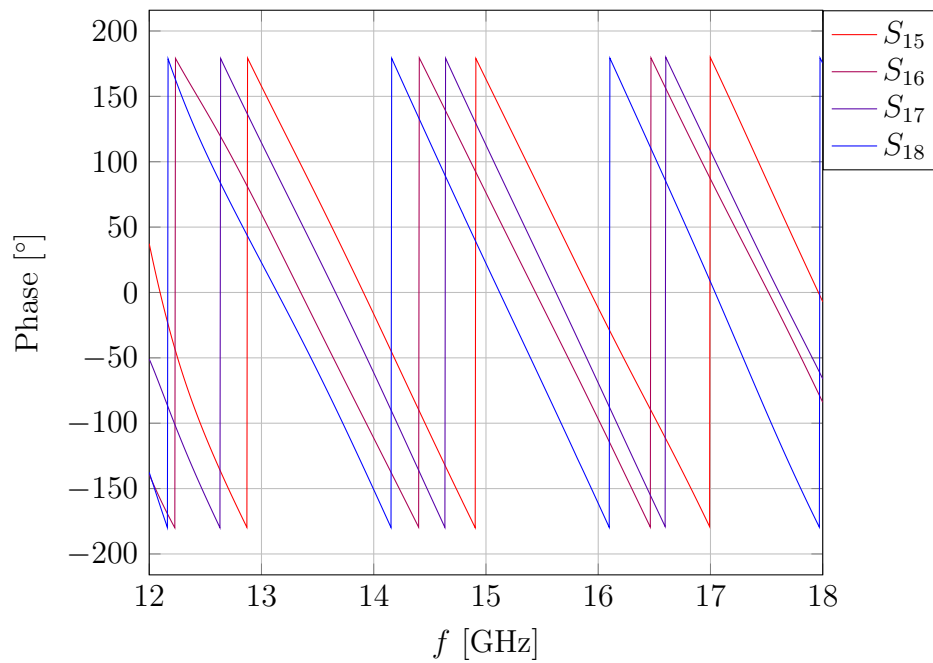


Figure B.34: CST simulation - Transmission phase, beam port 1, 15 GHz

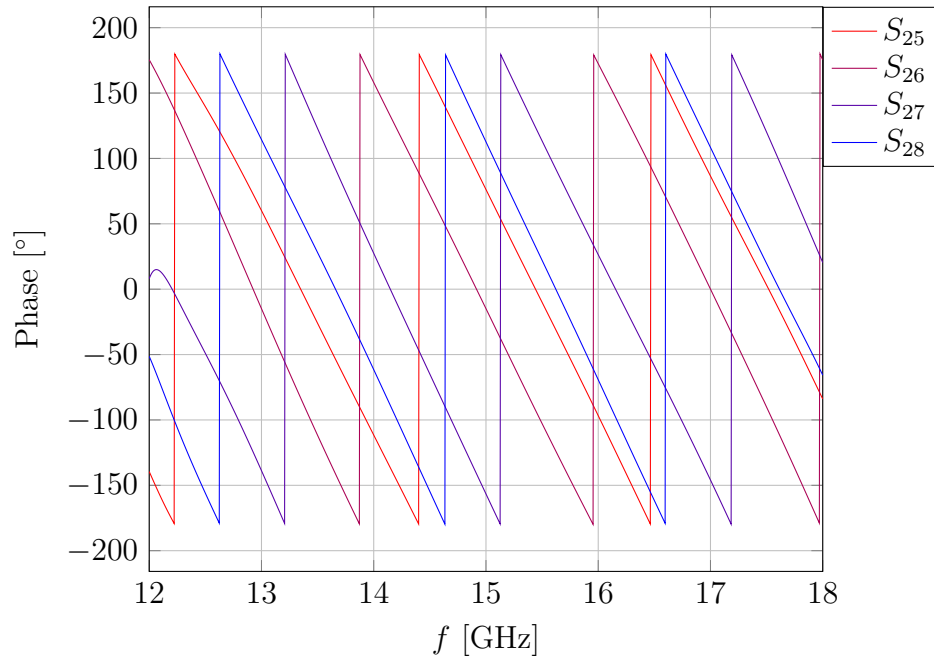


Figure B.35: CST simulation - Transmission phase, beam port 2, 15 GHz

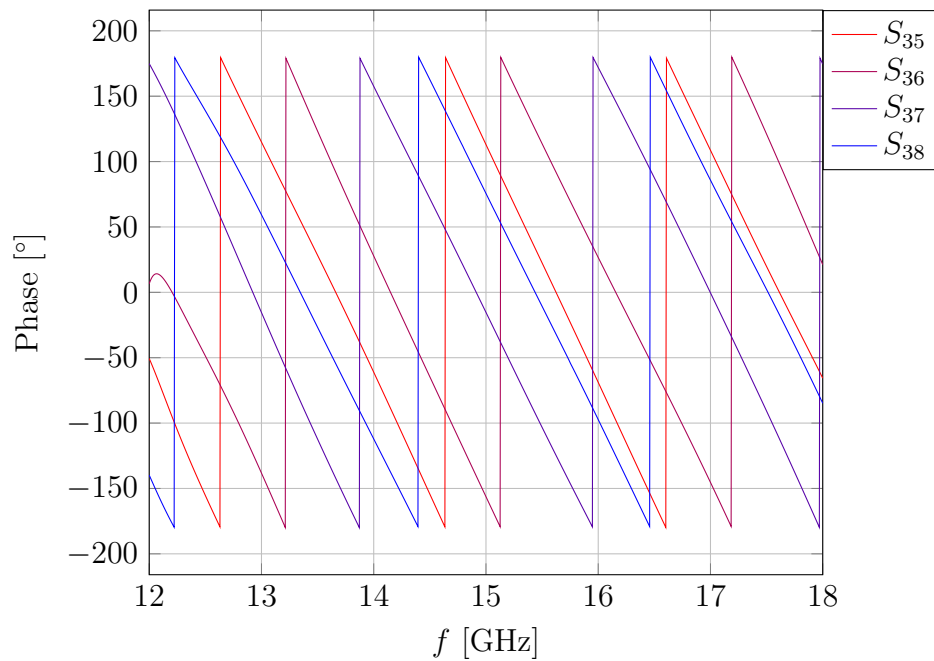


Figure B.36: CST simulation - Transmission phase, beam port 3, 15 GHz

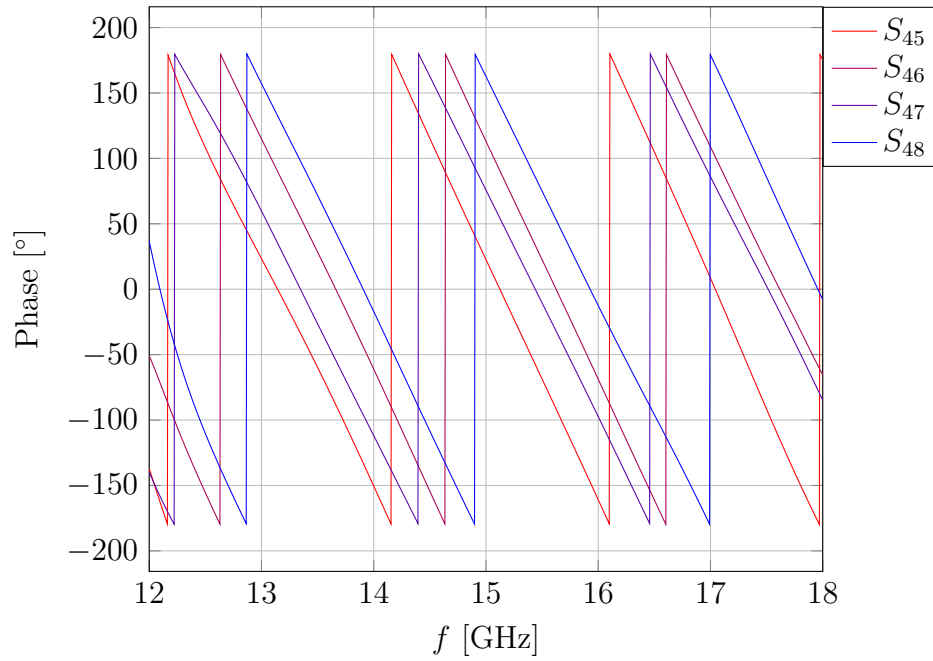


Figure B.37: CST simulation - Transmission phase, beam port 4, 15 GHz

B.6 Butler Matrix results - Measured PCB, 15 GHz

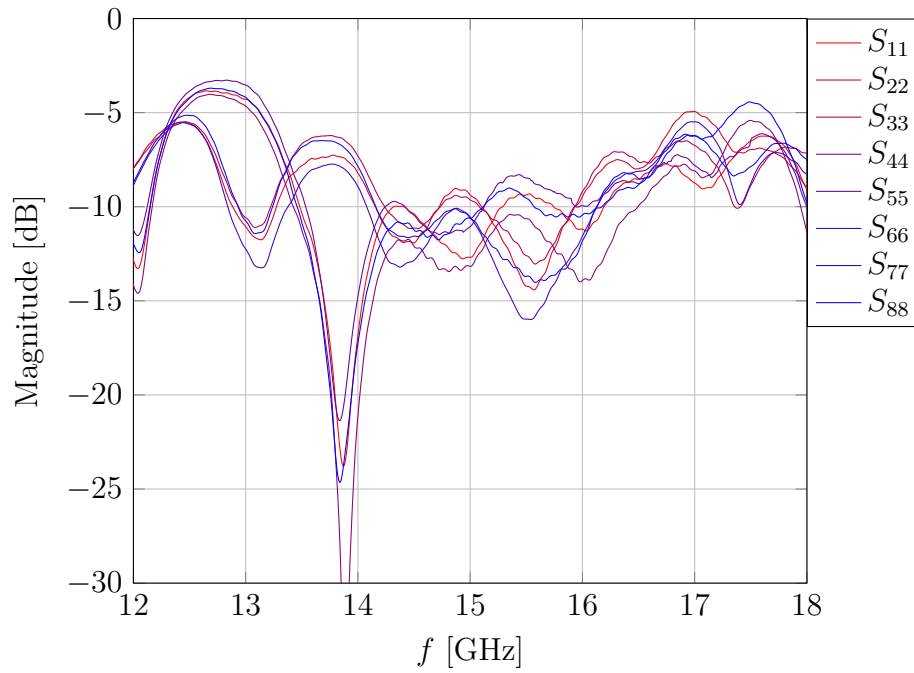


Figure B.38: Measured PCB - Reflection, 15 GHz

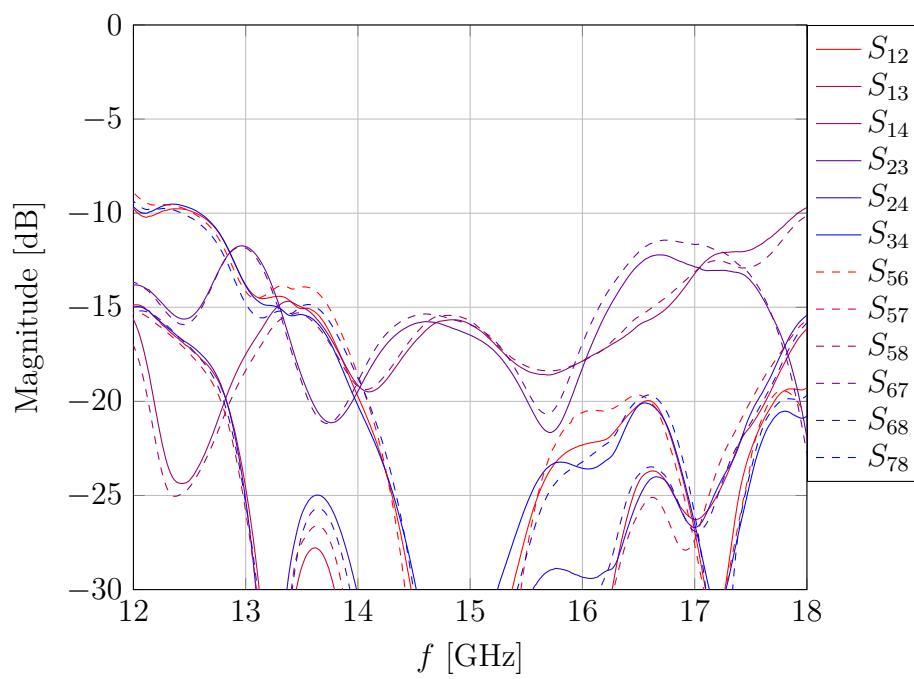


Figure B.39: Measured PCB - Isolation, 15 GHz

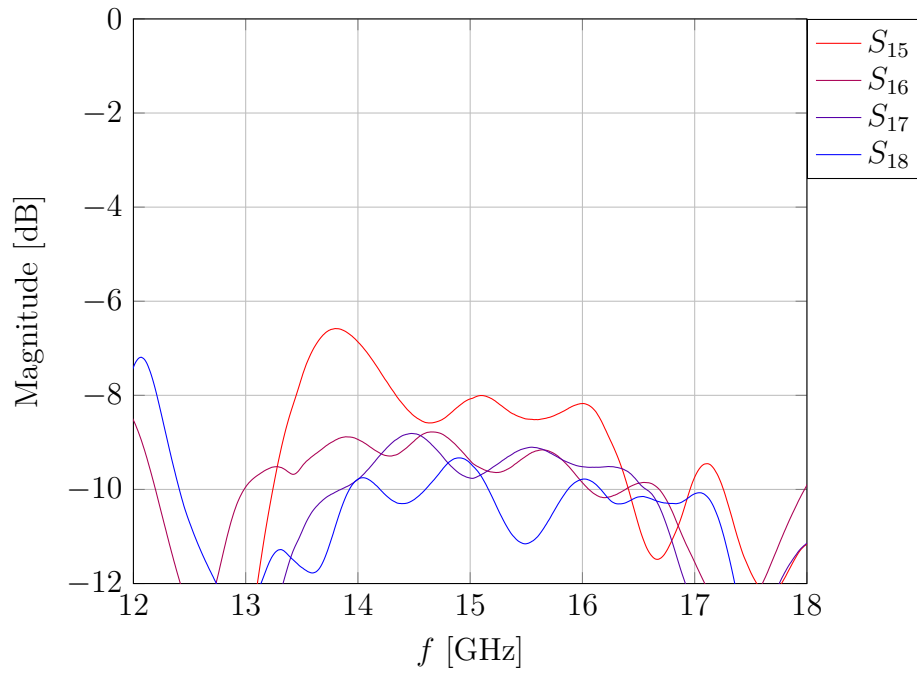


Figure B.40: Measured PCB - Transmission magnitude, beam port 1, 15 GHz

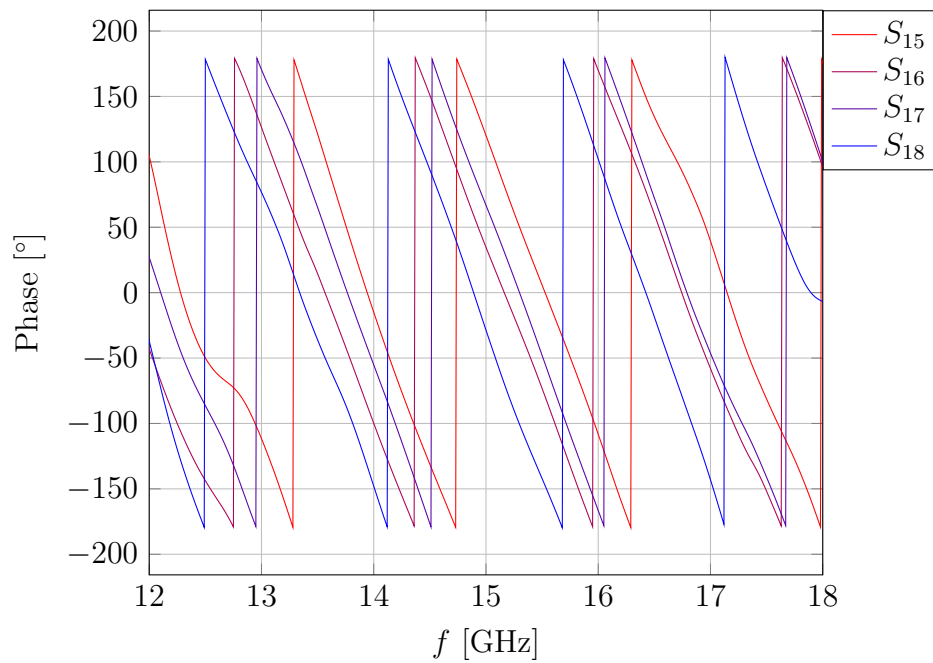


Figure B.41: Measured PCB - Transmission phase, beam port 1, 15 GHz

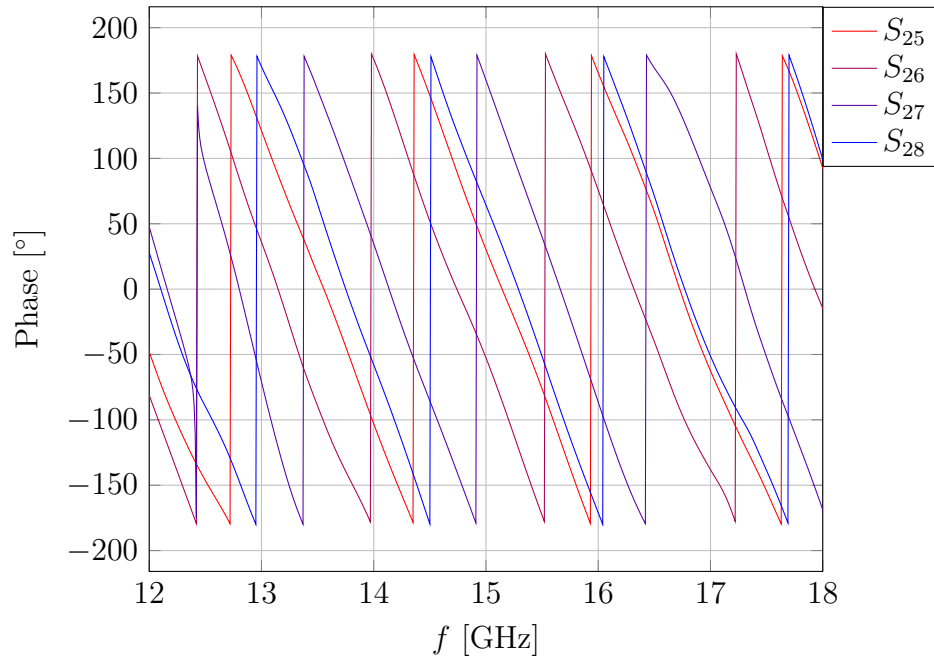


Figure B.42: Measured PCB - Transmission phase, beam port 2, 15 GHz

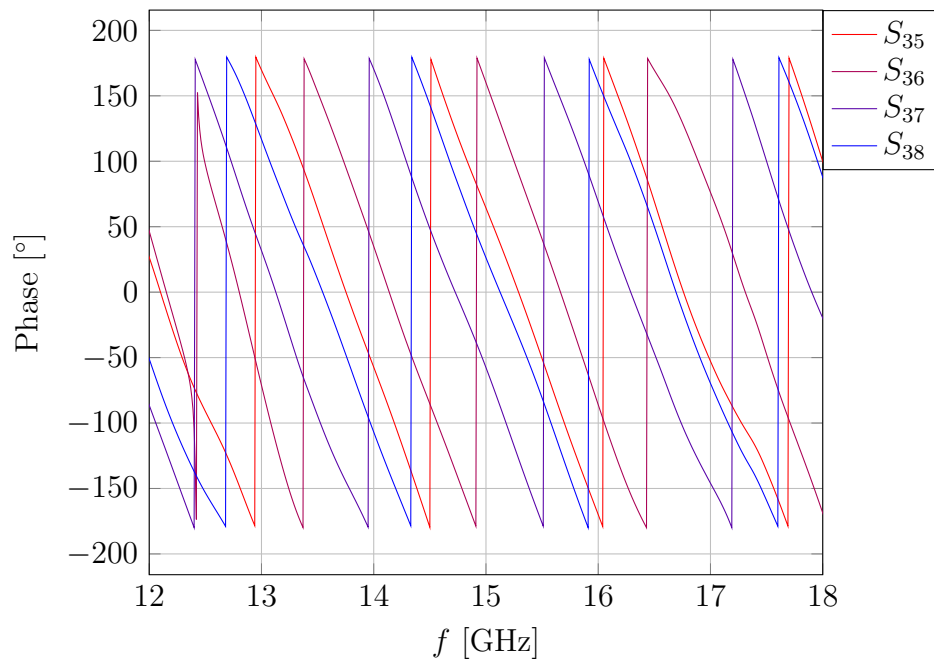


Figure B.43: Measured PCB - Transmission phase, beam port 3, 15 GHz

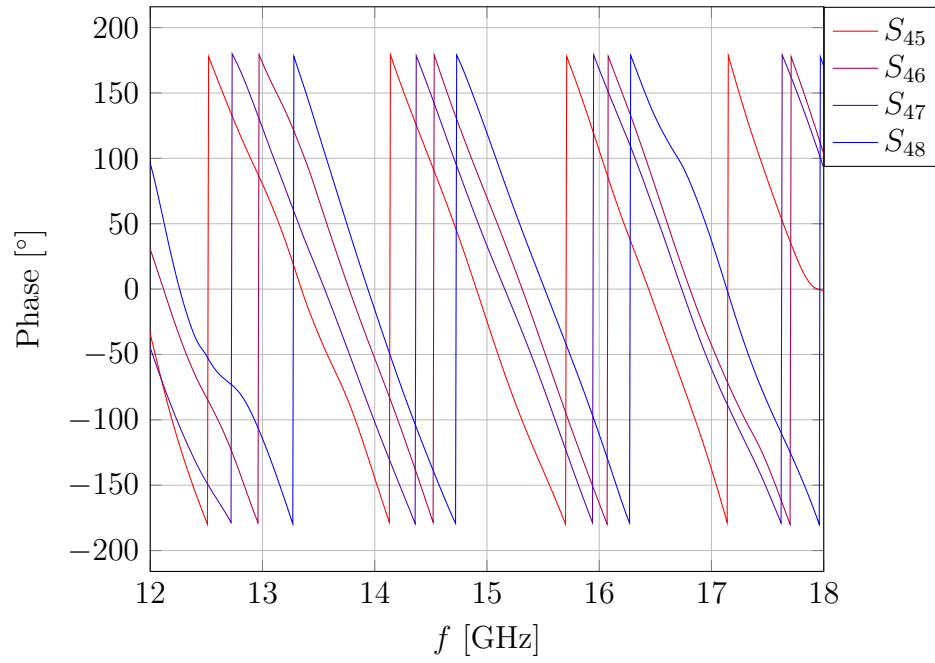


Figure B.44: Measured PCB - Transmission phase, beam port 4, 15 GHz

List of References

- Adamidis, G., Vardiambasis, I., Ioannidou, M. and Kapetanakis, T. (2019 01). Design and implementation of single-layer 4x4 and 8x8 butler matrices for multibeam antenna arrays. *International Journal of Antennas and Propagation*, vol. 2019, pp. 1–12.
- Balanis, C. (2012). *Antenna Theory: Analysis and Design*. Wiley. ISBN 9781118585733.
Available at: <https://books.google.co.za/books?id=v1PSZ48DnuEC>
- Bhattacharyya, A. (2006). *Phased Array Antennas: Floquet Analysis, Synthesis, BFNs and Active Array Systems*. Wiley Series in Microwave and Optical Engineering. Wiley. ISBN 9780471769118.
Available at: <https://books.google.co.za/books?id=nHKsLie6vNOC>
- Blake, L. and Long, M. (2009). *Antennas: Fundamentals, design, measurement*. Electromagnetics and Radar. Institution of Engineering and Technology. ISBN 9781891121784.
Available at: <https://books.google.co.za/books?id=2v0jDwAAQBAJ>
- Butler, J. and Lowe, R. (1961 01). Beam forming matrix simplifies design of electronically scanned antenna. *Electronic Design*, vol. 9, pp. 170 – 173.
- Cheng, D. (2014). *Field and Wave Electromagnetics: Pearson New International Edition*. Pearson Education Limited. ISBN 9781292038940.
Available at: <https://books.google.co.za/books?id=yb6pBwAAQBAJ>
- Ding, K. and Kishk, A. (2018 11). 2-d butler matrix and phase-shifter group. *IEEE Transactions on Microwave Theory and Techniques*, vol. PP, pp. 1–9.
- Hansen, R. (2009). *Phased Array Antennas*. Wiley Series in Microwave and Optical Engineering. Wiley. ISBN 9780470529171.
Available at: <https://books.google.co.za/books?id=vVtnDPhi43YC>
- Huang, Y. and Boyle, K. (2008). *Antennas: From Theory to Practice*. Wiley. ISBN 9780470772928.
Available at: <https://books.google.co.za/books?id=MoI1T9f0xdIC>
- Kraus, J. (1950). *Antennas*. Electrical Engineering Series. McGraw-Hill.
Available at: <https://books.google.co.za/books?id=mgUhAAAAMAAJ>

- Litva, J. and Lo, T. (1996). *Digital Beamforming in Wireless Communications*. Artech House mobile communications series. Artech House. ISBN 9780890067123. Available at: <https://books.google.co.za/books?id=taBpQgAACAAJ>
- Mailloux, R. (2005). *Phased Array Antenna Handbook*. Antennas and Propagation Library. Artech House. ISBN 9781580536899. Available at: <https://books.google.co.za/books?id=xji1ngEACAAJ>
- Pozar, D. (2011). *Microwave Engineering, 4th Edition*. Wiley. ISBN 9781118213636. Available at: <https://books.google.co.za/books?id=JegbAAAAQBAJ>
- Traii, M.e.a. (2008). A new design of compact 4x4 butler matrix for ism applications. *International Journal of Microwave Science and Technology*.